

UNIVERSITY OF CALIFORNIA  
SANTA CRUZ

**EXTRAGALACTIC BACKGROUND LIGHT AND GAMMA-RAY  
ATTENUATION**

A dissertation submitted in partial satisfaction of the  
requirements for the degree of

DOCTOR OF PHILOSOPHY

in

PHYSICS

by

**Rudy C. Gilmore**

June 2009

The Dissertation of Rudy C. Gilmore  
is approved:

---

Professor Joel R. Primack, Chair

---

Professor David A. Williams

---

Professor Stefano Profumo

---

Dean Lisa C. Sloan  
Dean of Graduate Studies

Copyright © by

Rudy C. Gilmore

2009

# Table of Contents

List of Figures	v
List of Tables	xiv
Abstract	xvi
Dedication	xix
Acknowledgments	xx
<b>1 Introduction</b>	<b>1</b>
1.1 Defining the EBL . . . . .	3
1.2 Measurement of the EBL . . . . .	5
1.2.1 Direct Measurement . . . . .	5
1.2.2 Number Counts . . . . .	8
1.2.3 Fluctuation Analysis . . . . .	10
1.3 The EBL and Cosmology . . . . .	11
<b>2 EBL Modeling</b>	<b>15</b>
2.1 Techniques . . . . .	15
2.1.1 Observed Evolution . . . . .	16
2.1.2 Backwards Evolution . . . . .	16
2.1.3 Forward Evolution Models . . . . .	17
2.1.4 Recent Challenges for Semi-Analytic Modeling . . . . .	20
2.2 The Semi-Analytic Model . . . . .	23
2.2.1 Overview . . . . .	24
2.2.2 Dust Absorption and Re-emission . . . . .	28
2.2.3 Non-Stellar Contributions . . . . .	31
<b>3 EBL Results</b>	<b>35</b>
3.1 Star-Formation History . . . . .	35
3.2 Number Counts and Luminosity Functions . . . . .	40

3.3	The Buildup of the EBL . . . . .	45
3.4	Discussion . . . . .	53
<b>4</b>	<b>Gamma-ray Attenuation by the EBL</b>	<b>60</b>
4.1	Historical Overview . . . . .	60
4.2	Gamma-ray Attenuation . . . . .	65
4.3	Gamma-ray Opacity Results . . . . .	69
4.4	EBL Constraints from Gamma-rays . . . . .	70
4.4.1	Effects on Known VHE Blazars . . . . .	78
4.5	Comparison with Other Work . . . . .	86
4.6	Discussion . . . . .	90
<b>5</b>	<b>GeV Gamma-ray Attenuation and the High-Redshift UV Background</b>	<b>95</b>
5.1	Introduction . . . . .	96
5.2	Modeling . . . . .	102
5.2.1	UV Output from Semi-Analytic Models . . . . .	102
5.2.2	Star Formation . . . . .	104
5.2.3	Radiative Transfer . . . . .	109
5.2.4	Ionizing Escape Fraction from Galaxies . . . . .	115
5.2.5	Quasar Emissivity . . . . .	118
5.3	Cosmological Models and Resulting UV Background . . . . .	121
5.3.1	Ly $\alpha$ Forest Constraints . . . . .	121
5.3.2	The Background Flux . . . . .	124
5.4	Gamma-ray Attenuation . . . . .	128
5.5	Discussion . . . . .	132
5.5.1	Comparison With Other Work . . . . .	136
5.5.2	Caveats and Future Work . . . . .	138
<b>6</b>	<b>Attenuation in the Spectra of High-Redshift Gamma-ray Bursts</b>	<b>141</b>
6.1	Introduction . . . . .	142
6.2	Model . . . . .	144
6.2.1	GRB Emission . . . . .	145
6.2.2	Instrument Properties . . . . .	151
6.3	Results . . . . .	154
6.3.1	Predicted Fluences for Fermi . . . . .	156
6.3.2	Predicted Fluences for MAGIC . . . . .	159
6.4	Discussion . . . . .	163
6.4.1	Simulated Results for GRB 080916C . . . . .	169
6.4.2	Intrinsic Spectral Cutoffs . . . . .	172
6.4.3	Future Experiments . . . . .	173
<b>7</b>	<b>Conclusions and Future Work</b>	<b>175</b>
	<b>Bibliography</b>	<b>182</b>

# List of Figures

2.1	Comparison of the dust emission templates of Rieke et al. (2009) (red) and Devriendt & Guiderdoni (2000) (blue). The four panels show templates for bolometric IR luminosities of $10^{10} L_{\odot}$ , $10^{11}$ (a LIRG), $10^{12}$ (a ULIRG), and $10^{13}$ (an extremely IR-bright ‘Hyper-LIRG’). . . . .	32
3.1	The star-formation rate density in each of the two SAMs over cosmic time. The solid black and broken blue curves are the fiducial and low models, respectively. The red points are data from the compilation in Hopkins (2004) with conversion to a Chabrier IMF, and the dot-dashed red line shows the best fit to the data from Hopkins & Beacom (2006). Green points are from $24\mu\text{m}$ observations by Pérez-González et al. (2005).	37
3.2	The stellar mass density (integrated star formation rate density) for the two models. This plot has been reproduced from Somerville et al. (2008) (S08). The solid blue curve denotes the fiducial model, and broken orange the low model. The solid square is the $z=0$ estimate of Bell et al. (2003), the circles are from Fontana et al. (2006), and the open diamonds are from the COMBO-17 estimates of Borch et al. (2006). The gray line is the best fit to the observational compilation of Wilkins et al. (2008). . .	38
3.3	Number counts in the four HST ACS bands. The solid black line represents the fiducial model, and the dashed blue line is the low model. Red, blue and green data is from the compilation by Dolch (2009), which includes data from the Hubble Ultra-Deep Field. Additional data in orange from SDSS-DR6 is provided by Montero-Dorta & Prada (2008). . . . .	42
3.4	Galaxy counts in the K-band ( $\sim 2.2 \mu\text{m}$ ). Lines colors and types are as in the previous figure. Data is from the 6dF survey (Jones et al., 2006) (orange stars), 2MASS (Kochanek et al., 2001) (red stars), and DEEP2/Palomar (Conselice et al., 2008)(green pentagons). Red stars at bright magnitudes are from Gardner et al. (1996), magenta stars are from Martini (2001), and blue squares are from Barro et al. (2009). . . . .	43

3.5	Number counts from four Spitzer (IRAC and MIPS) infrared bands; as in previous figures the solid black line represents the fiducial model, and the dashed blue line the low model using Devriendt dust templates (see Section 2.2.2). The long dashed red line shows the fiducial model using the new Rieke dust emission templates. Data in the IRAC bands is from Fazio et al. (2004); Sanders et al. (2007); the MIPS data is from Papovich et al. (2004); Shupe et al. (2008); Chary et al. (2004) at $24\mu\text{m}$ and (Frayer et al., 2006) at $70\mu\text{m}$ . . . . .	44
3.6	The rest-frame luminosity functions for the fiducial model in a variety of bands. Solid and dashed curves show the model with and without dust processing. In the SDSS bands, orange data is from SDSS-DR6 (Montero-Dorta & Prada, 2008), while blue points are from the older SDSS-DR2 (Blanton et al., 2003). For the K-band plot, the green points are from 2dF (Cole et al., 2001) while the red are from 2MASS (Kochanek et al., 2001). . . . .	46
3.7	The $z=0$ luminosity density of our model. As before, the fiducial model is shown as a solid black line, the low model as dashed blue, and the fiducial model with Rieke dust templates is dashed red. Data at a number of wavelengths is shown from GALEX (blue circle), SDSS (green stars; Montero-Dorta & Prada, 2008), 6dF (magenta pentagons; Jones et al., 2006), 2MASS (green star; Cole et al., 2001, and red star; Bell et al., 2003). In the mid- and far-IR, the orange squares are from IRAS (Soifer & Neugebauer, 1991), while blue stars are from an analysis of local emissivity using data from IRAS, ISO, and SCUBA (Takeuchi et al., 2001). . . . .	47
3.8	The luminosity density (integrated luminosity function of sources within a given redshift range) in our models vs. redshift at $2800 \text{ \AA}$ and in the B-, R-, and J- bands (approximately $4500 \text{ \AA}$ , $6500 \text{ \AA}$ , and $1.25 \mu\text{m}$ , respectively). The fiducial model is shown in black, the low model as dashed blue. Data for the $2800 \text{ \AA}$ plot is from Dahlen et al. (2007) (blue squares) and Gabasch et al. (2006) (red stars). In the B-, R-, and J-bands data from the COMBO-17 and DEEP surveys is included from Faber et al. (2007) (red stars and squares), Dahlen et al. (2005) (blue squares), and Wolf et al. (2003) (green stars). Purple hexes are from Marchesini et al. (2007). . . . .	48

3.9	The predicted $z = 0$ EBL spectrum from our fiducial (black) and low (dashed blue) models using the Devriendt dust templates, and the fiducial model with Rieke templates (red long-dashed), compared with experiments at a number of wavelengths. Our previous model (Primack et al., 2005), and the model of Franceschini et al. (2008) are also shown for comparison (dotted green curve and dash-dotted orange curve). Upward pointing arrows indicate lower bounds from number counts; other symbols are results from direct detection experiments. <b>Lower limits:</b> The blue-violet triangles are results from Hubble and STIS (Gardner et al., 2000), while the magenta open triangles are from GALEX (Xu et al., 2005). The green and red triangles from Hubble Deep Field (Madau & Pozzetti, 2000) and Ultra Deep Field (Dolch, 2009) respectively, combined with ground based-data. Open red triangles are from IRAC on Spitzer (Fazio et al., 2004), and the pink point at $15 \mu\text{m}$ is ISOCAM (Elbaz et al., 2002) on ISO. The remaining lower limits are from MIPS at 24, 70, and $160 \mu\text{m}$ on Spitzer (Papovich et al., 2004; Chary et al., 2004; Frayer et al., 2006; Dole et al., 2006). <b>Direct Detection:</b> The open blue diamonds are from Bernstein (Bernstein, 2007). The points at 1.25, 2.2, and $3.5 \mu\text{m}$ are based upon DIRBE data with foreground subtraction (Wright, 2001) (dark red squares), (Cambrésy et al., 2001) (orange 4-stars), (Levenson & Wright, 2008) (red diamond), (Gorjian et al., 2000) (purple open hexes), (Wright & Reese, 2000) (green square), and (Levenson et al., 2007) (red asterisks). In the far-IR, direct detection data is shown from DIRBE (Wright, 2004) (blue stars), and (Hauser et al., 1998) (green stars), and also purple bars showing the detection of FIRAS (Fixsen et al., 1998). . . . .	51
3.10	The history of the EBL in each of our models. The top 2 plots show the background flux at past redshifts in the fiducial (left) and low (right) models in standard units. Redshifts shown include $z = 0$ (solid), $z = 0.2$ (dotted), $z = 0.6$ (short dashed), $z = 1$ (long dashed), $z = 1.5$ (dot-short dashed), $z = 2$ (dot-long dashed) and $z = 2.5$ (long and short dashed); also see the key in the upper-left panel. The bottom two plots show the same quantities, but now evolved to present-day, allowing easy comparison of the EBL in place at a particular time compared to the total at $z = 0$ . . . . .	54
3.11	The buildup of the photon population at various wavelengths shown separately for our fiducial and low models, showing the fraction of photons at a given present-day wavelength in place at past redshifts. The wavelengths are indicated as follows: violet = $400 \text{ nm}$ , blue = $1 \mu\text{m}$ , green = $2.2 \mu\text{m}$ , orange = $24 \mu\text{m}$ , and red = $160 \mu\text{m}$ . . . . .	55

3.12	The counts at 850 microns, compared to predictions from our model; see discussion in the text. Solid black, dashed blue, and long-dashed red lines denote results from the fiducial and low model with Devriendt templates, and the fiducial model with Rieke templates, respectively. Data is from the SCUBA SHADES survey (Coppin et al., 2006). . . . .	59
4.1	This plot shows the kinematics for EBL interactions in graphical form. The upper dashed line is the maximum wavelength of EBL photon with which a gamma ray of energy $E_\gamma$ can interact, assuming an optimal ‘head-on’ $\theta = \pi$ configuration. The solid line is the wavelength for which the cross-section is maximized, assuming an angle of incidence $\theta = \pi/2$ , where statistically the most interactions will occur. The dash-triple-dotted line shows where the cross section falls to half of its maximal value, again assuming $\theta = \pi/2$ . The horizontal dotted line shows where the background energies are 13.6 eV (1 Rydberg). As we shall see later when we discuss the UV background, the density of background photons falls rapidly at wavelengths shortward of this point due to absorption of hydrogen-ionizing photons by stellar atmospheres, H I in galaxies, and processing by the intergalactic medium (IGM). . . . .	67
4.2	The functional form of $\sigma(E_1, E_2, \theta)$ , as a function of $E_\gamma/E_{th}$ . . . . .	68
4.3	The attenuation $e^{-\tau}$ of gamma-rays vs. gamma-ray energy, for sources at $z = 0.05, 0.1, 0.2$ , and $0.536$ (the redshift of 3C279). Following the convention of our previous plots, the fiducial model is solid black, the low model is dashed blue, and the fiducial model using new Rieke dust templates is shown in long-dashed red. Note that the dust modeling only affects observations above about 3 TeV. Increasing distance causes absorption features to increase in magnitude and appear at lower energies. The plateau seen between 1 and 10 TeV at low redshift is a product of the mid-IR valley in the EBL spectrum. . . . .	71
4.4	The gamma-ray attenuation edges for our 3 EBL models; colors and line types are as in the previous plot. The curves show the redshift at which the pair-production optical depth $\tau$ reaches the indicated value for a particular observed gamma ray energy. The sets of curves from lower left to upper right are the contours for $\tau = 1, 3$ , and $10$ . . . . .	72

4.5	Present-day flux predicted in our 3 EBL models, compared against upper limits from gamma-ray observations. The models shown are as in Figure 3.9; solid black and dashed blue lines are fiducial and low models using the Devriendt dust templates, and dashed red is the fiducial model with Rieke templates. The SED from Primack et al. (2005) is also shown as dotted green. Upper limits are from Aharonian et al. (2006) (thick green line), MAGIC observations of 3C279 (Albert et al., 2008a) (red stars), the combined analyses of Mazin & Raue (2007) (purple dots) and Dwek & Krennrich (2005) (indigo triangle). The reader should consult the text for more details and caveats in interpreting this figure. . . . .	77
4.6	Here we show the results of Table 4.4.1 in graphical form. The measured spectral index ( $\Gamma$ ; $dN/dE \propto E^{-\Gamma}$ ) and redshift of each blazar is shown as a black square with error bars, with the spectrum corrected via the fiducial EBL shown as a orange (lower) point and that of the low EBL in blue (higher). The horizontal dotted line shows $\Gamma = 1.5$ , which is typically taken as the hardest spectrum possible under usual assumptions. Some points have been shifted sideways slightly for readability. . . . .	84
4.7	Our EBL models compared with those of (Franceschini et al., 2008) and the best-fit model of (Kneiske et al., 2004), at present-day and $z = 1$ . In each plot, our fiducial and low models with Devriendt dust templates are solid black and dashed blue, respectively, and the fiducial model using Rieke templates is long-dashed red. Kneiske's best-fit model is shown as long-dashed green and Franceschini as dot-dashed orange. The baseline and fast evolution models of Stecker et al. (2006) are the low and high dotted violet points in the $z = 0$ panel. . . . .	89
5.1	The emissivity due to galaxies predicted by our fiducial galaxy-formation model at a number of redshifts, normalized to $1 M_{\odot}/\text{yr}$ . Dotted curves show the emission predicted in the absence of dust extinction. Vertical lines indicate the ionization energies of H I and He II at 912 and 228 Å. . . . .	103
5.2	Number counts in the GALEX 1530 Å. The solid black line shows the fiducial model, and dashed blue shows the low model. Note that the low model has counts equal to or slightly greater than the fiducial model at some magnitudes due to differing amounts of dust extinction. Data are from GALEX (Xu et al., 2005, green squares), STIS on HST (Gardner et al., 2000, purple asterisks), and the balloon-borne FOCA experiment (Iglesias-Páramo et al., 2004; Milliard et al., 1992, red stars and open pentagons respectively). Following Xu et al. (2005), all counts have been converted to the GALEX band by assuming a UV spectral slope of -0.8. . . . .	105
5.3	Number counts in the GALEX 2310 Å. Curves and data are the same as in the previous figure. . . . .	106

5.4	The emissivity at $1500 \text{ \AA}$ as a function of redshift in our models. As previously, the solid black line is the fiducial model, and the dashed blue line shows the low model. The blue circle at redshift 0.1 is GALEX data from Wyder et al. (2005) and the purple stars are measurements using GALEX and other data (Schiminovich et al., 2005). The red squares are from GOODS (Dahlen et al., 2007), the red circles are determinations from ground-based observations (Reddy et al., 2008), and the green stars are from Bouwens et al. (2007). . . . .	107
5.5	The global star formation rate density predicted by our models, compared with a compilation of observational data. The solid black and dashed blue curves show the SFRD history of our fiducial and low models, respectively. The black dash-dot curve which diverges from the fiducial curve above redshift three is the ‘high-peaked’ form which we discuss in the text. The red squares at lower redshift are from the compilation of Hopkins (2004). The purple stars are from observations by Bouwens et al. (2008, 2007) of dropout-selected galaxies. For these we show the dust-corrected results from integrating the luminosity functions down to a value of $0.04 L_*$ at $z = 3$ ; it is possible that fainter objects provide an additional contribution. The magenta squares at redshift 4.5 and 6 show inferred star formation rates from gamma-ray burst observations (Yüksel et al., 2008). The green circle is based on observations of Lyman-break galaxies at $z \sim 5$ (Verma et al., 2007), and the orange triangle is an upper limit from VLT data (Mannucci et al., 2007). The blue squares are results from the Subaru Deep Field (Ouchi et al., 2004). All data have been corrected for extinction (by the authors) and converted to a Chabrier IMF. . . . .	110
5.6	Effective optical depth as a function of redshift from our assumed absorption cloud distribution. Data from quasar spectra are shown at ( $5 < z < 6.5$ ) from Fan et al. (2006); here the blue points are averaged Gunn-Peterson measurements, and the red, cyan, and green symbols are $\text{Ly}\alpha$ , $\beta$ , and $\gamma$ measurements of the highest-redshift individual objects. Values at lower redshifts are from Schaye et al. (2003) (green circles) and Dall’Aglia et al. (2008) (red stars). . . . .	113
5.7	Quasar luminosity density for the Hopkins et al. (2007) (solid black) and Schirber & Bullock (2003) Model ‘C’ (broken green) models at 912 (upper lines) and $228 \text{ \AA}$ (lower lines). The latter has been multiplied by a factor of 0.8 to better match the observations at low redshift. . . . .	120

5.8	<p>Ionization rate per hydrogen atom (with units of <math>10^{-12} \text{ s}^{-1}</math>) in our four scenarios compared with data at a range of redshifts. Black solid lines: fiducial model with H I escape fractions from star-forming galaxies of 0.02, 0.1, and 0.2 (bottom to top). Dashed blue lines: low star-formation model, with escape fractions 0.1, 0.2, and 0.5. Orange dash-dotted line: high-peaked star formation rate with escape fraction 0.1. These aforementioned models all use the quasar emissivity of HRH07. The long-dashed green line shows the fiducial SFR model with quasar model C of Schirber &amp; Bullock (2003), and escape fraction 0.02. Data points are divided into those obtained from flux-decrement analysis (black) and those obtained via proximity effect near quasars (green). References for the former are Bolton et al. (2005); Fan et al. (2006); Faucher-Giguère et al. (2008b); Kirkman et al. (2005); Tytler et al. (2004), and the latter include Scott et al. (2000); Cooke, Espey, &amp; Carswell (1997); Giallongo, Fontana, &amp; Madau (1997); Cristiani et al. (1995); Williger et al. (1994); Lu, Wolfe, &amp; Turnshek (1991); Bajtlik, Duncan, &amp; Ostriker (1988). Some points have been shifted slightly for readability. . . . .</p>	125
5.9	<p>The ratio of He II to H I column densities plotted against redshift. Higher values indicate a softer ionizing background, with comparatively more ionizing photons available per hydrogen atom. Line types in this plot are the same as in Figure 5.8. Data are from observations of He II Ly<math>\alpha</math> systems by Zheng et al. (2004) and Fechner et al. (2006). . . . .</p>	126
5.10	<p>The history of the background flux, shown at the present day and three other redshifts. Intensities at the nonzero redshifts have been multiplied by the indicated factors (<math>10^{-2}</math>, <math>10^{-4}</math>, and <math>10^{-6}</math> at <math>z = 1.6</math>, <math>3.2</math>, <math>5.8</math>, respectively) to separate the lines. Black solid line: fiducial model with H I escape fraction of 0.1. Dashed blue line: low star-formation model, with escape fraction 0.2. Orange dash-dotted line: high-peaked star formation rate with escape fraction 0.1. Green long-dashed: fiducial model with SB03 quasar contribution and escape fraction 0.02. At low redshift, only the first two models are shown, as the other models do not produce discernibly different levels of background at these times. We have also shown observational measurements of the background flux at <math>z = 0</math> in the UV, optical, and near-IR from Figure 3.9. . . . .</p>	127
5.11	<p>Attenuation factors (<math>e^{-\tau}</math>) as a function of gamma-ray energy for the indicated source redshifts. Curves are as in Figure 5.10, and indicate the absorption resulting from our models of star-formation and quasar emissivity. Black solid line: fiducial model with H I escape fraction of 0.1. Dashed blue line: low star-formation model, with escape fraction 0.2. Orange dash-dotted line: high-peaked star formation rate with escape fraction 0.1. Green long-dashed: fiducial model with SB03 quasar contribution and escape fraction 0.02. Curves for the high-peaked star formation and high quasar models converge to the fiducial model for <math>z \leq 2</math>.</p>	129

5.12	The redshifts at which the universe becomes optically thick ( $\tau > 1$ ) to gamma rays at a given energy. Line types and colors are as in Figure 5.11.	131
6.1	The bursts seen by Swift BAT for which we have well-measured redshifts, shown on axes of redshift and fluence. The fluences observed by BAT at energies from 15–150 keV have been converted to the BATSE energy range (20 keV – 2 MeV) using a Band function over these energy ranges with peak 250 keV and low and high energy spectral indices of -1 and -2.2, respectively. For reference, we also show the position of GRB 080916C on this plot based on its GBM fluence (single red star). This burst was not seen by Swift until nearly 17 hours after its detection by GBM and LAT (Kennea, 2008), and was not included in our analysis.	147
6.2	The fluence factors arising due to the slew time delay for ground-based telescopes. The solid black curve shows the percentage of prompt fluence in the total sample which is seen after a time $T_{delay}$ , if the GeV flux is proportional to that in the BAT energy range and is constant across $T_{90}$ . The red curve shows the fraction of GRBs for which $T_{90}$ is longer than $T_{delay}$ . This plot shows the percentage of high energy emission that will be missed by a telescope with a given delay time (due to slewing and other factors) in our model, after averaging over all Swift bursts.	155
6.3	The mean number of integrated photons above a given energy visible to Fermi per year, up to the maximum LAT energy of 300 GeV. The black line shows the unabsorbed rate, while the blue and orange lines show results with attenuation due to the low and high-peaked EBL models.	157
6.4	The variation in yearly predictions for observations of GeV gamma rays from GRBs with the Fermi LAT. The upper-left plot shows the annual probability of a given number of GRBs occurring in view of the LAT with redshifts between 1 and 6. This does not take into account the expected number of GeV photons from each GRB, which may be less than one. The lower-left plot is the yearly distribution of stacked fluences, normalized to the mean yearly predictions in Figure 6.3. On the right-hand side we show the same quantities computed for a 5-year period.	158
6.5	The number of gamma-rays seen by MAGIC per year, for those years in which at least 1 GRB falls within the field of view of the telescope (see Table 6.3), using parameters $T_{delay}=45$ sec and $\theta_{max} = 40$ deg. Blue and orange lines show the results after attenuation by the low and high-peaked EBL models, respectively. The leftmost bin is the probability of zero photons being received.	164
6.6	As in the previous figure, but showing only the photons from the prompt phase of emission.	165

6.7	Predictions for the spectrum observable by MAGIC from distant GRBs, at 4 different redshifts. The black line is the unattenuated spectrum, and the orange and blue lines show the flux after attenuation by the high-peaked and low EBL models. The fluence is normalized to the average per year, as was done for our Fermi results. However, as we have seen, the year-to-year prediction is highly variable. So the vertical scale of the plot should be taken as arbitrary, and Figs. 6.5 and 6.6 used as a gauge of expected number of counts. . . . .	166
-----	---	-----

# List of Tables

3.1	The integrated flux of the present-day EBL in our three models (fiducial and low with Devriendt dust templates, and fiducial with Rieke templates), over 3 different wavelength ranges. Units are $nW/m^2/sr$ . . . . .	50
4.1	Reconstruction of the VHE spectral indices of a number of blazars using our three EBL realizations. $\Gamma_{obs}$ is the index reported by the given reference at energies between $E_{L\gamma}$ and $E_{H\gamma}$ , reported in TeV. These are taken from the reference if explicitly stated, otherwise the highest and lowest data points presented are used. $\Gamma_{fid}$ , $\Gamma_{low}$ , and $\Gamma_{fid(Rieke)}$ are the average intrinsic indices after de-absorption by our three EBL models presented in the last chapter, over the range of energies claimed in the detections. Errors on this quantity are the same as in the observed indices, if provided by the author. Plus (+) and minus (-) after the source name are used to signify that the detection was claimed in an abnormally high or low state; readers should consult the references given for further details. Many of these reference were taken from Wagner (2008).	
	† The redshift of 3C66A quoted here is based upon two measurements of weak, single emission lines, and is considered uncertain; see reference for details. . . . .	81

5.1	The background models considered in this work. The second and third columns show the star-formation histories and quasar luminosity densities used as inputs in each model. The escape fraction in the last column refers to the values used in calculating the background flux and optical depth to gamma rays in Figs. 5.10 and 5.11, respectively. Our star formation history scenarios are discussed at the beginning of this section. ‘HRH07’ refers to the best-fit model of Hopkins et al. (2007), and ‘SB03 Model C’ to the model in Schirber & Bullock (2003). We have multiplied the latter by a factor of 0.8 to better match the observed quasar luminosity density at low redshift. The escape fraction refers to the attenuation of ionizing photons from star-forming galaxies by neutral hydrogen; attenuation by dust is included intrinsically in our semi-analytic model. . . . .	122
5.2	Here we summarize a broad set of models, and the qualitative level of agreement of each with Ly $\alpha$ forest data, proximity effect measurements, and simulations of total ionizing escape fraction from star-forming galaxies. The numbers of the models shown in Figs. 5.10 and 5.11 are in bold. . . . .	134
6.1	The redshift bins we use in our analysis and the numbers of GRBs and total fluence in each bin for the sample of Swift bursts. The fluences shown are in the BAT energy range, 15–150 keV. These data are over 50 months of observations, from January 2005 to February 2009. . . . .	156
6.2	Some of the parameters we use for calculations of this section. See Sections 6.2.1 and 6.2.2 for more details. . . . .	156
6.3	The annual probabilities of a given number of GRBs falling within a given angle from zenith, assuming a duty cycle of 10 per cent. Under ‘afterglows’, we include all bursts, and for ‘prompt’ only those with $T_{90} > T_{delay}$ . Note that this calculation is for the number of GRBs falling in view of the instrument, and does not predict the number of expected photons, which may be less than one. In Figure 6.5 and 6.6 we show the number of photons received in years with a non-zero (usually 1) number of bursts, using our emission model, and taking into account EBL attenuation and instrument effective area. Based on Equation 6.6, the energy threshold for MAGIC, taken to be 50 GeV at zenith, is 60 GeV at 20 degrees, 78 GeV at 30 deg, and 115 GeV at 40 deg. . . . .	161

## Abstract

Extragalactic Background Light and Gamma-ray Attenuation

by

Rudy C. Gilmore

Attenuation of high-energy gamma rays by pair production with UV, optical and IR background photons provides a link between the history of galaxy formation and high-energy astrophysics. I present new calculations of the EBL from a recent set of semi-analytic models (SAMs), based upon a  $\Lambda$ CDM hierarchical structural formation scenario and employing all ingredients thought to be important to galaxy formation and evolution, as well as reprocessing of starlight by dust to mid- and far-IR wavelengths. These models also use results from recent hydrodynamic galaxy merger simulations. These latest SAMs are successful in reproducing a large variety of observational constraints such as number counts, luminosity and mass functions, and color bimodality. We have created 2 models that bracket the likely ranges of galaxy emissivities, and for each of these we show how the optical depth from pair-production is affected by redshift and gamma-ray energy. Dust reemission in the IR is calculated using 2 different sets of templates. I discuss the implications of these models for blazar observations by current experiments, and compare with other models of the EBL that have been created using different techniques.

The second part of this work focuses specifically on the evolving UV background out to the epoch of cosmological reionization and makes predictions for the

amount of GeV gamma-ray attenuation by electron-positron pair production. This calculation utilizes stellar emissivities from our SAMs along with estimates of quasar emission, and accounts for the reprocessing of ionizing photons by the intergalactic medium. We test whether our models can reproduce estimates of the ionizing background at high redshift from flux decrement analysis and proximity effect measurements from quasar spectra, and identify a range of models that can satisfy these constraints. Pair-production against soft diffuse photons leads to a spectral cutoff feature for gamma rays observed between 10 and 100 GeV. This cutoff varies with redshift and the assumed star formation and quasar evolution models. There are only negligible amounts of absorption for gamma rays observed below 10 GeV for any emission redshift. With observations of high-redshift sources in sufficient numbers by the Fermi Gamma-ray Space Telescope and new ground-based instruments it should be possible to constrain the extragalactic background light in the UV and optical portion of the spectrum.

Gamma-ray bursts (GRBs) may be a source of high-redshift photons above 10 GeV, and could be useful as a probe of the evolving UV background radiation. In the last section of this work, we develop a simple phenomenological model for the number and redshift distribution of gamma-ray bursts that can be seen at GeV energies with the Fermi satellite and MAGIC atmospheric Cherenkov telescope. We calculate the number of gamma rays predicted per year, and show how this result is modified by considering interactions with different realizations of the evolving EBL. We also discuss bright Fermi GRB 080916C in the context of this model. The LAT on Fermi can be expected to see a small number of photons above 10 GeV each year from distant GRBs. Annual results

for ground-based instruments like MAGIC are highly variable due to the low duty cycle and sky coverage of the telescope, however successfully viewing a bright or intermediate GRB could provide hundreds or even thousands of photons from high redshift, which would almost certainly be extremely useful in constraining the high-redshift EBL.

To Mom and Dad

## Acknowledgments

This dissertation was made possible by the and assistance support of many people. I would first like to acknowledge Rachel Somerville, whose semi-analytic models formed the basis for this research. Rachel's care and attention to detail in developing these models have made it possible for me to work with one of the highest quality simulations available, and my work has benefited greatly from our interactions.

I would like to thank Piero Madau and Francesco Haardt for allowing me to use the CUBA code, and answering my many questions about modeling the UV background. David A. Williams has been closely involved in this work and has provided an observer's perspective on many EBL issues. I'd like to thank David for mentoring me throughout my graduate career, from my early summer projects on Milagro, to sitting on my dissertation reading committee. I'd like to thank Nepomuk Otte and Alberto Dominguez Diaz for many useful discussions about EBL topics. Francisco Prada motivated me to do the calculations regarding GRBs, and has served as a mentor on that particular project. Stefano Profumo has provided assistance on this project as well as my earlier work and my job search last fall, and I greatly appreciate his taking the time to serve on my committee.

Finally, I would like to thank my advisor, Joel Primack, for all his support during my time at Santa Cruz. Being able to work with Joel and benefit from his extensive knowledge of astronomy and physics has been an invaluable experience.

An earlier version of the work discussed in Chapters 1 through 4 was presented

at the 4th International Meeting on High Energy Gamma-Ray Astronomy, held 2008 in Heidelberg, Germany, and appeared in AIP Conference Proceedings Volume 1085, p. 71. The material in Chapter 5 is from a paper has been submitted to the journal Monthly Notices of the Royal Astronomical Society.

I received support for much of this work through the National Science Foundation (NSF-AST-0607712), a Fermi Guest Investigator Grant, and a UCSC Regent's Fellowship. My travels to Heidelberg, Germany were supported by a AAS International Travel Grant.

# Chapter 1

## Introduction

The goal of this work is to make predictions for the number density of cosmological background photons emitted by galaxies. This population of photons, often referred to as the extragalactic background light (EBL), is produced mainly by thermal processes as a result of structure formation and exists today at wavelengths from the extreme UV ( $\sim 10$  nm) to the submillimeter ( $\sim 1$  mm). Because the production of the EBL is directly linked to the star formation history of the universe, limits on the EBL can be used to provide constraints on the history of galaxy formation and evolution.

A second focus of this work is on showing how our predicted EBL will impact high-energy astronomy with current and future experiments. The EBL photons form a barrier to high energy (GeV- and TeV-scale) gamma rays, due to interactions that form electron-positron pairs (Section 4.2). These interactions give rise to an optical depth for gamma rays that is a function of energy and source redshift. In the past 10 years, the number of active galactic nuclei (AGN) known to produce gamma rays at

these energies has increased to more than 2 dozen, and it is likely that many more will be found with current and next generation experiments in the near future. Therefore, there has been a growing interest in making predictions of the EBL to understand how observations of high energy gamma rays are being affected, and to allow reconstruction of the intrinsic spectra of these sources. Conversely, the EBL can be constrained by using these gamma-ray observations and assuming reasonable limits on the intrinsic properties of the source. This technique has been used in several cases in the past few years to set fairly tight upper bounds on the background flux, and will become more powerful as gamma-ray sources become better understood in the future.

The remainder of this chapter will be devoted to a general discussion of the EBL, including an overview of measurements and how the EBL relates to cosmological questions. In Chapter 2, we will discuss the techniques that have been used to create evolving models of the EBL, and then address the details of the semi-analytic model and dust emission templates used as the basis for this work. Comparisons of the model with astrophysical observables will be the main focus of Chapter 3. In Chapter 4, we will begin with an introduction to studies of the EBL through gamma-ray observations, and present attenuation results for known AGN sources in the context of our EBL model, as well as a comparison with other recently-published models. The work of the first four chapters focuses mostly on the EBL resulting from direct starlight and dust reemission. Understanding the UV background presents several theoretical challenges, such as the inclusion of quasar emission in the model, and the processing of ionizing photons by neutral hydrogen. Chapter 5 will discuss results of a calculation specifically focusing on

the high-redshift UV and optical background, which is of interest to GeV-scale gamma-ray experiments such as Fermi and ground-based telescopes with low energy thresholds. The work in this chapter is intended to supplement our results for the lower redshift optical and IR backgrounds, and extend our gamma-ray attenuation results to the high-redshift regime. An exciting possibility is to use distant gamma-ray bursts (GRBs) as a probe of this background. In Chapter 6, we will present a simple phenomenological model of GRB emission, and show the effects of the EBL models developed in Chapter 5 on these observations. Chapter 7 presents conclusions for this work and some brief comments on future directions of research.

## 1.1 Defining the EBL

The extragalactic background light can be defined in a couple of ways that are nearly equivalent. The most intuitive definition is that the EBL is the population of UV, optical, and IR photons averaged over a cosmological volume that is large enough to be homogeneous. A second, more functional definition is that the EBL is the average flux observed on the sky after all foreground sources within our galaxy are subtracted<sup>1</sup>; these foreground sources include stars, infrared emission from the interstellar medium (ISM), and scattered or re-emitted light from the dust in our solar system, which is often referred to as the zodiacal light. The reason these definitions might be slightly different is

---

<sup>1</sup>A word on terminology: the phrase ‘extragalactic background light’ is based on this observational definition, and therefore carries the connotation that it is the local ( $z = 0$ ) background that is being observed. When modeling the background in existence at previous epochs, other authors sometimes use terms such as ‘evolving background flux’ or ‘metagalactic radiation field’ to make it clear that they are including the unobservable nonlocal radiation as well. In this work, we will be a bit more relaxed in our definition, and use ‘EBL’ to refer to both local and non-local flux, being more explicit if necessary.

that our galaxy, the Milky Way, is not located at a point in the universe which is average with respect to structure distribution, but this is a relatively minor effect. The EBL is just one of several background populations that exist in the universe. This includes other photon wavelengths such as the cosmic microwave background (CMB) and the diffuse gamma-ray background, as well as non-photon backgrounds such as neutrinos and that of hypothesized gravitational waves. As with these other background populations, we expect the EBL to be isotropic and homogeneous on large scales, specifically greater than those on which galaxies cluster.

One important difference between the EBL and the well-known CMB is that while the latter is produced over a very short period in cosmological time, the production of the EBL has taken place over most of the history of the universe, and its emission continues at the present. Over this time, it is simultaneously being modified by cosmological redshifting that transfers energy to longer wavelengths. At non-ionizing wavelengths we assume EBL photons evolve passively after leaving their galaxies, however ionizing photons are reprocessed by the intergalactic medium and may be emitted at longer wavelengths, an idea we will address in Chapter 5. The fact that the EBL is created by an evolving population of sources explains some of the difficulty in predicting the EBL with theoretical models. In the local universe, the galaxies and quasars that create the EBL are readily observable and fairly well-understood on the individual level. However, it is the evolution of these sources that must be understood across cosmological history, and this is where a great deal of uncertainty still exists.

## 1.2 Measurement of the EBL

In this section, we outline the measurement techniques which have been used to determine the observed local EBL. Attempts to model the evolving EBL, based on inferred or observed source populations, will be treated separately in Chapter 2. The values of most of the measurements mentioned in the following paragraphs are shown as data points in our main plot of the EBL spectral energy distribution (SED), Figure 3.9.

### 1.2.1 Direct Measurement

The most straightforward way to determine the EBL is by absolute photometry of the sky at the desired wavelength. Measurement of this light through direct observation is complicated by foreground emission from our own galaxy and reflected zodiacal light from our sun, which are much brighter than the EBL across most of the optical and IR spectrum (Hauser & Dwek, 2001, for review). Interplanetary dust is the major contributor of foreground light at most wavelengths, with starlight becoming substantial in the optical and near-IR, and the interstellar medium most important in the submillimeter regime. Another instrumental difficulty for absolute measurements comes from maintaining the zero-point calibration of the detector, which plagued many experiments not specifically designed for these types of measurements.

The EBL in the optical has been estimated using Hubble Space Telescope (HST) observations (Bernstein et al., 2002a,b) by taking direct measurements in 3

bands, and subtracting away the zodiacal and galactic contributions. The detection of the EBL presented in these works was based on two methods. The first involved measuring the photometry of the sky with the HST Wide Field Planetary Camera 2 (WFPC2), and subtracting off foreground sources determined using ground-based observations and modeling. The second method set a lower bound on the EBL using an ‘ensemble photometry’ technique to extract light from the edges of resolved sources; these methods were combined to arrive at a  $1-2\sigma$  detection of background. An update to this paper (Bernstein, 2007) responded to criticisms of the sky subtraction methods used, and the updated results were significantly higher than those of the 2002 papers. However, the authors claim that these results are consistent with findings from integrated number counts (Madau & Pozzetti, 2000) given the small significances of the detections in both cases.

Many early attempts to measure the IR background were done using rocket-borne experiments (e.g, Matsumoto et al., 1988; Kawada et al., 1994). These suffered from a limited time of observation, as well as a variety of systematic errors, including possible significant contamination due to thermal emission from the rocket itself. The Infrared Astronomy Satellite (IRAS), launched in 1983, was the first instrument to fully survey the infrared sky in 5 wavelengths spanning the mid- to far-IR. However, it lacked the means for zero-point calibration, and was unable to claim an EBL detection due to uncertainties in the measured flux (Rowan-Robinson et al., 1990).

The most robust direct measurements of the IR background to date come from the Diffuse Infrared Background Experiment (DIRBE) and Far-Infrared Absolute

Spectrophotometer (FIRAS) instruments on the Cosmic Background Explorer (COBE) satellite, though they are still fraught with uncertainty in sky subtraction. DIRBE was specifically designed to measure the background radiation in 10 bands across the IR from 1.25 to 240  $\mu\text{m}$ . Ultimately it was most successful in the near- and far-IR wavebands, where the zodiacal light contribution is lowest (see Figure 2 in Hauser & Dwek (2001)). The near-IR flux has been calculated from DIRBE observations by a variety of authors (Wright & Reese, 2000; Wright, 2001; Gorjian et al., 2000; Cambrésy et al., 2001; Levenson et al., 2007) using foreground source subtraction techniques and modeling of the zodiacal light, and has generally yielded high estimates in this range compared to number counts. Another near-IR measurement was done using the Infrared Telescope in Space (IRTS) on the Space Flyer Unit satellite. Based on these observations, Matsumoto et al. (2005) claimed an even higher background level than most of the DIRBE analyses below 2  $\mu\text{m}$ , at a level that would require a large contribution from an as-of-yet undetected source type. Part of the scatter seen in the reported results of different authors can be traced to the model of zodiacal light used in each case. The papers associated with Wright and Gorjian have applied the zodiacal light maps of Wright (1998), with the foreground light from stars removed for various regions of the sky. Those of Cambresy and Matsumoto have used the Kelsall et al. (1998) zodiacal model, which gives a lower zodiacal intensity at all 3 near-IR bands, and therefore a higher background remaining after subtraction. It is argued in Levenson et al. (2007) that these near-IR results are all consistent with each other after the differences in zodiacal model are taken into consideration.

In the far-IR regime, observations from FIRAS (Fixsen et al., 1998) and DIRBE (Hauser et al., 1998) provide direct measurements of the background radiation. At shorter wavelengths (60 and 100  $\mu\text{m}$ ), where foreground contamination has more of an impact, the DIRBE instrument can only place upper limits on the background. Analyses of the DIRBE data at far-IR wavelengths have been attempted by other authors using new models for the zodiacal light and instrument calibration (Finkbeiner et al., 2000; Lagache et al., 2000; Wright, 2004). The rather high detection claimed by Finkbeiner et al. at 60 and 100  $\mu\text{m}$ , which required careful subtraction of the bright foreground, has been disputed by other authors (Puget & Lagache, 2001).

### 1.2.2 Number Counts

Integration of galaxy counts (galaxies per unit sky area at a given magnitude) is a way to set firm lower limits on the EBL, although the degree to which these measurements converge on the true value generally remains controversial. If the EBL is created by discrete sources such as galaxies, then it should be possible to identify all of the sources contributing to the present day EBL in an image of sufficient depth and resolution. The flux from faint sources will converge mathematically if the slope of the counts plotted on a log number vs flux diagram is flatter than unity, or in terms of magnitudes if  $\alpha < 0.4$ , for  $\ln(N) \propto \alpha m$ . Seeing this flattening behaviour for the faintest observable counts in a given survey may suggest a finite contribution from integration of unobservable sources, however there is no guarantee that number counts do not exhibit an upturn at magnitudes beyond the resolution limit, or that whole new classes of

unresolved objects do not exist. As expounded by Bernstein (2007), photometry of faint galaxies is fraught with difficulty in untangling the faint galactic fringes from the background, and it is possible to miss 50% or more of the light associated with the extended source in simple aperture photometry. Measured luminosities of galaxies in the Hubble Deep Field (HDF) (Madau & Pozzetti, 2000) place a lower bound on EBL fluxes in the 0.4-1  $\mu\text{m}$  range, a much lower level than that proposed in the Bernstein papers. This paper also uses Two-micron All Sky Survey (2MASS) data to extend counts to 3  $\mu\text{m}$ . It is argued in this work that the flatness ( $\alpha < 0.4$ ) of the faint counts in all bands indicate convergence, and therefore a low EBL across the optical and near-IR. The difference between the low EBL in number counts and the much higher Bernstein points can be accounted for by either an unresolvable diffuse source of background photons, or an underestimation in the determination by HST counts of the integrated light from faint sources. A similar analysis conducted using IR data from the Subaru deep field (Totani et al., 2001) modeled possible selection effects and supported the conclusion of a low optical–near-IR background compared to many of the direct detection claims.

In the UV, limits exist from GALEX (Xu et al., 2005) and observations of the HDF with the STIS instrument (Gardner et al., 2000), with the latter finding a considerably higher bound on the EBL at two UV wavelengths. The STIS EBL determination also used data from the balloon-based FOCA experiment to find bright counts, and this experiment found a higher level of counts than the GALEX experiment at several magnitudes. The IRAC instrument on *Spitzer* has placed lower limits on several bands in the near- to mid-IR (Fazio et al., 2004), which similarly are well

below the IRTS and DIRBE direct detection fluxes. In a complementary approach to their DIRBE sky-subtraction papers, Levenson & Wright (2008) used IRAC data to calculate the best-fit flux at  $3.6 \mu\text{m}$  using a profile-fit to estimate the light from the unobservable faint fringes of galaxies, and a broken power law model for the number count distribution. Profile fits were based on GIM2D (Simard et al., 2002), which uses a 12-parameter model for each source. This is used with Monte Carlo methods to find the most probable contribution from galaxies. This method yielded results nearly 70% higher than the corresponding IRAC aperture measurement, though at a level lower than most DIRBE direct photometry measurements. ISOCAM on the Infrared Space Observatory (ISO) and the MIPS instrument on Spitzer have reported lower limits from number counts at 15, 24, 70, and  $160 \mu\text{m}$  (Elbaz et al., 2002; Chary et al., 2004; Frayer et al., 2006; Papovich et al., 2004; Dole et al., 2006). Galaxy counts from the SCUBA instrument provide a lower limit at  $850 \mu\text{m}$  (Coppin et al., 2006), with an estimated 20 to 30% of the background at these wavelengths resolved into point sources.

### 1.2.3 Fluctuation Analysis

Measurement of the power spectrum present in sky brightness images is another way to constrain the EBL. While this alone does not provide an absolute measurement of the EBL, fluctuation measurements can be used with other data such as number counts to constrain the amount of light from unresolved sources. Kashlinsky et al. (1996b) analyzed the DIRBE near-IR bands in this way and reported upper limits in the EBL, and Kashlinsky et al. (1996a) and Kashlinsky & Odenwald (2000) extended

this work to all DIRBE bands, including the mid-IR where the zodiacal light makes direct photometry extremely difficult. The upper limits for all wavelengths were quite high compared to the findings in most recent models. Matsuhara et al. (2000) examined fluctuations seen in 170  $\mu\text{m}$  ISO measurements, and calculated lower limits including flux from sources below the instrument's detection threshold. More recently, attention has been paid to possible fluctuations due to primordial population-III (pop-III) stars in the near-IR background. The claims by Kashlinsky et al. (2005) of a high detection here have been disputed on cosmological grounds, as we discuss below.

### 1.3 The EBL and Cosmology

The EBL provides an important test of star-formation observations; if there is a large gap between the flux from sources in deep surveys and direct measurements, then an unresolved population must exist to provide the missing energy. The present-day EBL is linked to the history of star formation through the stellar initial mass function (IMF), as well as the evolving metallicity and dust distribution, as we will discuss later. It is well established that star formation rates per unit cosmological volume were much higher in the past, peaking at roughly  $z \sim 2$  (Hopkins, 2004; Gabasch et al., 2004; Hopkins & Beacom, 2006). Studies of the buildup of stellar mass have typically found that the integrated star formation rate tends to exceed stellar mass as measured by IR (fossil) light from old stars, with the discrepancy becoming worse with redshift. The local star-formation rate is typically measured from the strength of the  $\text{H}\alpha$  (Balmer) line. At

higher redshift, other tracers must be used. These can include UV continuum emission corrected for dust, radio emission by supernovae remnants, emission lines which are excited by UV radiation from young stars, or measuring reprocessed light from dust in the infrared. All of these methods are fraught with uncertain amounts of contamination from quasars and biases from dust and metallicity, and different methods can produce widely varying results for the same galaxy. An overview of these issues can be found in Hopkins & Beacom (2006). One solution to the SFR–fossil mass discrepancy may lie in a variable IMF which suppresses formation of low mass stars in starbursts occurring primarily at higher redshift (Fardal et al., 2007; Davé, 2008). In this way, high mass stars that produce tracers of star-formation rate could be produced at a high rate while lower mass stars that account for most of the integrated stellar mass are created in smaller quantities. Alternatively, it is possible that systematic biases in determinations of the star formation rate at increasing redshift are responsible for the discrepancy. This can be phrased in terms of measurements of Davé’s star-formation activity parameter, which determines the Hubble times required for galaxies to reach their current mass at current SFR, and is seen to decrease too much between present day and  $z \sim 2$ . This conflicts with model predictions, and the passive population that would be required to counterbalance the high star formation in these rapidly growing systems is not observed. The recent work of Chen et al. (2009) has found lower specific star formation rates in galaxies from the SDSS and DEEP2 surveys than typically measured by more usual means using an alternative method based on higher order Balmer lines. The lower normalization found in this model can be attributed to a number of factors, though the

possibility of a changing IMF cannot be ruled out.

Unresolved pop-III stars could in principle provide a large contribution to the background light. The near-IR peak observed by the IRTS satellite (Matsumoto et al., 2005) has been interpreted as the redshifted photons from massive population-III stars beyond redshift  $\sim 9$  (Salvaterra & Ferrara, 2003). This peak reaches nearly a factor of 10 higher than levels from resolved number counts. Therefore this claim is at odds with Madau & Pozzetti (2000) and Totani et al. (2001), who argue that the contribution from resolved galaxies has nearly converged, and there is little room for any additional sources such as an early generation of stars with a top-heavy IMF. The background fluctuation analyses of Thompson et al. (2008) and Cooray et al. (2007) dispute the finding of a large contribution from these epochs. The high levels of metal formation from massive stars in these models would require metals to either be locked away in compact products or dispersed in the IGM in a very inhomogeneous fashion. The large fraction ( $\sim 10\%$ ) of baryons which would have to be processed through primordial stars, and the lack of J-band dropout detections of these sources have strongly disfavored this interpretation (Salvaterra & Ferrara, 2006; Dwek et al., 2005), as does the amount of material that would have to be locked away in intermediate mass black holes (Madau & Silk, 2005). Additionally, if this near-IR flux was extragalactic in origin, then it would have a huge impact on the optical depth of TeV gamma rays, as we will discuss in later chapters.

In addition to the global star formation rate of the universe, the stellar environment can play an important role in determining the spectral energy distribution

(SED) of the EBL. The processing of starlight by dust is crucial to our understanding of this characteristic double-peaked distribution. The far-IR peak contains roughly the same total energy density as the optical and near-IR peak (Hauser & Dwek, 2001; Dole et al., 2006), while the Milky Way and most other nearby galaxies emit the majority of their light in the optical. Because the well-constrained  $z=0$  luminosity density of the universe has only one-third as much light in the far-IR as in the optical (Soifer & Neugebauer, 1991), there must have been a strong trend towards increased far-IR production at higher redshifts. It has recently been determined that this part of the background is largely produced by a population of (ultra) luminous infrared galaxies ((U)LIRGs) (Lagache et al., 2005; Puget et al., 1996; Dole et al., 2006), which are dust-shrouded, starbursting galaxies whose numbers increase rapidly with redshift. The rapid star-formation in these galaxies is heavily obscured by dust, and most stellar light undergoes re-radiation in the IR; there may also be a subdominant contribution from active galactic nuclei (AGN). The flux at  $850\mu\text{m}$  from sources observed by the SCUBA instrument seems to arise largely from these types of sources at high redshift,  $z > 1.3$  (Dye et al., 2006; Devlin et al., 2009).

# Chapter 2

## EBL Modeling

### 2.1 Techniques

Modeling the EBL, and calculating its evolving spectral energy distribution (SED) is a matter of quantifying the emission of sources responsible for its production, and integrating over cosmic time. This has been done in a number of ways by different authors. As enumerated in Kneiske et al. (2002), techniques for determining the EBL fall into three general categories: **i)** interpolating and extrapolating from direct observation of luminosity functions or inferred star formation rate; **ii)** backwards evolution of the well-constrained present-day galaxy emissivity according to some prescription; and **iii)** forward evolution beginning with initial cosmological conditions, such as the semi-analytic models used in this work. We will discuss some modeling efforts that have focused specifically on the UV background in Chapter 5.

### 2.1.1 Observed Evolution

Deriving the EBL from galaxy observations has become a much more powerful technique in recent years due to large-scale surveys by ground- and space-based instruments. This is especially true at UV and IR wavelengths, where a great deal of progress has taken place in the last decade. Madau et al. (1998) made predictions from the emission and star-formation history seen in the galaxy population by HST, while Franceschini (2001) made IR predictions based on ISO data. A model based on the chemical enrichment history seen in Ly $\alpha$  systems was proposed by Pei et al. (1999), who found a background flux level near that set by number counts. A two-part paper series by T. Kneiske and collaborators (Kneiske et al., 2002, 2004) computed the EBL and subsequently predictions for attenuation of gamma-ray sources based on observed galaxy emissivity. These models separately include the contribution of the LIRG/ULIRG population. A sophisticated model using observed luminosity functions was recently published by Franceschini et al. (2008) which calculates the EBL and gamma-ray attenuation. This model uses evolving luminosity functions and synthetic SEDs for three different galaxy populations (spiral, spheroidal, and starbursting galaxies) to find total emissivity.

### 2.1.2 Backwards Evolution

Other authors have used backward evolution models to predict the EBL. These calculations begin with the present day galaxy luminosity function and attempt to trace this function backwards in time by assuming a functional form for the redshift evolution.

Emission at other wavelengths can be calculated using libraries of spectra based on observations of local galaxies. In Malkan & Stecker (1998), IR luminosity functions from IRAS were extrapolated backwards in redshift using power law functions, and in Malkan & Stecker (2001) the luminosity functions and counts predictions at other wavelengths were shown for this model. The model of Stecker et al. (2006) updated this previous work and determined the EBL below the Lyman limit (13.6 eV) in two different cases of stellar evolution. The model of Rowan-Robinson (2001) also utilized a 60  $\mu\text{m}$  evolving luminosity function, and a four-component spectral model for IR and optical emission. One potential problem with this method is that it has difficulty accounting for the emissivity contribution of merger-triggered starbursts, believed to occur increasingly with redshift. An attempt to account for this starburst phase using ISO data and dust modeling was done in Franceschini et al. (2001).

### 2.1.3 Forward Evolution Models

In forward evolution scenarios such as semi-analytic models (SAMs), predictions for evolution of galaxy emissivities are made by beginning from the universe in its primordial state and simulating the process of galaxy formation. This is considerably more involved and challenging than the other methods of estimating the EBL, but can provide a degree of insight into the fundamental astrophysics processes that determine the emissivity that is lacking in other calculations. These types of calculations have their roots in spectral synthesis models such as Partridge & Peebles (1967) and Yoshii & Takahara (1988), or more recently Franceschini et al. (1994), which focused on re-

radiated emission from dust in a similar way to calculate the IR background. These were ‘pure luminosity evolution’ models which calculated the output from galaxies existing today at past redshifts. These models were limited because they did not take into account mergers, or attempt to treat star formation realistically as being driven by the cold gas available. The treatment of galaxies as non-interacting systems is now known to be an incorrect premise, as a model of galaxy formation must account for merging and hierarchical growth of these systems. The development of Cold Dark Matter (CDM) and Cold-Hot Dark Matter (CHDM) (Blumenthal et al., 1984; van Dalen & Schaefer, 1992) lead to a new class of models in which galaxy properties were modeled using ‘semi-analytic’ techniques within the dark matter framework.

The use of semi-analytic models to study galaxy formation was developed by White & Frenk (1991), and initial work was carried out primarily by two groups based in Durham (e.g. Cole et al., 2000; Benson et al., 2002, 2003) and Munich (e.g. De Lucia & Blaizot, 2007; Bertone et al., 2007). Generally, SAMs are based on N-body simulations of cold dark matter halo formation and mergers, or alternatively, upon a description of the density of these halos modeled using Press-Schechter theory (Press & Schechter, 1974). From here, prescriptions are used to trace the formation and evolution of galaxies which inhabit these halos, accounting for all aspects of galaxy formation such as gas cooling and dissipation, star formation rate, chemical abundance evolution, and supernovae feedback.

Several papers reporting results for the EBL have been produced since then by the ‘Santa Cruz’ group which became active soon afterwards. The first of these calcula-

tions was MacMinn & Primack (1996), which considered standard ( $\Omega_m = 1$ ) CDM and CHDM cosmologies. Each dark matter halo, as determined by Press-Schechter theory, was occupied by a single galaxy, with luminosity determined as a function of halo mass. Stellar populations were modeled as a simple blackbody emitter, and 3 different stellar initial mass functions (IMFs) were considered, including a Salpeter ( $N(M) \propto M^{-2.35}$ ) (Salpeter, 1955) and two steeper power law forms. Dust absorption was accomplished by assuming a Galactic extinction curve and scaling according to metallicity. This paper found that dark matter cosmology played a larger role in determining the near-IR background than did choice of stellar IMF. In a CHDM cosmology, galaxies form later and produce less light overall, particularly in the near-IR, which was of particular interest at this time due to the recent discovery of blazar Mrk 421 at TeV energies. This model found less attenuation of gamma-rays from this source than other contemporary calculations such as Stecker & de Jager (1997).

The EBL calculated in Primack et al. (1999) used an updated SAM, described in Somerville (1997), Somerville & Primack (1999), and Somerville et al. (2000). This model was based on a ‘merger tree’ construction for each halo, which accounted for the merger history of the halo and its resident galaxy. As demonstrated in Somerville & Kolatt (1999), the Monte-Carlo realizations of these trees were in good agreement with results from collisionless N-body simulations. This technique allowed mergers to be included as a fundamental component in the model: galaxies began as disks, and then spheroids formed during major (approximately equal mass) mergers. Stars formed out of gas that cooled into a gaseous disk at the center of each halo, and supernovae

regulated this process by heating and expelling gas. The spectral output was determined based on Salpeter and Scalo IMFs using the GISSEL98 population synthesis model. As in MacMinn & Primack (1996), cosmology was found to play an important role in the EBL formation. This model did not include the increasing far-IR contribution with redshift from starbursting (U)LIRGs, and predicted significantly less flux than seen by DIRBE.

In Somerville et al. (2001), these models were combined with the improved dust emission code of Devriendt et al. (1999) and Devriendt & Guiderdoni (2000) for a prediction of the EBL and absorption of gamma rays (Primack et al., 2001). At the 2004 Symposium on High Energy Gamma-ray Astronomy, another model was presented with a modified spectrum and attenuation predictions (Primack et al., 2005). This SED was somewhat lower than the 2001 result, primarily because the model had been recalibrated to fit the local luminosity density as determined by new surveys such as 2MASS (Cole et al., 2001), SDSS (Blanton et al., 2003), and 2dF (Norberg et al., 2002). While the prediction of this model was consistent with optical and near-IR integrated number counts, it was below both the ISOCAM lower limit at  $15 \mu\text{m}$  and well below the direct detection fluxes of DIRBE and FIRAS in the far-IR, which indicated that the light remission by dust was being significantly underpredicted.

#### **2.1.4 Recent Challenges for Semi-Analytic Modeling**

The discovery of color bimodality by large-scale galaxy surveys such as SDSS is a problem in which progress has been made in the last few years using semi-analytic

methods. Bimodality, in which most galaxies fit conclusively onto a red sequence or blue cloud in color-magnitude space, is also seen in a variety of other facets, including the luminosity function (Bell et al., 2003), the stellar age and recent star-formation rate (Kauffmann et al., 2003), and gas mass fraction (Kannappan, 2004). A problem that has traditionally plagued semi-analytic models is the overproduction of large, star-forming, blue galaxies. Introducing the correct mechanisms to quench star formation in high-mass systems has been a major challenge for modeling, with obvious consequences for EBL predictions.

Stars preferentially inhabit systems in a relatively narrow mass range around a stellar mass of  $3 \times 10^{10} M_{\odot}$ , or halo mass of  $10^{12} M_{\odot}$ . In halos substantially above or below this number the mass-to-light ratio is seen to rapidly increase. This contrasts with the shape of the dark matter halo mass function, which features a broader distribution with both a shallow power-law cutoff at the high end and a steeper small-mass end (Benson et al., 2003). Larger galaxies tend to be red and consist of older stellar populations, while smaller galaxies are bluer and forming stars. Some faint galaxies in overdense environments also appear to have moved to the red sequence (Blanton et al., 2006), and thus an environmental bimodality exists as well. This red sequence of massive galaxies is seen to exist out past redshift 1; at still higher redshifts large galaxies which are likely the progenitors of these objects exhibit rapid star formation (Bell et al., 2004; Shapley et al., 2004). There are a number of known mechanisms which are capable of quenching the supply of gas that drives star formation. In smaller systems this can include the photoionization heating of gas (Quinn et al., 1996b), and supernovae-driven

winds in larger systems (Dekel & Silk, 1986; White & Frenk, 1991). Understanding the role of super-massive black-hole driven AGN is now thought to be key to the regulation of growth in the largest galaxies. Including AGN feedback in SAMs has allowed theorists to create galaxies that move to the red sequence at the correct mass scale. Recent simulations suggest a scenario in which galaxies cease to form stars after reaching a critical halo mass (Croton et al., 2006; Cattaneo et al., 2006, 2008). The mechanism is feedback from AGN ‘radio mode’ accretion, which is associated with static hot gas halos surrounding galaxies and prevents the condensation of cold gas which would fuel star formation. This mode distinguished from the quasar-like optical mode spurred by the merging of halos. While AGN of this type do not produce great amount of optical or x-ray emission, they are efficient at producing relativistic particle jets that create radio lobes, and it therefore by their radio emission that AGN in this class are usually identified. Unlike other feedback mechanisms, radio-mode accretion is not dependent upon continued star formation. Galaxies which are above this mass will continue to grow via gasless ‘dry’ mergers. Lower mass galaxies can also join the red sequence if they find themselves as satellites of a halo above the threshold, and galaxies in this situation form the faint end of the continuum (Blanton et al., 2006).

Correctly matching the anti-hierarchical growth of galaxies seen in observations is an ongoing challenge for semi-analytic models. Studies of the buildup of stellar mass typically find that larger galaxies build up their mass earlier than smaller systems, a phenomenon often referred to as ‘downsizing’. Fontanot et al. (2009) discusses this issue for three current semi-analytic models, including the one used in this work

(Somerville et al., 2008). This paper finds that all of the models have difficulty correctly predicting star formation in low mass galaxies. These galaxies form too early, and therefore do not have enough star formation at low redshift. The nature of the physical basis for correctly regulating star-formation in these galaxies remains an open question; the current implementation of supernovae feedback in the models does not produce correct results.

## 2.2 The Semi-Analytic Model

This section summarizes the semi-analytic model that is used to predict the EBL in the current model. This model is based upon the code described in Somerville & Primack (1999) and Somerville et al. (2001), with several updates and new capabilities. Readers should refer to Somerville et al. (2008) (S08) for a much more detailed account.

One of the advantages to the semi-analytic technique is that the model produces galaxy populations which can be compared to a wide variety of measurements. This allows the model to be verified along many different observational dimensions, which is an essential step to constraining the large number of parameters that go into the calculation. S08 discusses many of these comparisons with data, including stellar metallicity and ages, cold gas fractions and specific star formation rates across the galaxy population, and the stellar mass function. In the next chapter, we present many results related to the EBL such as observed number counts in several bands, local luminosity functions, and total luminosity density. We also revisit the issue of the global

star formation history in the model. While these measurements of the local universe have been used to calibrate the model, we have not used the EBL flux itself as a means of normalizing the inputs. The background flux presented in the next chapter should therefore be understood as a prediction of the model that follows from choosing inputs in such a way that the properties of the modeled galaxy population closely match observations.

### 2.2.1 Overview

We assume a standard  $\Lambda$ CDM universe and a Chabrier stellar initial mass function (IMF) that does not evolve in redshift. Two models are presented in this work. Our ‘fiducial’ model is based upon a concordance cosmology with  $\Omega_m = 0.3$ ,  $\Omega_\Lambda = 0.7$ ,  $H_0 = 70.0$ , and  $\sigma_8 = 0.9$ . Our ‘low’ model adopts the best fit values from WMAP3 for these parameters, with  $\Omega_m = 0.2383$ ,  $\Omega_\Lambda = 0.7617$ ,  $h = 0.732$ , and  $\sigma_8 = 0.761$ . The most relevant difference in this work is the value of the power spectrum normalization  $\sigma_8$ . The lower normalization of the primordial power spectrum in the ‘low’ model leads to delayed structure formation and decreased luminosity densities at high redshifts.

The SAMs used here are based either upon the merger history of the dark matter halos seen in N-body simulations or, in the case of the low model, the extended Press-Schechter method described in Sheth & Tormen (1999). This latter model provides the number of dark matter halos as a function of mass for a desired redshift. For each present-day halo, a merger ‘tree’ is constructed, using the method similar to that described in Somerville & Kolatt (1999). The merger trees track the buildup of dark

matter mass, with junctions representing halo mergers which form larger, virialized halos. The NFW profile (Navarro et al., 1997) is used as the initial halo description with the concentration determined using a fitting formula based on Bullock et al. (2001). The model does not account for scatter or merger history in determining concentration. These methods do allow tidal disruption and destruction of halos in minor mergers to be considered; if a halo is destroyed prior to merging, its stars join a diffuse stellar component around the central galaxy.

Gas can be accreted by the galaxy and becomes available for star-formation after cooling via atomic processes. Gas which cools around the potential well of a halo is assumed to initially fall into a thin disk with an exponential profile. The scale radius of this disk is determined using conservation of angular momentum and the concentration and baryon fraction of the disk. Our model computes the cooling time for gas based upon density, metallicity, and the initial virial temperature. Our recipe agrees well with gas infall and cooling rates from 3-D hydrodynamic simulations of cold and hot flows (Birnboim & Dekel, 2003; Dekel et al., 2009; Keres et al., 2008). Feedback from supernovae can heat the cold gas reservoir and drive it from the galaxy. This gas will either be deposited in the hot reservoir of the galaxy, or returned to the IGM, depending on the wind velocity relative to the virial velocity of the halo. Ejected gas can cool and return to the galaxy on a timescale roughly equal to the dynamical time of the galactic halo. The model discriminates between cold- and hot- mode accretion of gas based on the relative values of the cooling time of the gas versus the dynamical time of the halo.

Star-formation in our model occurs in two regimes, quiescent star-formation

in non-interacting galaxies and merger-driven starbursts. The former is treated using a recipe based on the Schmidt-Kennicutt law (Kennicutt, 1989; Kennicutt et al., 1998)

$$\dot{\Sigma}_{SFR} = A \Sigma_{gas}^{\alpha} \quad (2.1)$$

where  $\dot{\Sigma}_{SFR}$  is the star formation rate per unit area and  $\Sigma_{gas}$  is the gas surface density in the disk, and  $A$  is a normalization factor. In this model, we assume a slope  $\alpha = 1.4$  and normalization to the Chabrier IMF. Star formation is assumed to cut off below a specific surface density, giving the exponential galactic disks corresponding radius within which stars are forming. Merger-driven bursts are parametrized by the mass ratio of the merging pair, the mass in this case being the total mass in the inner part of the halo, taken to be twice the characteristic NFW scale radius. The burst efficiency parameter determines the fraction of cold gas converted to stars in the burst, and no burst occurs for a mass ratio of less than 1 to 10. The functional form taken for this parameter is from Cox et al. (2008). The star-formation rate (SFR) during the burst is proportional to the available fuel, and therefore takes the form of a decaying exponential after an event. Details of the functional forms for the burst efficiency and timescale can be found in Somerville et al. (2008). Chemical enrichment takes place instantaneously, and the effective yield is a free parameter in the model. The metallicity and star formation history of each galaxy are used to predict the total emission spectrum. This is done making use of the Bruzual & Charlot (2003) population models. Light emitted by stars can be absorbed and reemitted by dust, as described in the next section.

The model accounts for the release of energy by the growth of supermassive

black holes at the center of galaxies and the effect of this AGN feedback on the galaxy. Every top-level halo in the simulation begins with a seed black hole of 100 solar masses; results are not found to be sensitive to this specific mass. The implementation of AGN feedback is similar in many respects to that of Sijacki et al. (2007), in which AGN operate in ‘bright’ and ‘radio’ modes, with the former being switched on when the accretion rate rises above a critical value. This bright mode is equivalent to a classical quasar mode, with bright optical to X-ray emission. This phase can rapidly remove cold gas from a galaxy, but only occurs over a small fraction of the galaxy’s lifetime. All bright mode accretion is triggered by galaxy mergers, and the interdependent processes of AGN activity and black hole growth are based upon results from a large suite of hydrodynamic simulations. Black holes in merging galaxies coalesce rapidly and the product grows at the Eddington rate until reaching a critical ‘blowout’ mass, after which the accretion rate falls as a power law, until it is cut off completely upon attaining a final mass determined by the spheroid mass and gas fraction. Radiative momentum from the accreting black hole is transferred to the galactic wind via an assumed coupling efficiency. In radio mode, the black hole enters a phase of Bondi-Hoyle accretion (Bondi, 1952). The net cooling in this mode is the cooling rate minus the heating from Bondi accretion. Heating is ignored if the cooling time is shorter than the dynamical time of the halo (‘cold mode’ cooling).

### 2.2.2 Dust Absorption and Re-emission

Dust plays a crucial role in determining the SED of galaxies, by absorbing energy at optical and UV wavelengths, and re-emitting this energy at IR wavelengths. Unfortunately, most of what we know about the distribution of dust in galaxies is from observations that are limited to the Milky Way (MW) and other local galaxies. The detection of the EBL in the far-IR by DIRBE and FIRAS at a level comparable to the direct emission from starlight requires the inclusion of galaxy populations very different from the local galaxies, which emit most light in the optical and near-IR. Detectors in the mid-IR such as ISOCAM and MIPS find significant IR emission from star-forming galaxies (e.g. Reddy et al. 2006; Elbaz et al. 2005). These (U)LIRGS are very dusty and compact, and can emit more than 90 % of their energy in the far-IR, while this ratio for a galaxy like the MW is less than one-third. The cause of this reddening is primarily tiny particles of dust released in supernovae explosions, with typical sizes ranging from nanometers to tenths of a micron. The temperature of these grains is only weakly affected by the flux of the surrounding radiation field, due to the blackbody emission which increases as the 4th power of temperature and the falloff of emission at long wavelengths, and therefore the peak emission wavelength ranges over a relatively small range due to galaxy luminosity, from about about 170 microns for a Milky Way type spiral to 60 microns for a ULIRG (Lagache et al., 2005). Polycyclic aromatic hydrocarbons (PAHs) are another class of absorbers. These are molecules which emit at a group of specific wavelengths in the mid-IR from 3 to 17 microns.

To calculate absorption in the SAM, dust is modeled as a two-component distribution, using the prescription of Charlot & Fall (2000), which treats individually the dense dust in giant molecular clouds that contain forming stars and the much more diffuse cirrus clouds in the interstellar medium. The metallicity is tracked both in the stellar spectra and surrounding gas, with predictions for radiative transfer based on geometry and metal distribution modeled after the MW and nearby galaxies. Galaxies in the simulation are assumed to have random inclinations. The  $V$ -band, face-on extinction optical depth of the diffuse dust is given by

$$\tau_{V,0} \propto \frac{\tau_{\text{dust},0} Z_{\text{cold}} m_{\text{cold}}}{(r_{\text{gas}})^2}, \quad (2.2)$$

where  $\tau_{\text{dust},0}$  is a free parameter,  $Z_{\text{cold}}$  is the metallicity of the cold gas,  $m_{\text{cold}}$  is the mass of the cold gas in the disk, and  $r_{\text{gas}}$  is the radius of the cold gas disk. Additionally, stars younger than  $10^7$  yr are enshrouded in a cloud of dust with optical depth  $\tau_{\text{BC},V} = \mu_{\text{BC}} \tau_{V,0}$ , where  $\mu_{\text{BC}} = 3$ . To calculate extinction at other wavelengths, we have assumed a Galactic attenuation curve (Cardelli et al., 1989) for the diffuse dust component and a power-law extinction curve  $A_\lambda \propto (\lambda/5500 \text{ \AA})^n$ , with  $n = 0.7$ , for the birth clouds.

The reemission of IR light by the dust due to blackbody and PAH emission is accomplished in our model using templates which describe the spectra of galaxies from the mid-IR to submillimeter as a function of the total IR luminosity, and are based on observations of galaxies in the local universe. Energy absorbed by dust from direct starlight is redistributed in the infrared according to a prescribed SED. These templates are embedded in our semi-analytic model, and account for emission at wavelengths

from a few microns to the sub-millimeter, including the emission and absorption lines appearing in the PAH region. The idea of templates is based upon the assumption that galaxies of a given IR luminosity can be reasonably represented by a single SED. As we will discuss more in the conclusions, future progress in dust modeling may require moving beyond this approximation.

We have used two different sets of templates in this work. The first are the STARDUST templates of Devriendt et al. (1999); Devriendt & Guiderdoni (2000) and Guiderdoni & Devriendt (1999). These templates are based upon flux ratios observed in IRAS and submillimeter observations, and take the age, star-formation rate timescale, and the size of the gaseous disk as inputs. PAH emission occurs at five wavelengths between 3.3 and 11.3  $\mu\text{m}$ . Thermal emission from larger dust grains is modeled as a two-component blackbody, with one peak at 17 K and another at a higher temperature to simulate the effect of warmer dust near star-forming regions. These templates were used previously in Primack et al. (2001) and Primack et al. (2005); the difference in dust treatment between those models and the current one lies in the inclusion of the Charlot & Fall two component dust prescription.

The second set of templates we have used are presented in Rieke et al. (2009), and are based on observations of 11 local LIRGS and ULIRGS, with observations of lower luminosity systems provided by Dale et al. (2007) and Smith et al. (2007). They make use of the Spitzer MIPS and IRAC instruments, as well as the Infrared Spectrograph (IRS), which is sensitive to most of the PAH region. A single optimized blackbody is used to fit emission in the far-IR. These templates are claimed to reproduce observations

out to  $z = 2$ , where there may be a shift in the strength and line profile of PAH emission. This is claimed to cause not more than a factor of 2 error in luminosity. However, the fact that no bright ULIRGS are observed locally could be another source of error in translating local results to high redshift where these galaxies are common and produce a significant fraction of the IR emissivity.

In the following chapters we will refer to these template sets simply as the ‘Devriendt’ and ‘Rieke’ templates. In Figure 2.1, we show how the templates compare at 4 different IR galaxy luminosities. The newer Rieke templates have less emission in the PAH and mid-IR regions, particularly at the brightest luminosities. As we will see, this will have a significant impact on predictions for attenuation in the spectra of nearby blazars. The Rieke templates are also considerably more detailed in their representation of PAH emission.

### 2.2.3 Non-Stellar Contributions

AGN are also responsible for a minor portion of the infrared background via dust heating in their host galaxies; we do not include this emission in our model. Observations by Chandra and XMM-Newton limit this contribution to  $< 20\%$  at the low part of the EBL spectrum around  $15 \mu\text{m}$ , and conservative assumptions put the contribution in the far-IR peak at  $4\%$ , with a reasonable upper limit of  $10\%$  (Elbaz et al., 2002). The work of Madau & Pozzetti (2000) also put similar constraints on the AGN contribution to the infrared background. As discussed in Hauser & Dwek (2001), a simple analysis of the energy budget available to AGN suggests that the total energy released should be

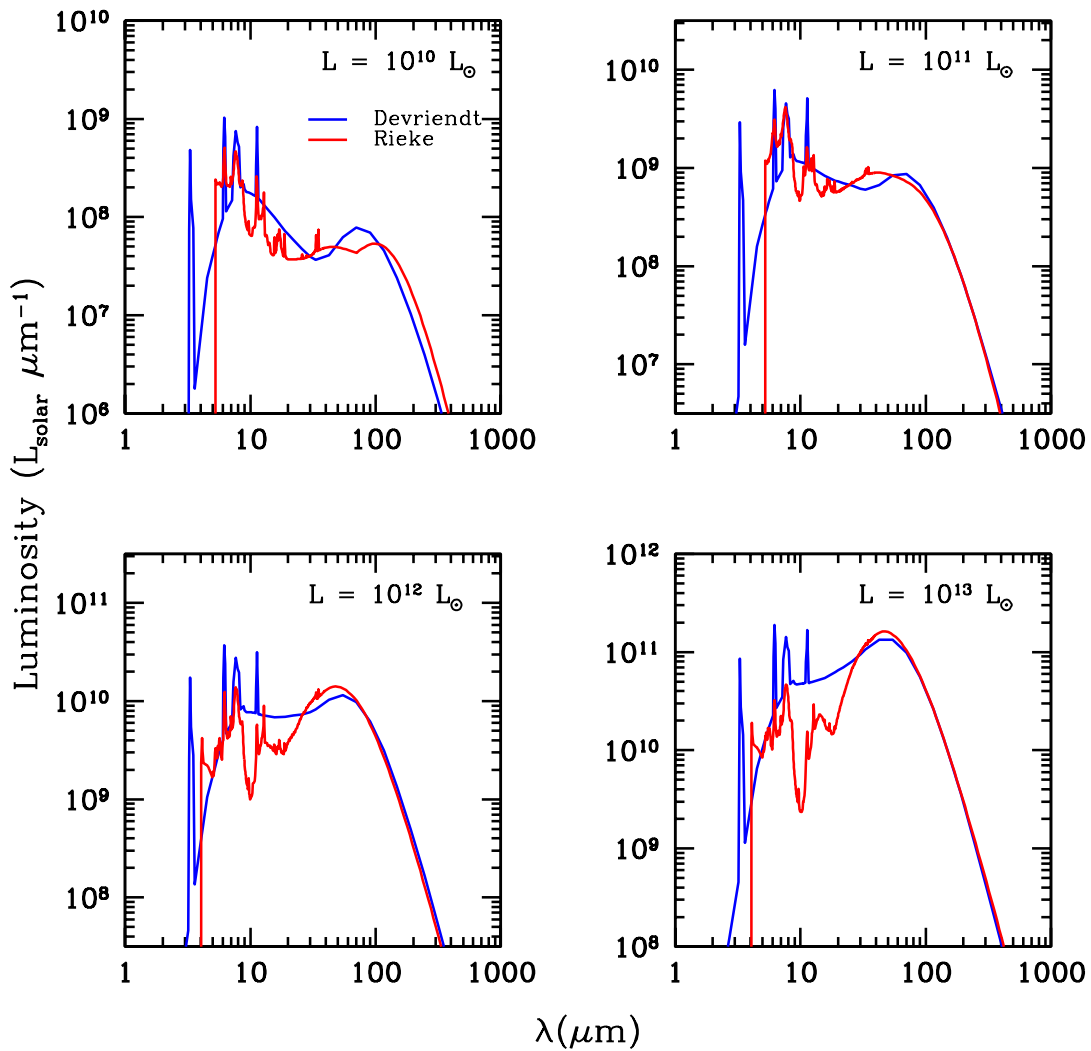


Figure 2.1: Comparison of the dust emission templates of Rieke et al. (2009) (red) and Devriendt & Guiderdoni (2000) (blue). The four panels show templates for bolometric IR luminosities of  $10^{10} L_{\odot}$ ,  $10^{11}$  (a LIRG),  $10^{12}$  (a ULIRG), and  $10^{13}$  (an extremely IR-bright ‘Hyper-LIRG’).

about 10 to 20 % of that from stars. In the UV, quasars are an increasingly important contributor to the total background flux with decreasing wavelength due to their hard spectra relative to young stellar populations. Quasars are a substantial and possibly dominant source of ionizing radiation at the epoch of helium reionization. The role quasars play in forming the UV background, which is relevant to attenuation of lower energy GeV-scale gamma rays, is the subject of Chapter 5. The results in the next two chapters, which are based purely on output from the SAM, do not include a UV quasar component.

There are other mechanisms which could emit at EBL wavelengths which we do not include in this work, but which are worth mentioning in brief. Shock heating of gas during structure formation could be a source of UV radiation emissivity, possibly at a level comparable to that from star-forming galaxies (Miniati et al., 2004). Cooling brown dwarfs could emit in the mid- and far-IR, however the density of these objects would have to be much higher than usually assumed to have a non-negligible contribution to the EBL. Karimabadi & Blitz (1984) found that a  $\Omega_m = 1$  cosmological density of these objects would provide an contribution of  $\sim 3 \text{ nW m}^{-2} \text{ sr}^{-1}$  to the mid- and far-IR. Even if this were not a gross overestimate of the brown dwarf mass density, this amount of flux would still be only a fraction of the total background in our models (Table 3.1). Results from WMAP (Komatsu et al., 2009) constrain all matter to be  $\lesssim 30\%$  of the critical density, and microlensing surveys find that low mass stars and brown dwarfs cannot be more than a small fraction of the dark matter (e.g. Tisserand et al., 2007; Alcock et al., 2000), so the actual background contribution must be negligible. Finally,

radiation in the UV or IR bands could be the product of decaying or annihilating exotic particles. Sciama (1998) proposed long-lived massive neutrinos as a possible contributor to the ionizing UV background. This prediction was subsequently ruled out by experiment (Bowyer et al., 2001). With the right choice of particle properties, density, and decay channels, essentially any spectral profile is possible, and in general there is no compelling reason from astrophysical data to propose a contribution of this type at EBL wavelengths.

# Chapter 3

## EBL Results

### 3.1 Star-Formation History

In this chapter we present results for the EBL and other cosmological observables for the ‘fiducial’ and ‘low’ models described in Section 2.2.1. The main difference between the two models we have presented is that our fiducial model features  $\sigma_8 = 0.9$ , while the low model uses a smaller  $\sigma_8 = 0.761$ . The effect is therefore to delay structure formation in the low model. The global star formation rate density arising in each of our models is shown in Figure 3.1. The difference between the models is most strongly pronounced at early times. Note that we will show another plot of star formation rate density in Chapter 5, Figure 5.5, which emphasizes comparisons with high-redshift data.

As discussed in Fontanot et al. (2009), S08 and other contemporary models do seem to systematically underestimate star-formation rates in low mass galaxies. In larger galaxies, the model makes predictions that are in agreement with the bulk of

data for  $z < 1$ , and tend to be lower than observed at  $z \sim 2$ . All measured star-formation rates are subject to significant uncertainties, as seen in the scatter in results for the plotted data. Uncertainties in dust extinction impact all results relying on UV luminosity. Measurements of  $H\alpha$  and higher order spectral lines must take into account extinction as well as metallicity effects. Other authors have attempted to measure star-formation rates based on  $24 \mu\text{m}$  and other mid-IR observations of warm dust. These results can be affected by AGN contamination, as well as PAH features which move in and out of the instrument bandpass with changing redshift. All of these problems are exacerbated with increasing redshift, where our knowledge of dust distribution and galaxy SEDs becomes less reliable.

In Figure 3.2 we show the integrated stellar mass density. Stars form earlier on the fiducial model due to the higher value of  $\sigma_8$ , and this is seen to be at odds with observations of high redshift galaxies. The contrast between these two plots highlights the well-known observational discrepancy between estimates of the star formation rate and stellar mass (e.g. Hopkins & Beacom (2006); Davé (2008)) discussed in the Section 1.3, in which the integrated value of the former, with allowances for recycling of stellar material under constant initial mass function (IMF), produces stellar mass densities 2-3 times higher than the latter. While the low model seems to be well below best estimates of the star formation rate density at most redshifts—though still within experimental limits—it matches quite well with the stellar-mass density data. One possible explanation, which we have not investigated at this time, is that the IMF was more top-heavy, and therefore produced more high-mass stars, at higher redshift. This would allow for

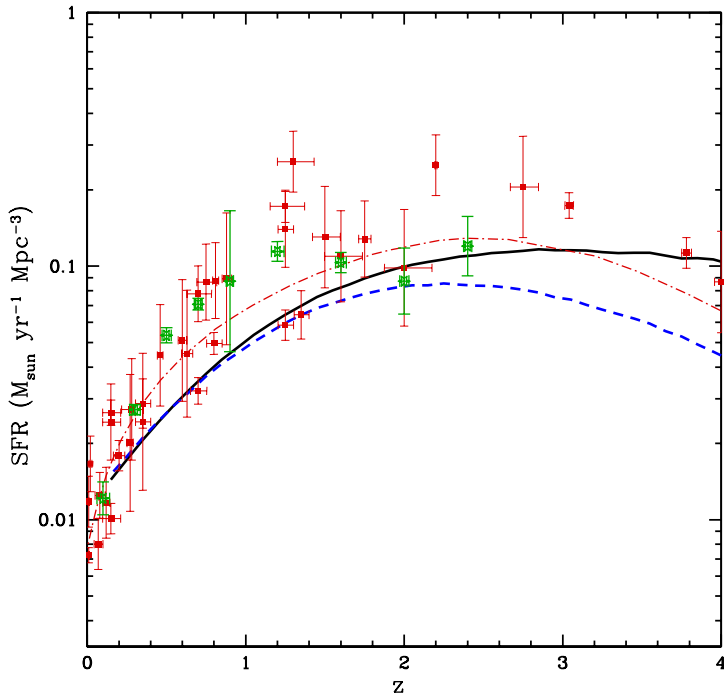


Figure 3.1: The star-formation rate density in each of the two SAMs over cosmic time. The solid black and broken blue curves are the fiducial and low models, respectively. The red points are data from the compilation in Hopkins (2004) with conversion to a Chabrier IMF, and the dot-dashed red line shows the best fit to the data from Hopkins & Beacom (2006). Green points are from  $24\mu\text{m}$  observations by Pérez-González et al. (2005).

higher star-formation at these epochs without locking away as much material in long-lived stars. This scenario was discussed in Fardal et al. (2007), and we address their claims in detail in the discussion in Section 3.4.

One successful prediction of our model is to replicate the shape of the galaxy stellar mass function, which can be cast either in terms of star-formation efficiency, or in terms of the fraction of baryons in stars for a given halo mass. As discussed in S08, this characteristic shape arises from the fact that supernovae winds effectively

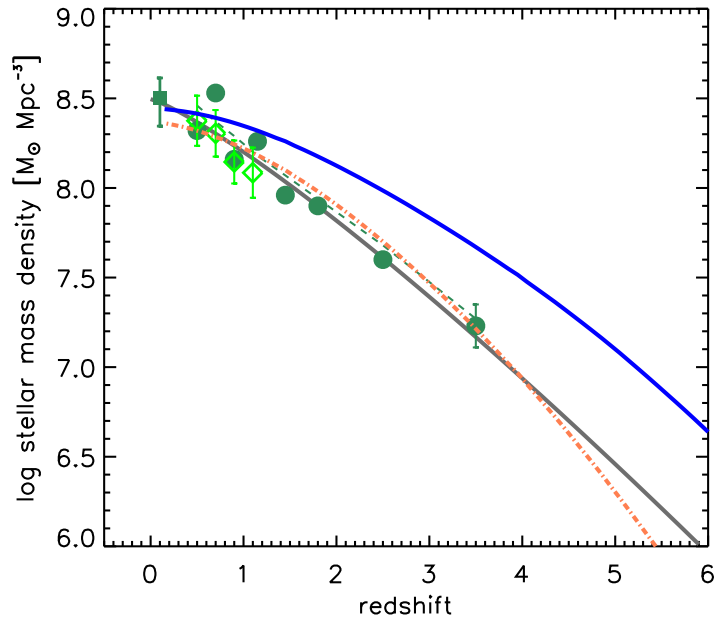


Figure 3.2: The stellar mass density (integrated star formation rate density) for the two models. This plot has been reproduced from Somerville et al. (2008) (S08). The solid blue curve denotes the fiducial model, and broken orange the low model. The solid square is the  $z=0$  estimate of Bell et al. (2003), the circles are from Fontana et al. (2006), and the open diamonds are from the COMBO-17 estimates of Borch et al. (2006). The gray line is the best fit to the observational compilation of Wilkins et al. (2008).

heat and expel gas in smaller halos, while radio mode heating quenches star-formation in large halos. Without this quenching mechanism, stars are overproduced in massive systems, leading to an overabundance of bright blue galaxies. The function peaks at a halo mass of  $\sim 10^{12} M_{\odot}$ , where the halo mass is too large for supernovae to drive gas from galaxies, but the relatively low black hole sizes and halo virial temperature limit the efficiency of AGN heating. The results of AGN heating can be compared to a much simpler model in which all star formation is quenched at a halo mass of  $10^{12} M_{\odot}$ . This simple ‘halo quenching’ model produces good agreement with data for the local stellar mass function, cold gas fraction, and global star formation history. However, the star-formation efficiency function is too sharply-peaked, and this model fails to match the observation that massive galaxies ( $> 10^{11} M_{\odot}$ ) have significant star-formation rates. The fiducial model does overestimate the high-mass end of the galaxy mass function, though there is evidence that mass inferred from luminosity may be underestimated in some of the major surveys (see von der Linden et al., 2007). Dividing the mass function into different galaxy morphologies (bulge- versus disk-dominated), it is found that this excess is primarily in bright spirals, with a corresponding deficit of low-mass disks. The cold gas fraction is in reasonable agreement with data, but also shows a small excess for high-mass galaxies. The stellar mass versus metallicity relation shows agreement with the estimates from SDSS of Gallazzi et al. (2005), though there are a number of potential observational biases which complicate this comparison.

## 3.2 Number Counts and Luminosity Functions

In this section, we focus on more direct observables such as number counts and luminosity functions. Difference in dust re-emission modeling has a substantial impact on the EBL at wavelengths longer than  $\sim 8\mu\text{m}$ . We present results here using the Devriendt templates described in Section 2.2.2 for both models, and also show results for the fiducial model using the recently published Rieke templates based on Spitzer data. The latter should be considered preliminary at this time. Due to time constraints on this project, we have not yet been able to do a detailed comparison of these templates, nor have we integrated Rieke templates into the low model.

Comparisons with number count data provide a basic test of the model's reproduction of galaxies in the nearby universe, as well as a direct link with the local EBL, which should be reproducible by summing over all magnitudes in a given band. Large scale surveys such as the Sloan Digital Sky Survey (SDSS), the 6-degree Field survey (6dF) and the 2-Micron All Sky Survey (2MASS) have provided us with an accurate accounting of the galaxies in the local universe, and surveys with the HST have complemented this data with extremely deep counts. Our K-band counts are in reasonable agreement with the data, but tend to be high compared with many of the points, suggesting that there is little tolerance for increased low redshift star formation which would increase brightness in these wavelengths. In the IR, the Spitzer IRAC and MIPS cameras, as well as ISO, provide counts in a number of bands from 3.6 to 160  $\mu\text{m}$ . IRAC has 4 wavelength bands from 3.6 to 8  $\mu\text{m}$ , with good survey statistics

down to magnitude  $\sim 19.5$ , where source confusion and incompleteness become serious problems (Fazio et al., 2004). MIPS is particularly well-suited to study the emission of (U)LIRGs in the non-local universe with its 24  $\mu\text{m}$  band, although the 70 and 160  $\mu\text{m}$  bands have poorer angular resolution and become confusion-limited at deep magnitudes (Dole et al., 2004). In Figures 3.3, 3.4, and 3.5 we show number counts from our model with available data at a variety of wavelengths. At optical wavelengths, we find good agreement with bright counts, where SDSS-DR6 (Montero-Dorta & Prada, 2008) has found slightly higher counts than older SDSS data presented in the compilation by Dolch (2009). In the IR, we show the predictions from the fiducial model using newer Rieke et al. dust templates, in addition to the Devriendt templates used previously. The difference between the two is most evident in the 24 $\mu\text{m}$  band, where the older Devriendt templates are seen to overpredict bright counts.

The local luminosity density has been extremely well-measured in the optical and near-IR by large-scale surveys such as SDSS and 2MASS. In Figure 3.7 we show how our models fit the local data at all wavelengths, including GALEX, SDSS, 6dF, 2MASS, IRAS and SCUBA. We closely fit the optical and UV measurements. In Figure 3.6, we show the predictions of our fiducial model compared to local luminosity functions, as determined by the SDSS observations of nearby galaxies. We find good agreement across most of the optical, within a reasonable amount of scatter. Our model does seem to be slightly high at fainter magnitudes in the faint end of the SDSS  $g$ -,  $r$ -, and  $i$ -bands, but based on our number counts it does not appear that these are resulting in any systematic overestimate of the total emissivity.

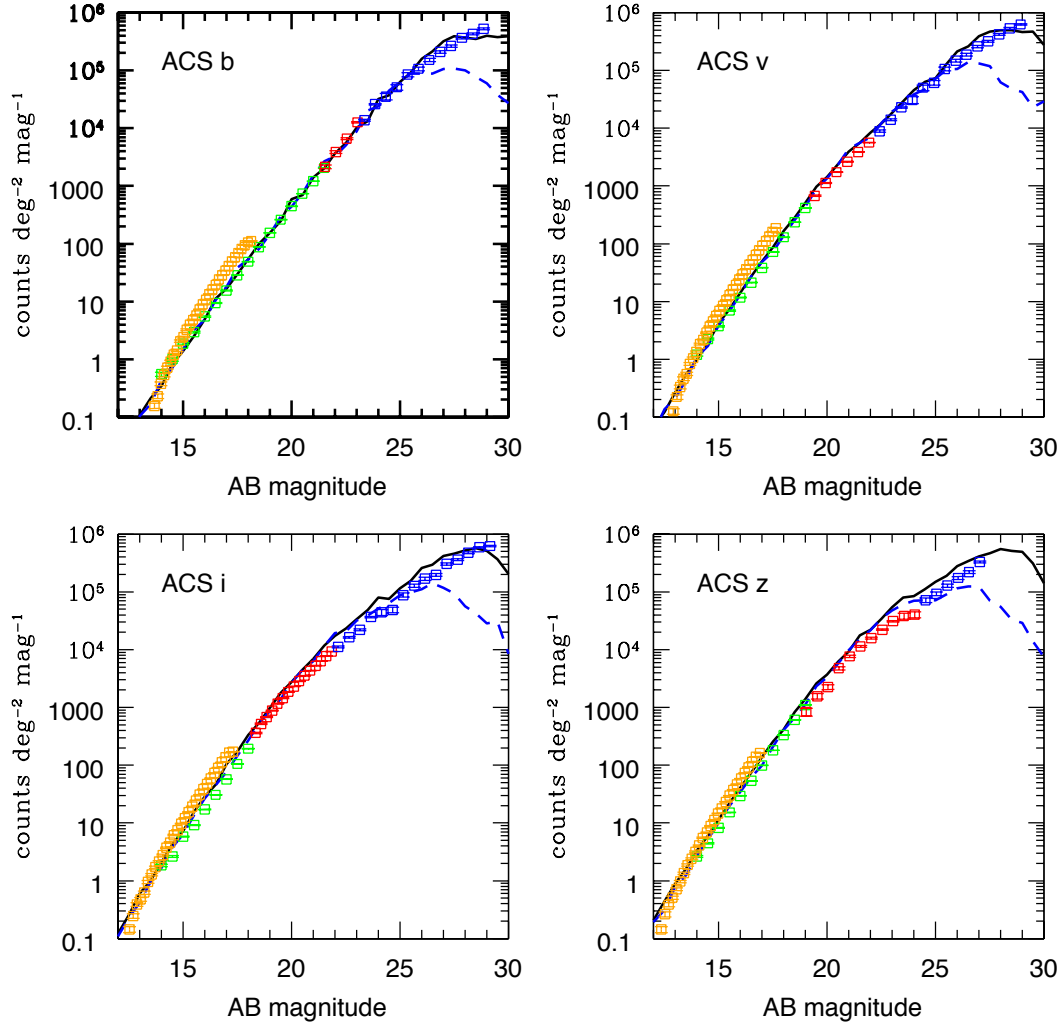


Figure 3.3: Number counts in the four HST ACS bands. The solid black line represents the fiducial model, and the dashed blue line is the low model. Red, blue and green data is from the compilation by Dolch (2009), which includes data from the Hubble Ultra-Deep Field. Additional data in orange from SDSS-DR6 is provided by Montero-Dorta & Prada (2008).

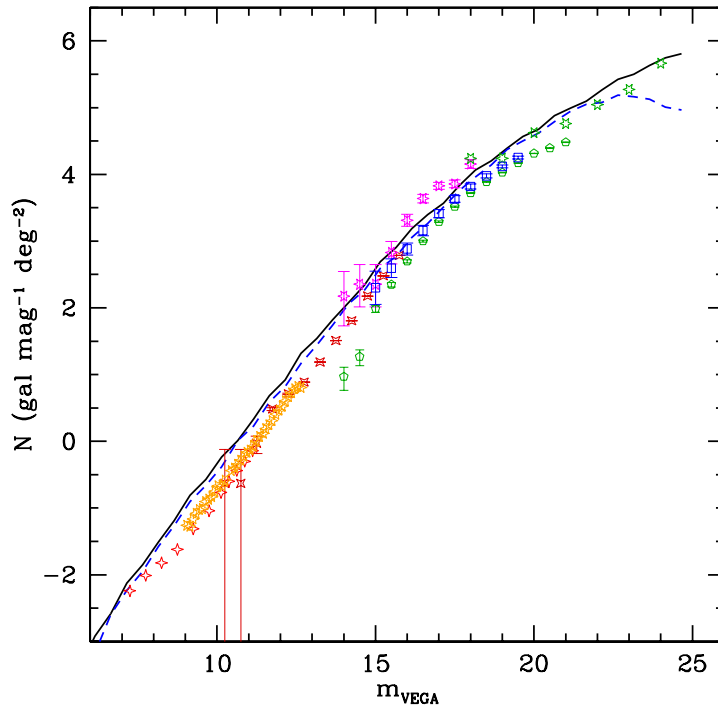


Figure 3.4: Galaxy counts in the K-band ( $\sim 2.2 \mu\text{m}$ ). Lines colors and types are as in the previous figure. Data is from the 6dF survey (Jones et al., 2006) (orange stars), 2MASS (Kochanek et al., 2001) (red stars), and DEEP2/Palomar (Conselice et al., 2008) (green pentagons). Red stars at bright magnitudes are from Gardner et al. (1996), magenta stars are from Martini (2001), and blue squares are from Barro et al. (2009).

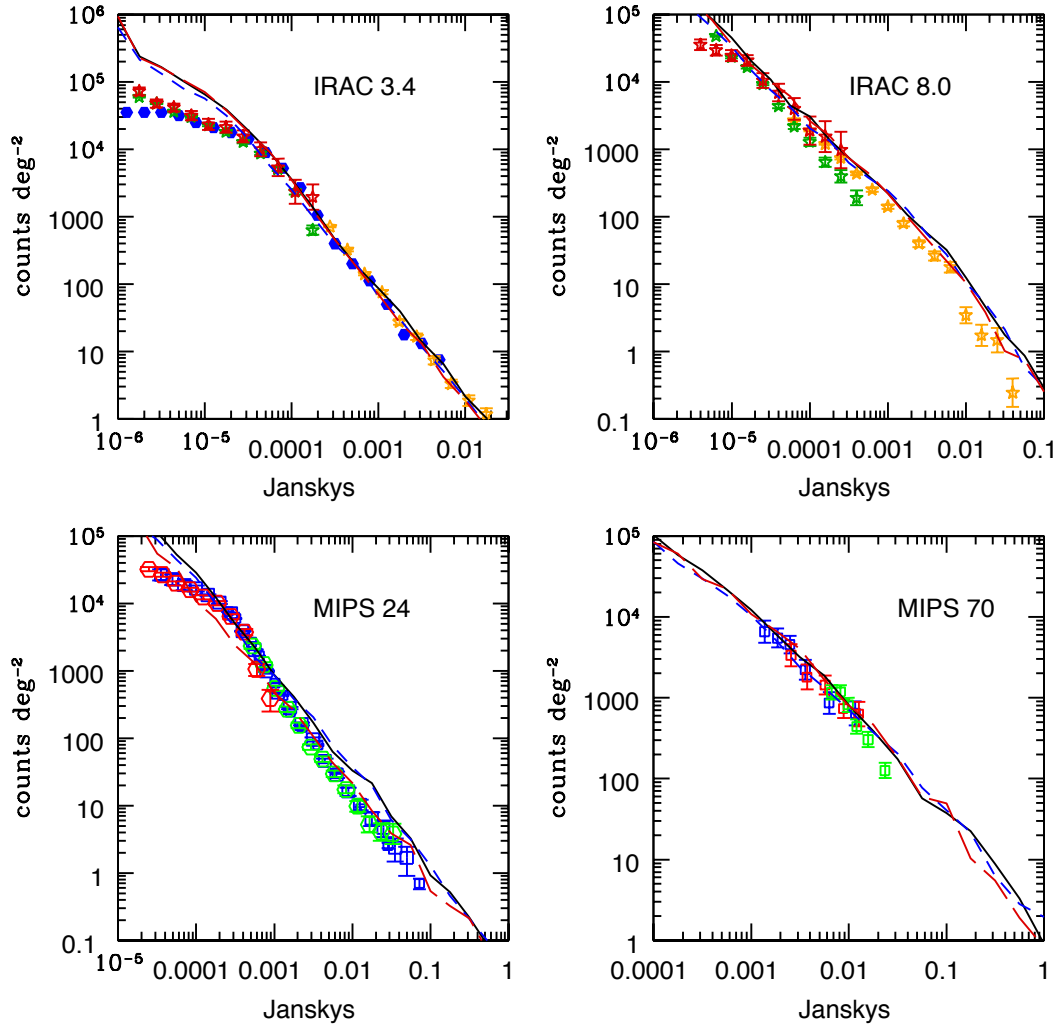


Figure 3.5: Number counts from four Spitzer (IRAC and MIPS) infrared bands; as in previous figures the solid black line represents the fiducial model, and the dashed blue line the low model using Devriendt dust templates (see Section 2.2.2). The long dashed red line shows the fiducial model using the new Rieke dust emission templates. Data in the IRAC bands is from Fazio et al. (2004); Sanders et al. (2007); the MIPS data is from Papovich et al. (2004); Shupe et al. (2008); Chary et al. (2004) at  $24\mu\text{m}$  and (Frayser et al., 2006) at  $70\mu\text{m}$ .

We have also compared our model with evolving luminosity density, which is the integrated light from luminosity functions at a number of different redshift bands (Figure 3.8). The peak emissivity in our model varies based on the wavelength considered. At UV bands, the emission closely follows star-formation rate, which peaks at  $z \approx 2.25$  in our low model and  $z \approx 3$  in the fiducial. Longer wavelengths include significant contributions from progressively more evolved stellar populations, and therefore peak at later times. Recent evolutionary surveys such as DEEP2 and COMBO-17 allow us to compare the evolution of galaxy emissivity against accurate luminosity density data in several bands. Emissivity at  $2800 \text{ \AA}$  has been seen to increase out to nearly  $z = 2$  (Dahlen et al., 2007). In the B-band wavelengths, Dahlen et al. (2005) find emission increases out to at least  $z = 1$ ; this paper makes the claim that emissivity in the B- and R-bands is consistent with being flat in the interval  $1 < z < 2$  (though this does not seem to be reflected in their reported R-band results). Results at the higher redshifts could be sensitive to the faint end slope assumed in calculating the luminosity density.

### 3.3 The Buildup of the EBL

The present-day EBL obtained in each of our models is shown in Figure 3.9. We also show results from Primack et al. (2005), which was a previous calculation with this SAM and Devriendt dust templates, as well as Franceschini et al. (2008), a recent model based on evolving luminosity functions of different galaxy populations. The

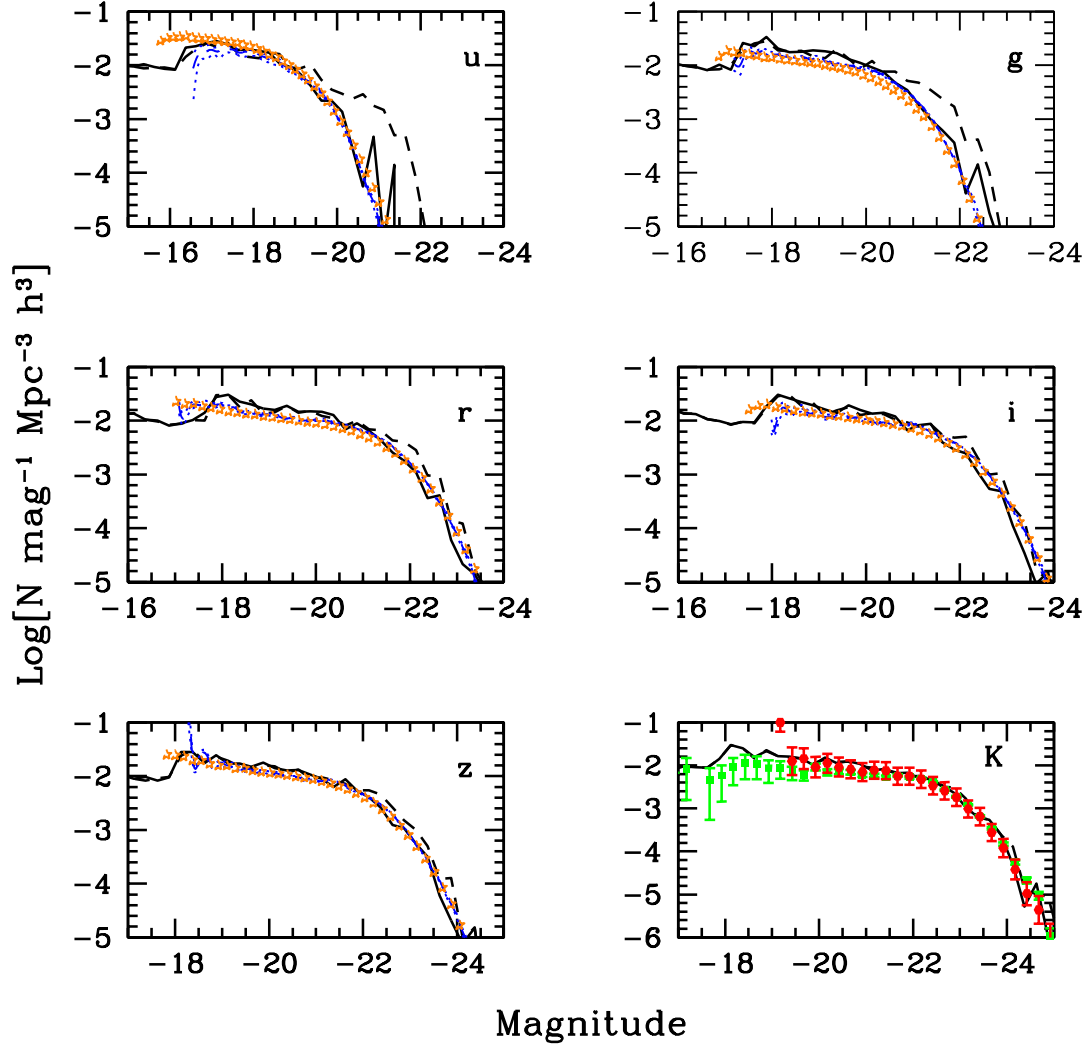


Figure 3.6: The rest-frame luminosity functions for the fiducial model in a variety of bands. Solid and dashed curves show the model with and without dust processing. In the SDSS bands, orange data is from SDSS-DR6 (Montero-Dorta & Prada, 2008), while blue points are from the older SDSS-DR2 (Blanton et al., 2003). For the K-band plot, the green points are from 2dF (Cole et al., 2001) while the red are from 2MASS (Kochanek et al., 2001).

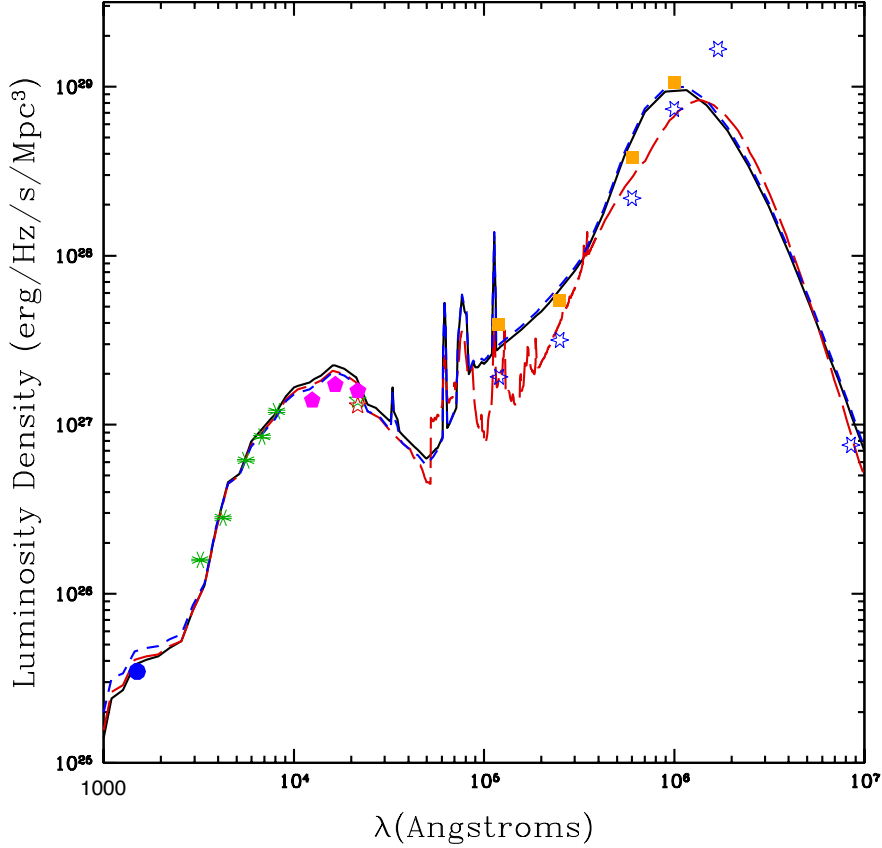


Figure 3.7: The  $z=0$  luminosity density of our model. As before, the fiducial model is shown as a solid black line, the low model as dashed blue, and the fiducial model with Rieke dust templates is dashed red. Data at a number of wavelengths is shown from GALEX (blue circle), SDSS (green stars; Montero-Dorta & Prada, 2008), 6dF (magenta pentagons; Jones et al., 2006), 2MASS (green star; Cole et al., 2001, and red star; Bell et al., 2003). In the mid- and far-IR, the orange squares are from IRAS (Soifer & Neugebauer, 1991), while blue stars are from an analysis of local emissivity using data from IRAS, ISO, and SCUBA (Takeuchi et al., 2001).

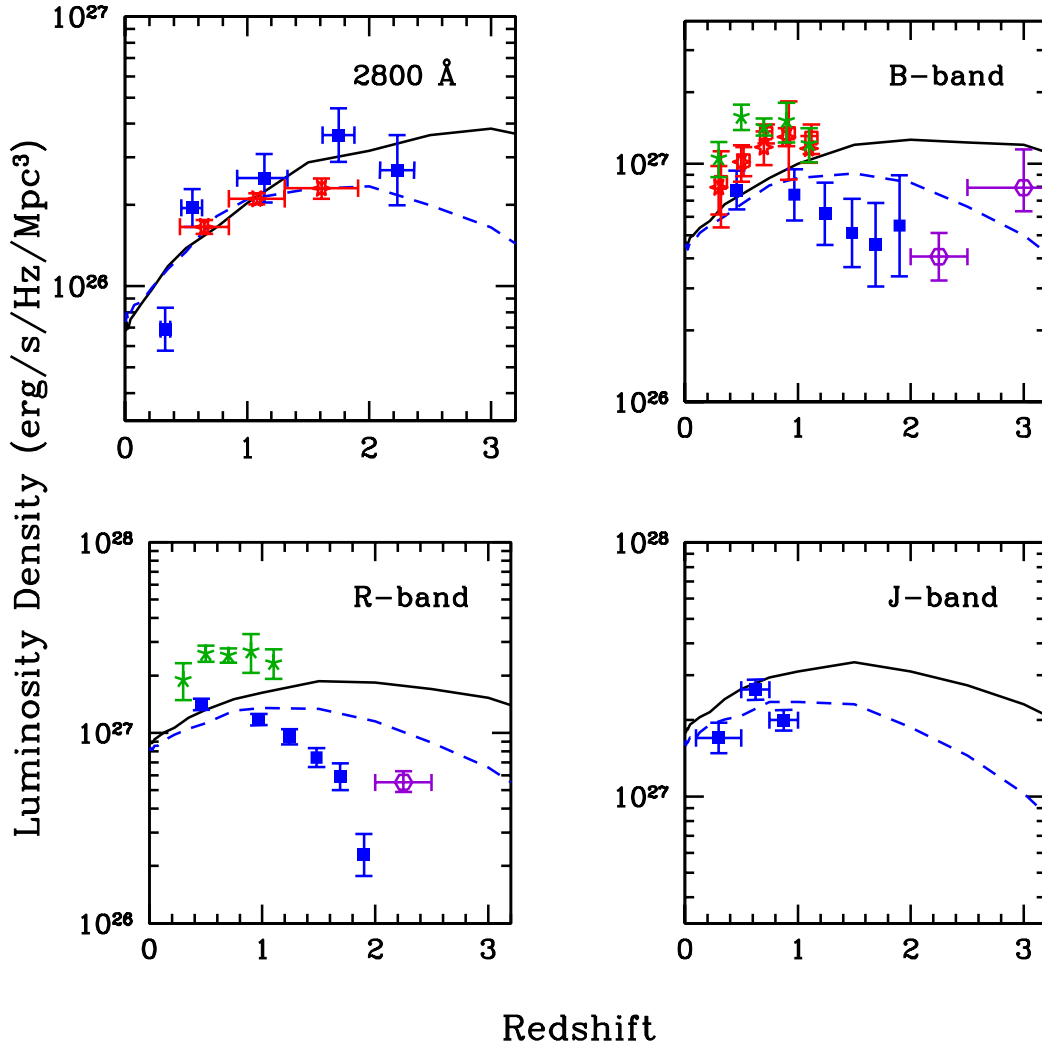


Figure 3.8: The luminosity density (integrated luminosity function of sources within a given redshift range) in our models vs. redshift at  $2800 \text{ \AA}$  and in the B-, R-, and J-bands (approximately  $4500 \text{ \AA}$ ,  $6500 \text{ \AA}$ , and  $1.25 \mu\text{m}$ , respectively). The fiducial model is shown in black, the low model as dashed blue. Data for the  $2800 \text{ \AA}$  plot is from Dahlen et al. (2007) (blue squares) and Gabasch et al. (2006) (red stars). In the B-, R-, and J-bands data from the COMBO-17 and DEEP surveys is included from Faber et al. (2007) (red stars and squares), Dahlen et al. (2005) (blue squares), and Wolf et al. (2003) (green stars). Purple hexes are from Marchesini et al. (2007).

local EBL is calculated by integrating over the luminosity density at all wavelengths beginning at  $z = 7$ , and accounting for the redshifting and dilution of photons as the universe expands. The EBL at a redshift  $z_0$  and frequency  $\nu_0$  in proper coordinates can be written as (Peebles, 1993)

$$J(\nu_0, z_0) = \frac{1}{4\pi} \int_{z_0}^{\infty} \frac{dl}{dz} \frac{(1+z_0)^3}{(1+z)^3} \epsilon(\nu, z) dz, \quad (3.1)$$

where  $\epsilon(\nu, z)$  is the galaxy emissivity at redshift  $z$  and frequency  $\nu = \nu_0(1+z)/(1+z_0)$ , and  $dl/dz$  is the cosmological line element, defined as

$$\frac{dl}{dz} = \frac{c}{(1+z)H_0} \frac{1}{\sqrt{\Omega_m(1+z)^3 + \Omega_\Lambda}} \quad (3.2)$$

for a flat  $\Lambda$ CDM universe. We assume here that the EBL photons evolve passively after leaving their source galaxies and are not affected by any further interactions except for cosmological redshift. This is an acceptable approximation for photons at energies below the Rydberg energy of 13.61 eV. At higher energies, photons are capable of interacting with residual neutral hydrogen and, if sufficiently energetic, neutral and singly-ionized helium in the intergalactic medium. Also, photons above this energy are strongly attenuated by neutral hydrogen when leaving their galaxy of origin. The effect of these processes on the ionizing EBL is the topic of Chapter 5; for now we will discuss the background only at non-ionizing wavelengths.

Figure 3.9 includes recent constraints on the EBL from number counts in surveys and direct determination based on foreground subtraction. The total flux of the integrated EBL for each model is shown in Table 3.1. The total flux contributions in the optical–near-IR and far-IR peaks, as well as the mid-IR valley, are also shown.

Wavelength Range	Fiducial Model	Low Model	Fiducial Model (Rieke)
Optical–near-IR peak (0.1 to 8 $\mu\text{m}$ )	24.56	20.23	24.40
Mid-IR (8 to 50 $\mu\text{m}$ )	7.37	6.24	5.49
Far-IR peak (50 to 500 $\mu\text{m}$ )	26.07	21.19	23.58
Total (0.1 to 500 $\mu\text{m}$ )	58.00	47.66	53.47

Table 3.1: The integrated flux of the present-day EBL in our three models (fiducial and low with Devriendt dust templates, and fiducial with Rieke templates), over 3 different wavelength ranges. Units are  $nW/m^2/sr$ .

Results are presented here in terms of  $\lambda F_\lambda = \lambda dF/d\lambda$ , which gives the EBL power per logarithmic interval in wavelength  $\lambda$ . Note that  $\nu F_\nu$  is a dimensionally equivalent formulation that is often used. Some authors also quote results in units of energy density, such as  $\text{eV cm}^{-3}$ , rather than flux. A useful conversion is (Hauser & Dwek, 2001)

$$E^2 n_E (\text{eV cm}^{-3}) = 2.62 \times 10^{-4} \lambda F_\lambda (\text{nW m}^{-2} \text{sr}^{-1}),$$

where  $E$  is the energy in eV and  $n_E$  is the photon number density in  $\text{eV}^{-1} \text{cm}^{-3}$ .

A correct determination of gamma-ray opacity at distances beyond the immediate universe,  $z > 0.05$ , requires accounting for the redshift-dependent evolution of the background at all wavelengths. The sharply increasing star formation from  $z=0$  out to  $z \sim 2$ , combined with the  $(z+1)^4$  flux dependence on redshift means that the background was considerably more powerful in the recent past, a fact that can only be neglected in attenuation calculations for the closest extragalactic sources. With observations of VHE extragalactic sources now stretching out to redshifts of over 0.5, it is important that in comparing different realizations of the EBL that we focus not only on the flux at  $z = 0$ , but at higher redshifts as well, where behavior may be quite different depending on the model of star formation used. We show how the background develops

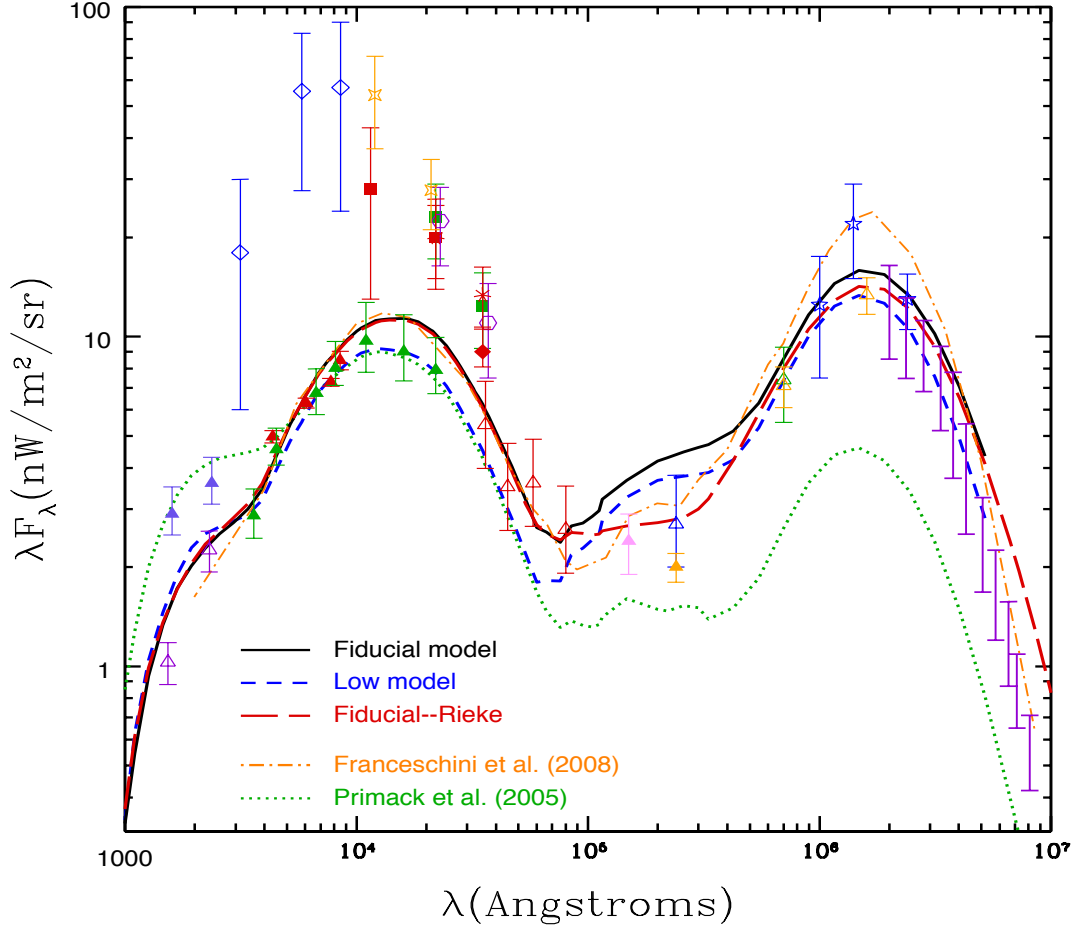


Figure 3.9: The predicted  $z = 0$  EBL spectrum from our fiducial (black) and low (dashed blue) models using the Devriendt dust templates, and the fiducial model with Rieke templates (red long-dashed), compared with experiments at a number of wavelengths. Our previous model (Primack et al., 2005), and the model of Franceschini et al. (2008) are also shown for comparison (dotted green curve and dash-dotted orange curve). Upward pointing arrows indicate lower bounds from number counts; other symbols are results from direct detection experiments. **Lower limits:** The blue-violet triangles are results from Hubble and STIS (Gardner et al., 2000), while the magenta open triangles are from GALEX (Xu et al., 2005). The green and red triangles from Hubble Deep Field (Madau & Pozzetti, 2000) and Ultra Deep Field (Dolch, 2009) respectively, combined with ground based-data. Open red triangles are from IRAC on Spitzer (Fazio et al., 2004), and the pink point at  $15 \mu\text{m}$  is ISOCAM (Elbaz et al., 2002) on ISO. The remaining lower limits are from MIPS at 24, 70, and  $160 \mu\text{m}$  on Spitzer (Papovich et al., 2004; Chary et al., 2004; Frayer et al., 2006; Dole et al., 2006). **Direct Detection:** The open blue diamonds are from Bernstein (Bernstein, 2007). The points at  $1.25$ ,  $2.2$ , and  $3.5 \mu\text{m}$  are based upon DIRBE data with foreground subtraction (Wright, 2001) (dark red squares), (Cambrésy et al., 2001) (orange 4-stars), (Levenson & Wright, 2008) (red diamond), (Gorjian et al., 2000) (purple open hexes), (Wright & Reese, 2000) (green square), and (Levenson et al., 2007) (red asterisks). In the far-IR, direct detection data is shown from DIRBE (Wright, 2004) (blue stars), and (Hauser et al., 1998) (green stars), and also purple bars showing the detection of FIRAS (Fixsen et al., 1998).

in our models in two ways in Figure 3.10. The top panels show the proper EBL SED from different redshifts in the rest frame, for each of our models. The bottom panels show the EBL at those same redshifts evolved to present day; this is the background that would be seen today if all galaxy emissivity had been shut off below the indicated redshift. It can be seen in the top plots that the EBL photon density was considerably higher in the past at all wavelengths. The most striking rises from present day levels are in the mid- and far-IR, and in the UV.

Complementary to Figure 3.10, in Figure 3.11 we show how the photons populating the EBL at various wavelengths today have been produced as a function of redshift. As expected from our knowledge of obscured starbursting galaxies at high redshift, the mid- and far-IR parts of the EBL came into existence considerably sooner than the photons that are part of the optical–near-IR peak today. These results are in reasonable agreement with a recent survey of submillimeter galaxies (Devlin et al., 2009) which has found that half of the background radiation at  $250 \mu\text{m}$  is produced at  $z > 1.2$ , with this fraction increasing at longer wavelengths. We also confirm the findings from the SCUBA observations of MIPS-detected sources that find almost all the submillimeter flux arising from  $z > 1.3$  (Dye et al., 2006). The results for the fiducial and low models are qualitatively similar, however due to earlier star formation in the fiducial model a greater percentage of photons are in place at a given redshift for all wavebands, relative to the low model. At UV wavelengths ( $\lesssim 4000\text{\AA}$ ), the background increasingly reflects recent emission due to the sharp spectral falloff in this regime, and therefore follows the recent star-formation rate due to these photons being produced

almost exclusively by short-lived stars.

The rapid increase in flux at all wavelengths with increasing redshift means that the attenuation per unit distance increases a corresponding amount. Therefore, gamma rays from more distant blazars suffer more attenuation than might be expected from the local EBL flux. In addition, the functional form of the EBL changes, so a simple  $z$ -dependent scaling factor is not sufficient to allow accurate predictions of spectral modification for the more distant sources.

### 3.4 Discussion

At nearly all wavelengths we have considered, our two proposed EBL SEDs are near the level of flux resolved in discrete background counts. In the UV, we find an EBL lower than calculated using a combination of HDF and balloon-based FOCA data (Gardner et al., 2000). The later GALEX experiment, while not capable of surveying to the depth of Hubble, found a smaller number of bright counts than the FOCA data, likely resulting from differences in calibration of the instruments (Xu et al., 2005). It is therefore possible that the higher Gardner points resulted from overestimating the bright counts in their determination.

Our models lie below the level of direct detection of the absolute background by calculations using data from Hubble WFPC2, DIRBE, and IRTS (see Introduction and Figure 3.9). The low significance and large error bars on the HST points of Bernstein (2007) mean that these results should not be considered inconsistent with an EBL at

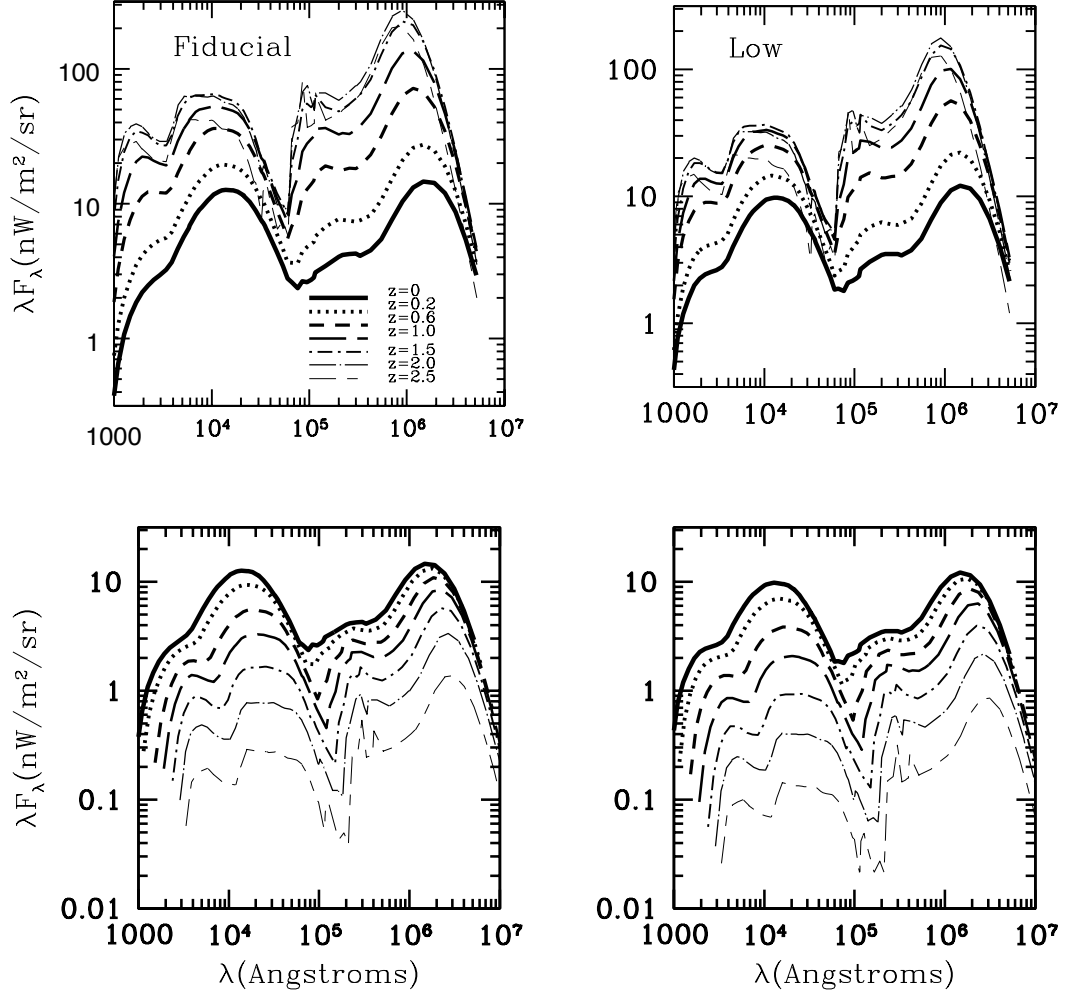


Figure 3.10: The history of the EBL in each of our models. The top 2 plots show the background flux at past redshifts in the fiducial (left) and low (right) models in standard units. Redshifts shown include  $z = 0$  (solid),  $z = 0.2$  (dotted),  $z = 0.6$  (short dashed),  $z = 1$  (long dashed),  $z = 1.5$  (dot-short dashed),  $z = 2$  (dot-long dashed) and  $z = 2.5$  (long and short dashed); also see the key in the upper-left panel. The bottom two plots show the same quantities, but now evolved to present-day, allowing easy comparison of the EBL in place at a particular time compared to the total at  $z = 0$ .

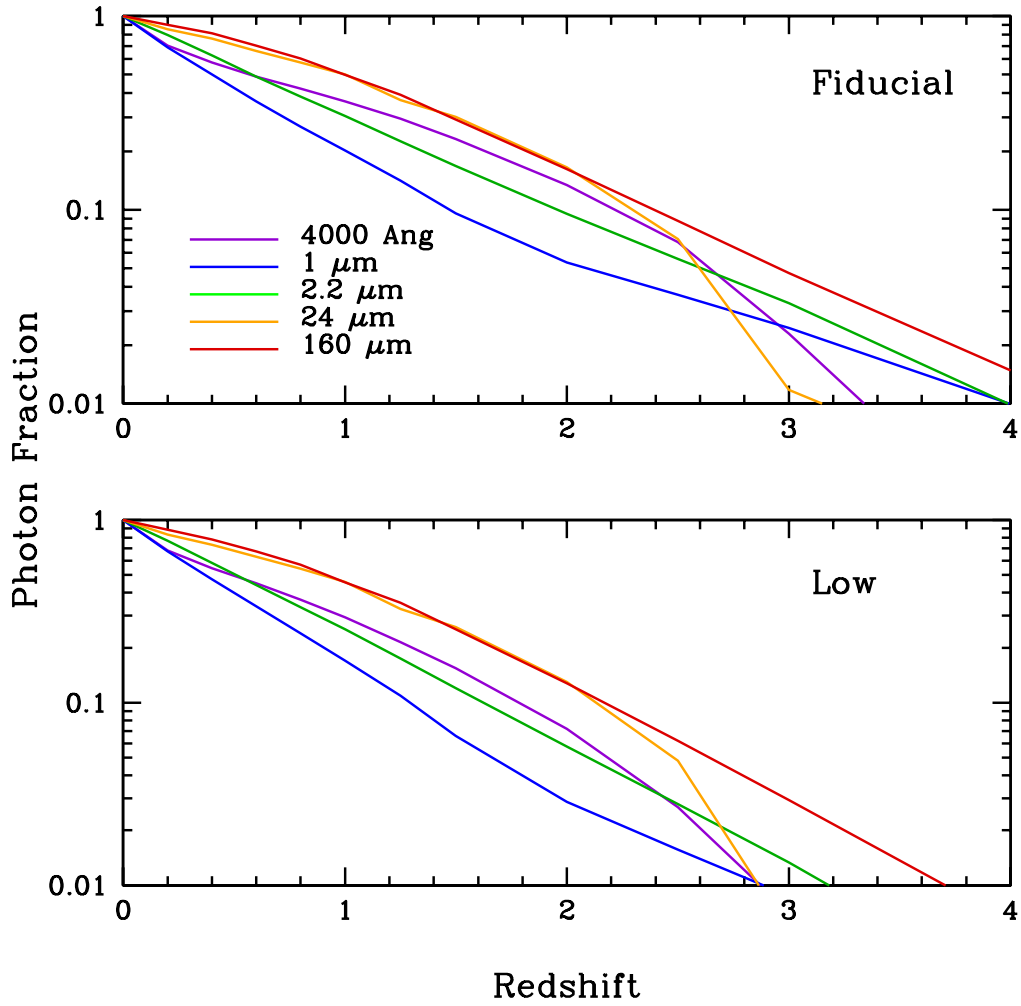


Figure 3.11: The buildup of the photon population at various wavelengths shown separately for our fiducial and low models, showing the fraction of photons at a given present-day wavelength in place at past redshifts. The wavelengths are indicated as follows: violet = 400  $nm$ , blue = 1  $\mu m$ , green = 2.2  $\mu m$ , orange = 24  $\mu m$ , and red = 160  $\mu m$ .

the level provided by resolved sources. Our fiducial model is at least  $1\sigma$  below the flux from any of the near-IR direct detection calculations we have discussed; considerably more for the results based on the Kelsall et al. (1998) zodiacal light model. Limits from gamma-ray observations have strongly disfavored the highest levels at this range. As discussed in Levenson et al. (2007), the present uncertainty in zodiacal light subtraction, exemplified in the difference between the Kelsall and Wright (1998) models (of  $3.4 \text{ nW m}^{-2} \text{ sr}^{-1}$  at  $3.6 \mu\text{m}$ ), may be intractable without a new mission to directly study this foreground.

Fardal et al. (2007) compared the possible range of EBL flux measurements with observations of the fossil mass and star formation rate history of the universe. As our semi-analytic model reproduces these 3 observables, it is worth discussing our work in the context of this claim that a top-heavy or ‘paunchy’ IMF can best fit simultaneously these parameters. This proposal is based on the argument that the low levels of estimated stellar mass are difficult to reconcile with the present-day EBL flux suggested by the majority of data and integrated star-formation rate; an issue we discussed in the Introduction. Fardal et al. (2007) create 3 models of the EBL based on all available observational limits. Their minimal model, with total flux of  $50 \text{ nW/m}^2/\text{sr}$ , is set by resolved number counts and is intermediate to our low and fiducial models in the optical and near-IR out to the K-band. Their best-fit model, based on a compromise between number counts compilations and the HST and DIRBE direct detection measurements, is substantially higher than our fiducial model. The K-band number counts are well measured by a number of surveys (see Figure 3.4) which constrain the amount of stellar

mass in the nearby universe. Two factors alleviate the discrepancy in our model. Our background fluxes are near the lowest levels considered in Fardal et al. (2007), with total fluxes of 58.0 and 47.66 nW/m<sup>2</sup>/sr for our fiducial and low model respectively, and our global Chabrier IMF produces more high-mass stars than the diet-Salpeter considered as the standard by these authors. For a near-IR flux much higher than our fiducial model to not overproduce the K-band counts, this flux would have to arise from a high-redshift population of sources unresolvable in our current surveys, which extend to > mag 24. As mentioned in the Introduction, there are reasons why the star-formation rate measures we compare against at high-redshift may tend to be biased high. This interpretation favors our low EBL model, which has slightly less flux than Fardal’s lowest model, and is in fairly good agreement with integrated star-formation and observed K-counts (Figures 3.2 and 3.4, respectively).

Referring back to Figure 3.9, we recognize two places in our calculated EBL SED in which there is tension with observations that do not rely strongly on foreground estimates, and which may signal shortcomings in our spectral modeling. Our low model falls roughly  $2\sigma$  under the 5.6  $\mu\text{m}$  lower bound from Spitzer, and  $1\sigma$  below the 8  $\mu\text{m}$  bound. The fact that the 5.6  $\mu\text{m}$  limit is higher than that at 4.5 may cast some suspicion on this particular measurement, as there is no reason to believe such a spectral feature would exist. Nonetheless, the low model is only marginally in agreement with these data, and the fiducial model leaves little room for contribution from unresolved sources. These counts are based upon early ‘first-look’ data, and newer results based on a larger set of survey data may soon be available (Fazio, G. , private communication). Additional

sensitivity and survey width may be achievable in the 3.6 and 4.5  $\mu\text{m}$  bands by post-cryogenic ‘Warm Spitzer’ surveys; however the higher wavelength bands will not be capable of operating at elevated temperatures (van Dokkum et al., 2007). While our models are consistent within  $1\sigma$  with number count measurements by MIPS in the mid- and far-IR, they are low compared to the DIRBE measurements of the far-IR peak. The zodiacal foreground is a sharply decreasing function of wavelength in this regime, and the DIRBE points are expected to suffer from less systematic error here than in the near-IR, especially at 240  $\mu\text{m}$ , where our low model lies beneath the data. The inability of our models to reproduce the SCUBA counts at 850  $\mu\text{m}$  (Figure 3.12) is the most glaring failure of this analysis, with more than a factor of 10 error seen. The total EBL flux from our model at the far-IR DIRBE wavelengths certainly does not differ from data by anywhere near this ratio, therefore the problem must lie in the inability of our templates to produce sufficient bright galaxies at these wavelengths. Our models are in good agreement with the claim in Dole et al. (2006) that their stacking analysis of 24  $\mu\text{m}$  sources has detected most ( $> 75\%$ ) of the background at 70 and 160  $\mu\text{m}$ . In the next chapter, we will see that for the purposes of gamma-ray attenuation, the wavelengths above  $\sim 30 \mu\text{m}$  are of little interest due to the high optical depth of nearby extragalactic sources (by any reasonable background model) at corresponding gamma energies. Therefore, while we acknowledge that dust reemission in our model is unable to produce bright submillimeter sources and may underestimate the far-IR flux by a small factor, we do not consider these problems to be detrimental to our calculation of gamma-ray opacities.

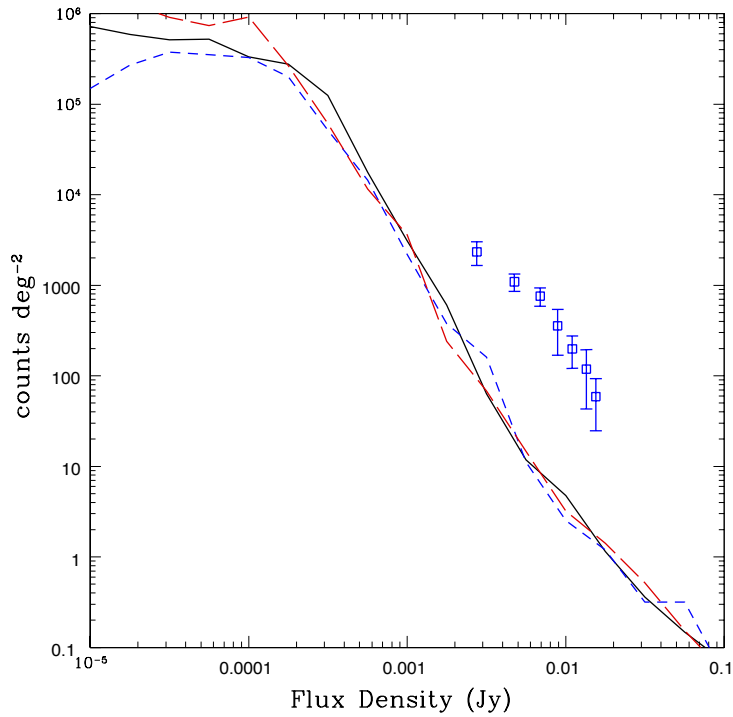


Figure 3.12: The counts at 850 microns, compared to predictions from our model; see discussion in the text. Solid black, dashed blue, and long-dashed red lines denote results from the fiducial and low model with Devriendt templates, and the fiducial model with Rieke templates, respectively. Data is from the SCUBA SHADES survey (Coppin et al., 2006).

# Chapter 4

## Gamma-ray Attenuation by the EBL

### 4.1 Historical Overview

Since the earliest days of gamma-ray astronomy, it has been recognized that interactions between gamma rays and background target photons could create electron-positron pairs. By effectively removing these gamma rays from view, this process has the potential to alter the observed spectra of high-energy sources, and completely occlude those at sufficient distance. The idea that gamma rays could be absorbed in this manner was first pointed out by Nikishov (1962). This paper explored the effect of a thermal near-IR background component on TeV gamma rays, and even calculated the opacities for ‘star’ Cygnus A (a radio galaxy at  $z = 0.056$ ).

A few years later, interest shifted to attenuation by the then newly-discovered CMB. Gould & Schreder (1967) and Jelley (1966) showed that the high density of photons at millimeter wavelengths would make the universe opaque to gamma rays above

100 TeV. Fazio & Stecker (1970) included redshift dependence and different cosmologies in predicting the opacities for a high-redshift source of gamma rays, and also mentioned attenuation of GeV gamma rays by the background of optical photons.

While the theory relating gamma-ray observations to the levels of background flux was established by these papers in the 1960s and 70s, observing attenuation in gamma-ray spectra would not be possible until pioneering gamma-ray experiments revealed more about the nature of extragalactic sources. The COS-B satellite, operating from 1975 to 1982 and observing an energy range of 50 MeV to 5 GeV, made the first definite association of gamma-rays with an extragalactic object, 3C273 (Swanenburg et al., 1978).

The EGRET experiment on Compton Gamma-ray Observatory (CGRO), launched in 1991, created an all-sky gamma-ray map which included more than 65 AGN above 100 MeV (Hartman et al., 1999). While the energy range of this experiment, roughly 20 MeV–30 GeV, was too low for any detection of attenuation due to background effects, its observations set an important benchmark for future experiments and identified these sources for targeted observation. EGRET also detected emission from a small number of gamma-ray bursts (GRBs), which established that these events can emit photons well into the GeV energy range— an idea we will pursue in Chapter 6.

The development of ground-based techniques such as imaging atmospheric Cherenkov telescopes (IACTs) were key to understanding the highest energy TeV-scale gamma-rays, which were at energies of 10–1000 times higher than the upper end of the EGRET energy range. This technique uses the opacity of the atmosphere to all

gamma-rays and involves searching for the Cherenkov light produced by the shower of secondary particles that are created when gamma rays scatter in the upper atmosphere (Weekes & Turver, 1977). The first major experiment in this field was the Whipple telescope, which detected TeV gamma-rays associated with the blazar Markarian 421, at  $z = 0.031$  (Punch et al., 1992). This represented the first observation that could reasonably put constraints on the EBL.

Continued observations of known EGRET sources and radio-loud AGN by Whipple led to the discovery of the BL Lac object Mrk 501, at redshift  $z=0.034$  (Quinn et al., 1996a). This object had not been reported by EGRET, and was thus the first blazar to be initially detected at gamma-ray energies from the ground. By 1999, 5 AGN sources had been detected and/or confirmed by Whipple and other various first-generation IACT experiments operating contemporarily, such as HEGRA, CAT, the Durham Mark 6 telescope, the Telescope Array Project, TACTIC, and the Crimean Astrophysical Observatory (Catanese & Weekes, 1999).

Another technique which was developed at this time was the water-Cherenkov detector. The Milagro experiment, and its predecessor Milagrito, used a pool of water at ground level as a medium for Cherenkov radiation, rather than the atmosphere as in the IACT technique. Photomultiplier tubes in the pool detected the Cherenkov light produced when the particle shower created by the gamma ray reached the ground and passed through the water.

While Milagro was less sensitive to gamma-ray flux than contemporary IACTs, it did have the advantage of a much larger field of view and a  $>90\%$  duty cycle, compared

to 10% for IACTs. This made it better-suited for searching for transient events such as GRBs and flaring AGN. The only blazar which Milagro was able to confidently detect was Mrk 421 (Williams & MILAGRO Collaboration, 2005). Searches for high energy emission from GRBs have only been able to produce upper limits on flux (Saz Parkinson & Dingus, 2008). This may have been due in a large part to the universe being optically thick to gamma rays at redshifts of most GRBs for Milagro energies.

Today exploration in the VHE regime is led by >10m-class IACTs including the VERITAS (Maier, 2007), H.E.S.S. (Hinton, 2004), and MAGIC (Cortina, 2005) experiments. VERITAS and H.E.S.S. both currently consist of arrays of four  $\sim 12$  m telescopes. VERITAS is located in Arizona and observes the northern sky, while H.E.S.S. is on the high-altitude veldt of central Namibia in southern Africa, and views the southern sky, including the Galactic center. MAGIC, located on La Palma in the Canary Islands, consisted of a single 17-meter telescope until recently, when a second nearly identical dish was added; this upgraded ‘MAGIC-II’ experiment reported first light in April 2009. Until recently, a wide gap existed between the energy range available to these instruments and the highest energies yet probed by space based detectors such as EGRET on the CGRO. The Fermi experiment, as well as AGILE (Tavani et al., 2008), are providing much needed data in the energy decade of 10 to 100 GeV, where the sensitivity of ground based IACTs declines rapidly. The Fermi satellite, formerly known as GLAST, launched in June 2008. Fermi contains two instruments, both operating at gamma-ray energies. The Large Area Telescope (LAT) is a pair conversion telescope that views gamma rays from 20 MeV up to  $\sim 300$  GeV with an effective area of nearly

1 m<sup>2</sup> (Atwood et al., 2009). The Gamma-ray Burst Monitor (GBM) consists of 12 NaI scintillation detectors and two BGO detectors, and is designed to provide alerts to transient events such as gamma-ray bursts. While in survey mode, the wide angle view of the LAT enables it to see the entire sky every 3 hours, and Fermi can therefore report flaring blazars to other detectors for study.

Ground-based detectors searching above 100 GeV have identified 26 extragalactic sources at the time of writing, including 23 BL Lac objects, radio galaxies M87 and Centaurus A, and the flat-spectrum radio quasar (FSRQ) 3C279. With the exception of the radio galaxies these objects are all blazars, accreting AGN which generate tightly beamed relativistic jets, that lie at a small angle relative to our line of sight. The most distant gamma-ray detection claimed thus far from the ground is 3C279 at  $z = 0.536$ , and most other sources have been found at  $z < 0.25$ . In contrast, EGRET sources detected above 100 MeV were seen out to  $z = 2.28$ . There is a strong bimodality seen between the populations of BL Lac objects and FSRQs in this sample, with the latter being more numerous, more luminous, and having a redshift distribution peaking at  $z \sim 1$ . BL Lacs are found mostly at low redshift, and have luminosities typically 1 to 2 orders of magnitude less than FSRQs (Dermer, 2007). Therefore, the detection of FSRQ 3C279 by MAGIC hints at the possibility that many more distant AGN sources may be visible from the ground.

## 4.2 Gamma-ray Attenuation

The process of photon-photon scattering to electron-positron pairs is well understood from quantum electrodynamics. The basic kinematic requirement for this process is that there must be sufficient energy in the center-of-mass frame of the two photon system to create the pair. Including the effect of interaction angle as measured in the cosmological frame, this can be written

$$\sqrt{2E_1E_2(1 - \cos \theta)} \geq 2m_e c^2, \quad (4.1)$$

where  $E_1$  and  $E_2$  are the photon energies and  $\theta$  is the angle of incidence. We are interested here in cases where the target background photon has energies from the submillimeter ( $\gtrsim 10^{-3}$  eV) to the far UV ( $\lesssim 100$  eV). The corresponding gamma-ray energies are therefore in the GeV or TeV range. Thus the pair creation is a very unbalanced process energetically, and the pair is created with a highly relativistic velocity and most of the energy of the gamma ray must go into producing that momentum. We can rewrite Equation 4.1 to define the minimum threshold energy  $E_{th}$  for a background photon to interact with a gamma ray of energy  $E_\gamma$ ,

$$E_{th} = \frac{2m_e^2 c^4}{E_\gamma(1 - \cos \theta)}. \quad (4.2)$$

The cross-section for this process is (Gould & Schreder, 1967; Madau & Phinney, 1996)

$$\sigma(E_1, E_2, \theta) = \frac{3\sigma_T}{16} (1 - \beta^2) \left[ 2\beta(\beta^2 - 2) + (3 - \beta^4) \ln \left( \frac{1 + \beta}{1 - \beta} \right) \right], \quad (4.3)$$

where

$$\beta = \sqrt{1 - \frac{2m_e^2 c^4}{E_1 E_2 (1 - \cos \theta)}}, \quad (4.4)$$

and  $\sigma_T$  is the Thompson scattering cross section.

The cross section is maximized for center-of-mass energies of approximately twice the threshold energy  $2m_e c^2$ , and falls approximately as inverse energy for  $E \gg E_{th}$ . If we also account for  $\theta$ , we find that the likelihood of absorption is maximized for photons at about 4 times the absolute threshold energy, with one factor of 2 from  $\sigma$  and another in going from  $\theta = \pi$  ('head-on' configuration) to the most probable angle of interaction  $\theta \approx \pi/2$ . If we assume  $\theta = \pi/2$ , then we can define the characteristic energy or wavelength for the background photons which will most strongly affect a gamma ray of energy  $E_\gamma$  as

$$E_{bg} = \frac{4m_e^2 c^4}{E_\gamma} = 1.044 \left( \frac{\text{TeV}}{E_\gamma} \right) \text{ eV}, \quad (4.5)$$

or equivalently,

$$\lambda_{bg} = 1.188 \left( \frac{E_\gamma}{\text{TeV}} \right) \mu\text{m}. \quad (4.6)$$

This relation is only approximate, and the actual wavelength of photons most likely to interact with the gamma ray is dependent on the background spectral energy distribution. For instance, if the number density of target photons increases rapidly with wavelength, then most of the attenuation for a gamma ray of given energy will be due to scattering with photons near  $E_{th}$ . In Figure 4.1 we show Equation 4.3 in graphical form, showing the wavelengths of background photons which are at the threshold energy and those for which cross section is maximized. The central solid line corresponds to Equation 4.6. Figure 4.2 shows how the cross section varies in  $E_\gamma$  for a particular choice of  $E_{bg}$  and  $\theta$ . The function reaches a peak at  $2E_{th}$  of approximately  $0.26\sigma_T$ .

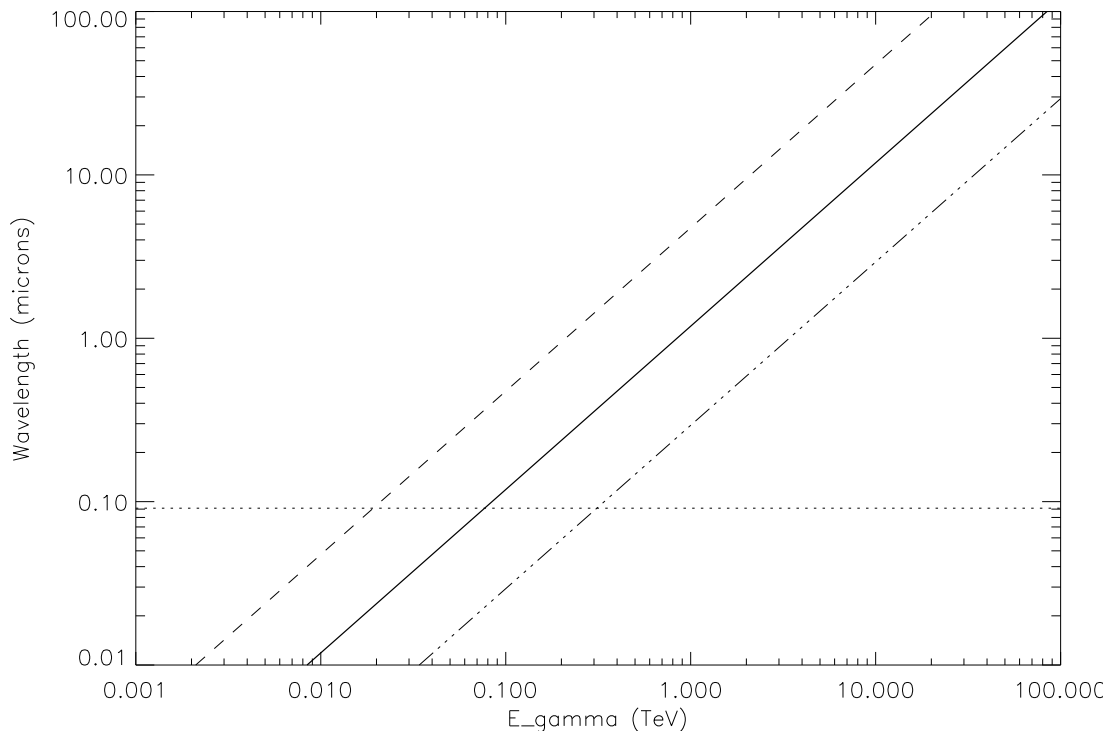


Figure 4.1: This plot shows the kinematics for EBL interactions in graphical form. The upper dashed line is the maximum wavelength of EBL photon with which a gamma ray of energy  $E_{\text{gamma}}$  can interact, assuming an optimal ‘head-on’  $\theta = \pi$  configuration. The solid line is the wavelength for which the cross-section is maximized, assuming an angle of incidence  $\theta = \pi/2$ , where statistically the most interactions will occur. The dash-triple-dotted line shows where the cross section falls to half of its maximal value, again assuming  $\theta = \pi/2$ . The horizontal dotted line shows where the background energies are 13.6 eV (1 Rydberg). As we shall see later when we discuss the UV background, the density of background photons falls rapidly at wavelengths shortward of this point due to absorption of hydrogen-ionizing photons by stellar atmospheres, H I in galaxies, and processing by the intergalactic medium (IGM).

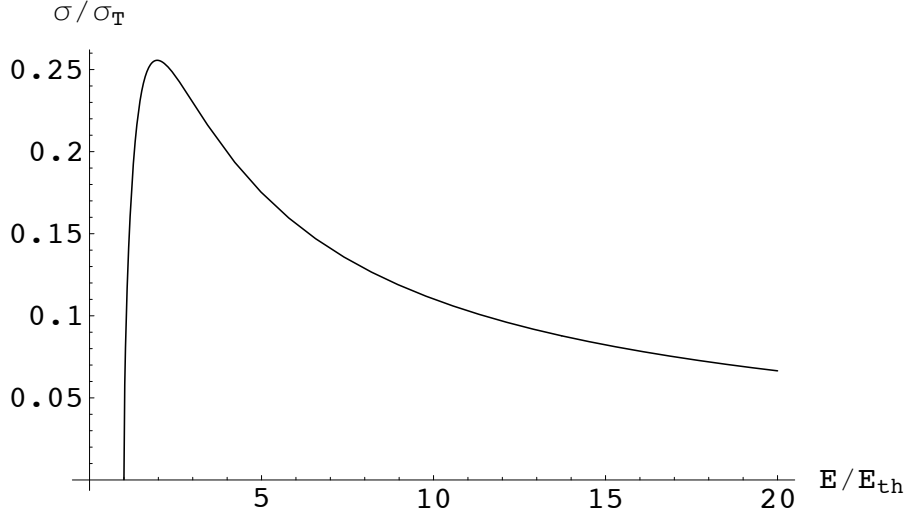


Figure 4.2: The functional form of  $\sigma(E_1, E_2, \theta)$ , as a function of  $E_\gamma/E_{th}$ .

Gamma rays above 1 TeV are most attenuated by the near- and mid-IR range of the EBL, while those in the 200 GeV to 1 TeV regime are sensitive to light in the near-IR and optical. Below 200 GeV it is mainly UV photons that have sufficient energy to cause the pair-production interaction. Below 19 GeV only background photons with energies above the Lyman limit of  $912 \text{ \AA}$  have sufficient energy to interact at any angle in the rest frame, and there is little attenuation. Note that these numbers refer to instantaneous energy of the gamma ray at a given point along its path from source to observer, which can be substantially higher than its observed energy due to the cosmological redshift if the source is distant enough. Gamma rays from distant sources can therefore be affected by background photons of longer wavelength than their observed energy would suggest.

To calculate the optical depth for a gamma ray observed at energy  $E_\gamma$ , we

perform the integral along the line of sight to the target at redshift  $z$ ,

$$\tau(E_\gamma, z_0) = \frac{1}{2} \int_0^{z_0} dz \frac{dl}{dz} \int_{-1}^1 du (1-u) \int_{E_{min}}^\infty dE_{bg} n(E_{bg}, z) \sigma(E_\gamma(1+z), E_{bg}, \theta). \quad (4.7)$$

Where we have

$$E_{min} = E_{th} (1+z)^{-1} = \frac{2m_e^2 c^4}{E_\gamma(1+z)(1-\cos\theta)}$$

to account for the redshifting of the gamma-ray energy. Here  $n(E_{bg}, z)$  is the proper density of target background photons as a function of energy  $E_{bg}$  and redshift  $z$ , and  $u$  is shorthand for  $\cos\theta$ .  $dl/dz$  is the cosmological line element, defined in Equation 3.2. For very nearby sources,  $z \lesssim 0.05$ , it is sufficient to use the local EBL density  $n(E_{bg}, z=0)$ . However, as we saw in Section 3.3, both the total power and SED of the EBL vary strongly with redshift, and in general it is therefore necessary to understand the evolution of the background to correctly compute opacities.

### 4.3 Gamma-ray Opacity Results

In this section, we show the key result of the first part of this thesis, which is the gamma-ray optical depth resulting from our EBL models. We have used the line-of-sight integral (Equation 4.7) discussed above to create plots of optical depth as a function of gamma energy for a variety of redshifts (Figure 4.3), including  $z = 0.54$ , the redshift of the most distant source yet detected at very high energies using ground-based techniques. A more general way to show EBL attenuation is to plot the ‘attenuation edge’ redshift where the optical depth reaches a certain value as a function of gamma energy (Figure 4.4). The redshifts and approximate highest detected energies of several

AGN sources are shown on this plot as well. This shows how telescopes with lower energy thresholds will allow us to peer deeper into the universe.

## 4.4 EBL Constraints from Gamma-rays

Observations of the modification to gamma-ray spectra from extragalactic sources provide a measurement of the EBL that is independent of direct observation. In principle, the cosmological history of the EBL could be reconstructed by comparing observations of high-energy sources at different redshifts to their known intrinsic spectra. Unfortunately, the emission mechanisms of GeV and TeV sources are in general poorly understood. Experiments at a wide variety of energy ranges have revealed that the spectra of blazars consist of a two-peaked distribution, the lower peak between the infrared and x-rays, the upper in the gamma-rays. This pattern is commonly understood as the result of a relativistic jet of charged particles. Whether this jet consists primarily of leptons or hadrons remains controversial (Sikora & Madejski, 2001). The leptonic model is preferred for its simplicity and ability to explain correlations in x-ray and gamma-ray flares as both being fueled by the same population of electrons. Hadronic models involving proton acceleration are an alternative source of gamma rays which are sometimes considered, but lack a clear-cut explanation of correlations within different wavebands. A single-zone leptonic model allows the key model parameters to be derived from measurements of the spectrum and normalization (Aharonian, 2001). The lower-energy peak is attributed to synchrotron emission, while the high energy

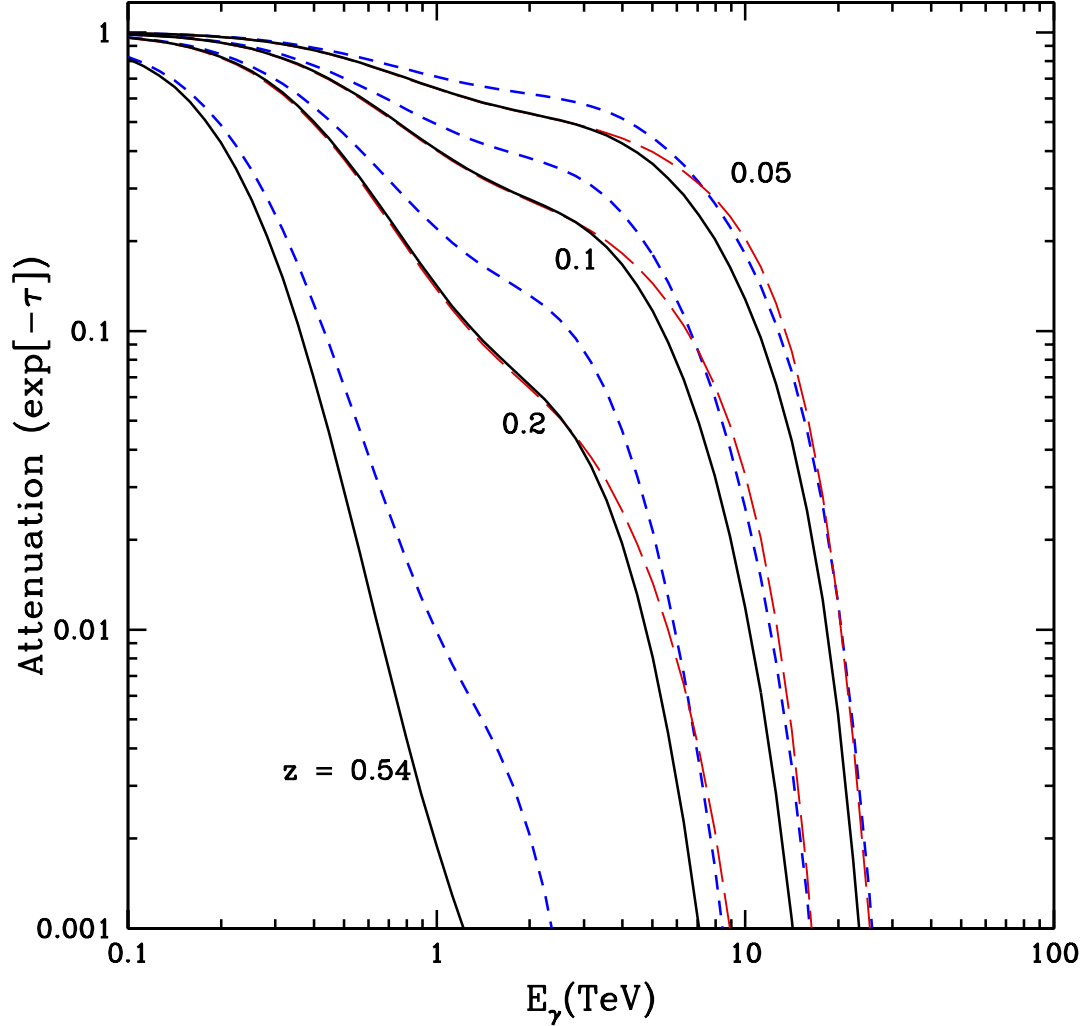


Figure 4.3: The attenuation  $e^{-\tau}$  of gamma-rays vs. gamma-ray energy, for sources at  $z = 0.05, 0.1, 0.2,$  and  $0.536$  (the redshift of 3C279). Following the convention of our previous plots, the fiducial model is solid black, the low model is dashed blue, and the fiducial model using new Rieke dust templates is shown in long-dashed red. Note that the dust modeling only affects observations above about 3 TeV. Increasing distance causes absorption features to increase in magnitude and appear at lower energies. The plateau seen between 1 and 10 TeV at low redshift is a product of the mid-IR valley in the EBL spectrum.

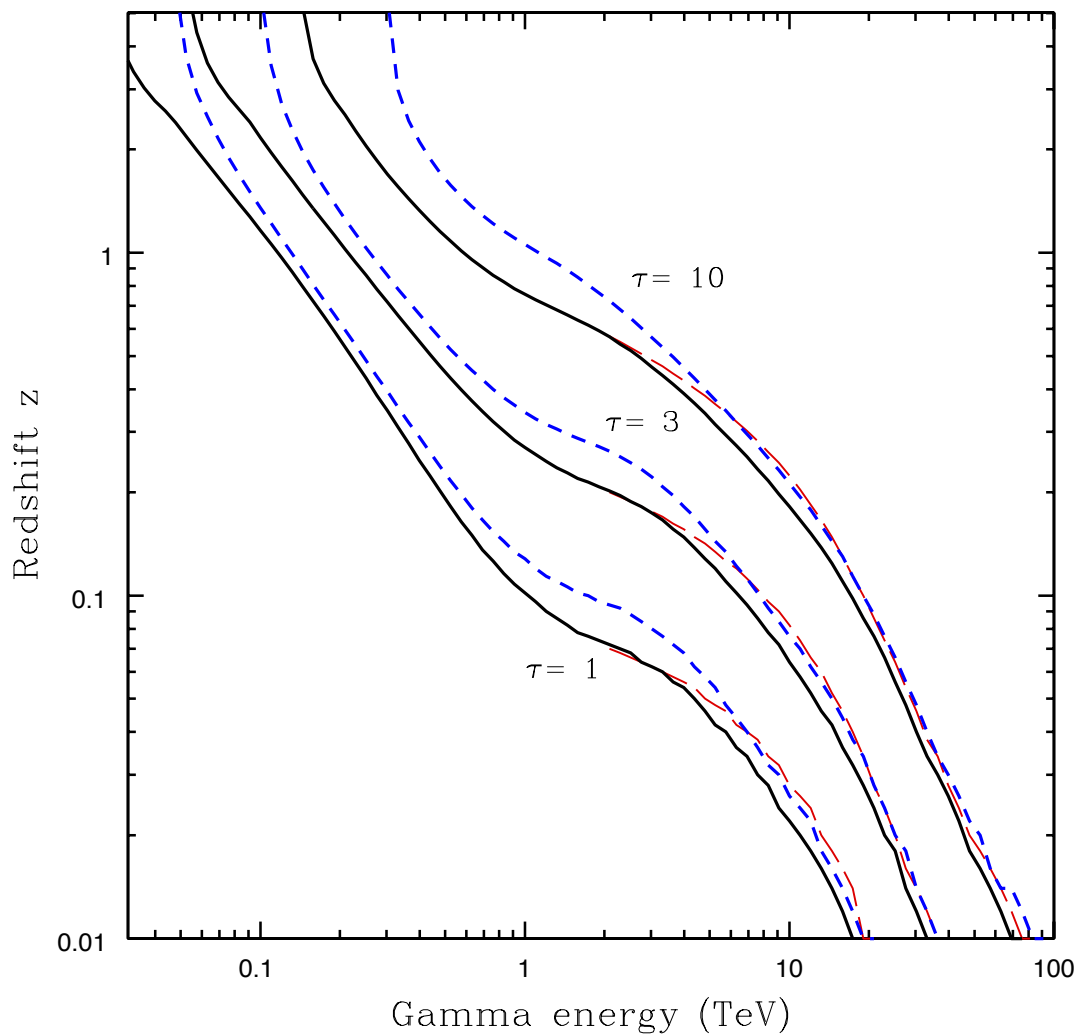


Figure 4.4: The gamma-ray attenuation edges for our 3 EBL models; colors and line types are as in the previous plot. The curves show the redshift at which the pair-production optical depth  $\tau$  reaches the indicated value for a particular observed gamma ray energy. The sets of curves from lower left to upper right are the contours for  $\tau = 1$ , 3, and 10.

peak is the result of inverse Compton radiation seeded by either the synchrotron photons themselves (the synchrotron self-Compton or SSC model) or photons from other sources (the external Compton or EC model). It has been argued in the case of at least 2 rapidly varying blazars that such variability is better modeled with an external radiation source (Begelman et al., 2008). There is evidence that there exists a BL Lac sequence, with less luminous objects having both peaks at higher energies than more brilliant sources (Fossati et al., 1998; Ghisellini et al., 1998; Maraschi et al., 2008). The high frequency-peaked BL Lac objects (HBLs) which have been the most common source type detected above 100 GeV, are therefore understood as being at the extreme end of a continuum that includes intermediate- and low-frequency peaked blazars, which are more luminous overall. The sequence may arise as a result of increased cooling of the accelerated particles at higher luminosities, suggesting that sources with brighter bolometric luminosities would have lower Lorentz factors and peak energies (Ghisellini et al., 1998, 2002). While they account for almost all the detected sources above 100 GeV, BL Lac objects are themselves only a small subset ( $\sim 20\%$ ) of all blazar sources, the other 80 percent being FSRQs like 3C279.

While uncertainties and likely variation in the intrinsic spectra of blazars make it impossible to directly link the observed spectrum to EBL attenuation, it is possible to translate limits on the spectra to EBL constraints. The standard assumption in placing limits on the EBL from individual spectra is that the reconstructed intrinsic spectrum should not have a spectral index harder than 1.5; that is,  $\Gamma \geq 1.5$  if  $dN/dE \propto E^{-\Gamma}$  for photon count  $N$ , or alternatively  $dF/dE \propto E^{-(\Gamma-1)}$  for flux  $F$ . This figure comes

about both on the basis of experimental observations (no EGRET or observed VHE spectrum is harder than this value) and theoretical arguments. The standard value for a single-zone SSC spectrum is  $\Gamma = (\alpha + 1)/2$ ; here  $-\alpha$  is the spectral index of the shock-accelerated electrons, which is not harder than 2.0 in most acceleration models with radiative cooling (Aharonian, 2001). Note that a slope of -1.5 in a log-log plot of  $dN/dE$  corresponds to positive slope 0.5 for a logarithmic plot of flux  $\nu F_\nu$ , which is dimensionally equivalent  $E^2 dN/dE$ . This limit can be invalidated by assuming a non-standard spectrum for the electrons; a low energy cutoff in the electron energy will lead to inverse-Compton scattered photons with an index as low as  $\Gamma = 2/3$  (Katarzyński et al., 2006). The most recent limits on the EBL come from observations of blazars at more distant redshifts ( $z > 0.1$ ) that have been detected by the current generation of ground-based IACTs. Observation by H.E.S.S. of two blazars at  $z=0.165$  and  $0.186$  were used to set limits on the near-IR EBL based on the  $\Gamma \geq 1.5$  criterion (Aharonian et al., 2006); in this case the maximal limit was the model of Primack et al. (2001) multiplied by a factor of 0.45. It should be noted that the 2005 EBL prediction of Primack et al. (2005) included an optical and near-IR flux even lower than this older model with the multiplier of 0.45. Another paper by the H.E.S.S. group set constraints from blazar 1ES 0229+200 at  $z=0.1396$  (Aharonian et al., 2007b). While this blazar is a closer source than the two featured in the 2006 publication, the observed spectrum extended above 10 TeV and therefore probed the background in the mid-IR. In this regime, the effect of optical depth on spectral modification is minimal due to the approximate  $\lambda^{-1}$  falloff in EBL flux. The limits derived in this case are well above the Primack et al.

(2005) model for a couple of different spectral slopes considered. The observation of quasar 3C279 at  $z=0.536$  by the MAGIC experiment during a flare in February 2006 (Teshima et al., 2008) presented an opportunity of place strong limits on the evolving EBL. The spectrum observed was quite steep,  $4.1 \pm 0.7_{stat} \pm 0.2_{sys}$ , and extended from about 80 to nearly 500 GeV. An analysis of the spectral modification (Albert et al., 2008a) found that there was little room for an EBL flux in the optical higher than one consistent with lower limits from number counts, approximately equivalent to the model of Primack et al. (2005). This paper used a modified version of the ‘best fit’ model from Kneiske et al. (2004) as the upper limit in the optical and near-IR from their finding. An alternative analysis of the spectral deconvolution of 3C279 by Stecker & Scully (2009) disputed this analysis and argued that the higher EBL of Stecker et al. (2006, 2007) could still lead to a steep best-fit spectrum.

Another approach to the problem is to attempt to constrain the EBL by using spectra from several sources simultaneously. Dwek & Krennrich (2005) considered 12 such permutations, and derived an upper limit at  $60\mu\text{m}$  by declaring invalid those realizations leading to unphysical intrinsic blazar spectra with sharply rising TeV emissions. However this is not completely certain, since it has also been argued that such exponential rises are not excluded (Aharonian et al., 2002). An effort by Costamante et al. (2004) used observations of 4 blazars by HEGRA to limit the EBL in the near-IR and at 60 microns with limiting  $\Gamma \geq 1.0$  and 1.5. More recently, this method was used in Mazin & Raue (2007), who applied constraints from all observed TeV blazars to a large number of possible EBL functional forms created using a spline interpolation

across a grid in flux versus wavelength space. The lower bound of the union of excluded models formed an envelope representing the highest possible background that does not violate any constraints. This was done for ‘realistic’ and ‘extreme’ bounds of  $\Gamma \geq 1.5$  and  $2/3$  respectively, and provided a limit on the EBL from the optical to the far-IR. The extreme limit, with  $\Gamma \geq 2/3$ , is motivated by the limiting case of a truncation at a low energy bound for the relativistic electrons responsible for the IC component (see Katarzyński et al., 2006).

In Figure 4.5, we show recent upper limits from gamma-ray observations in relation to the  $z = 0$  EBL from our models. All of our models are in agreement with these bounds across all wavelengths. It is worth pointing out here that, in general, one should use caution in evaluating these constraints. These limits on the present-day EBL do not take into account the differences in evolution occurring in different EBL models, which becomes increasingly problematic with redshift. As we will see when we compare against other EBL models, the difference in emissivity evolution alone can be significant at  $z = 0.18$ , and certainly at  $z = 0.536$ , the redshift of 3C279. Also, the limits from Aharonian et al. (2006) and Albert et al. (2008a) assume specific forms for the optical peak of the background SED (respectively, these are taken from the models of Primack et al. (2001) and a modified version of Kneiske et al. (2004)). The exact normalization of the upper bound is dependent upon this choice. The method used by Mazin & Raue avoids this second issue, but at a cost of more conservative limits resulting from considering a finite grid in flux–wavelength space.

The photon density of the EBL increases with wavelength at almost all energies

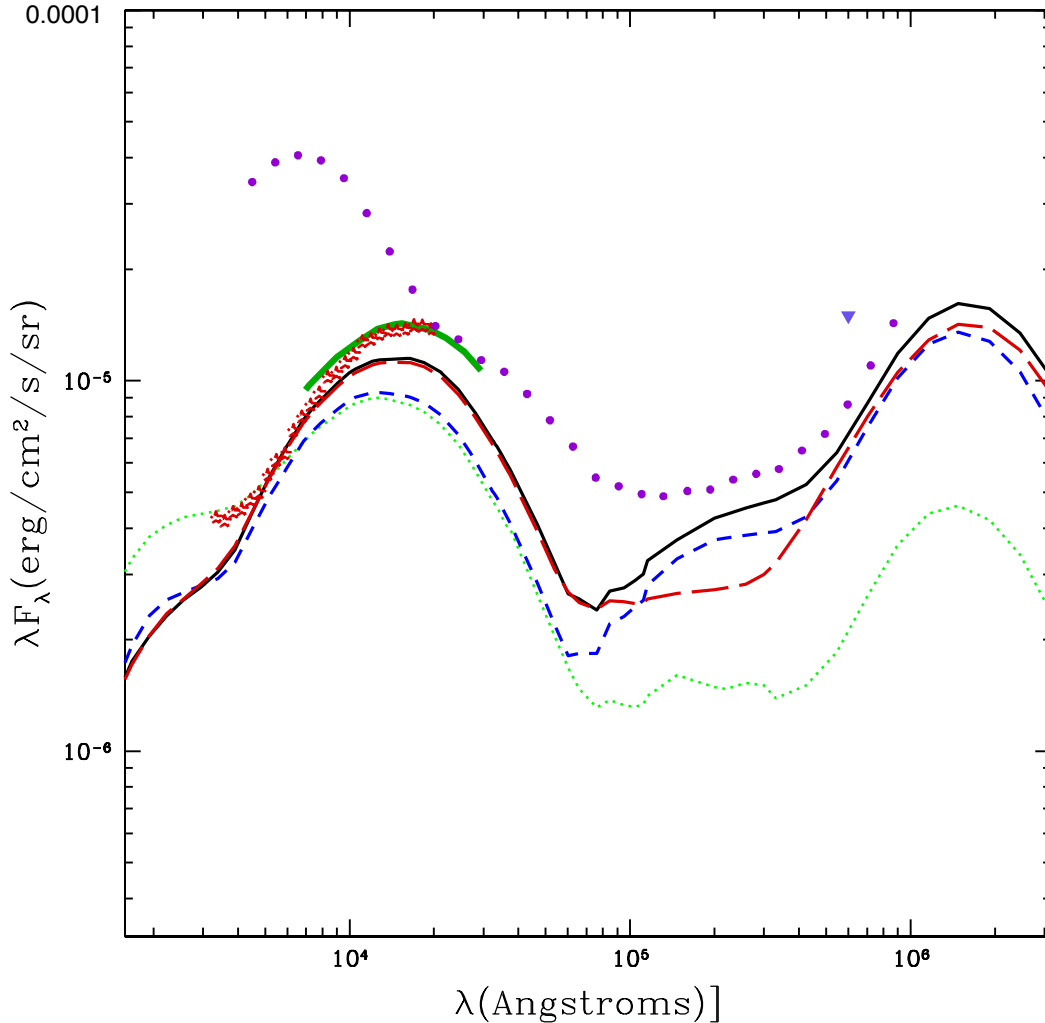


Figure 4.5: Present-day flux predicted in our 3 EBL models, compared against upper limits from gamma-ray observations. The models shown are as in Figure 3.9; solid black and dashed blue lines are fiducial and low models using the Devriendt dust templates, and dashed red is the fiducial model with Rieke templates. The SED from Primack et al. (2005) is also shown as dotted green. Upper limits are from Aharonian et al. (2006) (thick green line), MAGIC observations of 3C279 (Albert et al., 2008a) (red stars), the combined analyses of Mazin & Raue (2007) (purple dots) and Dwek & Krennrich (2005) (indigo triangle). The reader should consult the text for more details and caveats in interpreting this figure.

relevant to gamma-ray attenuation, and therefore the effect on high energy spectra is always a spectral softening. However, it is possible that local radiation in the vicinity of a source could have other effects on the spectrum. This is particularly true for FSRQ sources such as 3C279. As a quasar, 3C279 is a much more powerful source at optical and UV wavelengths than BL Lac objects. It has therefore been suggested that internal absorption from the broad-line region of the quasar could harden the spectrum by creating an optical depth that decreases with energy over the observed interval (Aharonian et al., 2008b), due to emission in a narrow band of UV wavelengths. An analysis by Tavecchio & Mazin (2009) claimed that while significant internal absorption was likely, only the more extreme models of the broad line region lead to an actual hardening of the intrinsic spectrum, and these models lead to a large decrease in flux from absorption, by a typical factor of  $> 10^3$ . More reasonable models with less total absorption were found to leave the spectral index softened or unmodified.

#### 4.4.1 Effects on Known VHE Blazars

We have calculated absorption from each of our EBL realizations in the observed spectra of known blazars that are approximated by power-law functions, and determined the approximate power law of the de-absorbed spectra. The spectra from these objects are not expected to be power laws over large energy ranges. The most simple theoretical form of the spectra from SSC emission is a double-peaked distribution (when plotted as  $\nu F_\nu$ ), which arises from synchrotron radiation of lower energy photons and inverse Compton upscattering of those same photons to gamma-rays. In this model,

the power law measured at VHE scales is an approximation to a section of the inverse Compton peak.

Also, the effect of gamma-ray attenuation through pair production does not in general preserve a power-law form, as can be seen in the optical depth plot, Figure 4.3. Quantifying attenuation as a simple modification to an intrinsic spectral index is an approximation which is only valid when considering short intervals in energy and fairly low redshifts. The EBL attenuation has also been described as an decaying exponential function in energy that affects the spectra above some threshold. However, this is a misleading functional description of the optical depth. The sharp increase in absorption in Figure 4.3 which appears at multi-TeV energies is caused by the rapid increase in photon density as one transitions from the mid-IR minimum in the EBL SED and into redshift-broadened PAH region and far-IR peak (note that our SED is plotted in terms of flux density, not number density). This part of the EBL is created by re-emitted light from cold dust, much of which originates in rapidly star-forming galaxies, and there is no reason to believe that this absorption feature would be related to an exponential form. The power law and the exponential cut-off, which are often used to describe gamma-ray spectra, are not amenable to describing the full non-linear effects of EBL absorption, which is a line-of-sight integral over the evolving photon field. Our optical depths for nearby sources are relatively straight from a couple hundred GeV out to this turnover region, so we present results for sources with spectra measured in this energy range.

One other note concerns the integration over bins of finite width in energy. As attenuation differs across these intervals, it changes the weighting of data and therefore

the mean within the bin. Properly de-absorbing spectral data points requires incorporating the optical depth into the analysis used to produce the points, and not just multiplying by  $e^\tau$  at the mean of the bin. Correlations between the data points must also be accounted for in effectively measuring error. The effect of analyzing the data with a simple multiplication of data introduces an error which is likely to grow with redshift.

Object ID	Redshift	Reference	Experiment	$E_{L\gamma}$	$E_{H\gamma}$	$\Gamma_{obs}$	$\Gamma_{fid}$	$\Gamma_{low}$	$\Gamma_{fid(Rieke)}$
Mrk 421 (+)	0.030	Konopelko et al. (2008)	Whipple	0.2	8.0	2.66	2.45	2.49	2.49
Mrk 421	0.030	Aharonian et al. (1999)	HEGRA	0.5	7.0	$3.09 \pm 0.07$	2.87	2.91	2.91
IES 2344+514	0.044	Albert et al. (2007d)	MAGIC	0.14	5.4	$2.95 \pm 0.12 \pm 0.20$	2.69	2.74	2.72
IES 1959+650	0.047	Albert et al. (2006c)	MAGIC	0.18	2.0	$2.72 \pm 0.14$	2.48	2.55	2.49
IES 1959+650 (-)	0.047	Tagliatierra et al. (2008)	MAGIC	0.150	3.0	$2.58 \pm 0.18$	2.36	2.41	2.36
IES 1959+650 (+)	0.047	Daniel et al. (2005)	Whipple	0.38	18.0	$2.78 \pm 0.12 \pm 0.21$	1.53	1.72	1.92
PKS 2155-304	0.116	Aharonian et al. (2005b)	H.E.S.S.	0.160	0.700	$3.32 \pm 0.06$	2.82	2.96	2.86
H 1426+428	0.129	Aharonian et al. (2002)	HEGRA	1.0	10.0	$2.60 \pm 0.60 \pm 0.1$	1.36	1.71	1.69
PKS 2005-489	0.071	Aharonian et al. (2005a)	H.E.S.S.	0.2	2.5	$4.0 \pm 0.4$	3.63	3.73	3.63
IES 1218+304	0.182	Albert et al. (2006a)	MAGIC	0.09	0.63	$3.00 \pm 0.4$	2.40	2.52	2.39
ES 1218+304	0.182	Fortin (2008)	VERITAS	0.16	1.8	$3.08 \pm 0.34 \pm 0.20$	2.16	2.39	2.15
H 2356-309	0.165	Aharonian et al. (2006)	H.E.S.S.	0.16	1.0	$3.06 \pm 0.40$	2.26	2.45	2.26
IES 1101-232	0.186	Aharonian et al. (2006)	H.E.S.S.	0.16	3.3	$2.88 \pm 0.17$	1.88	2.12	1.91
Mrk 180 (+)	0.045	Albert et al. (2006b)	MAGIC	0.2	1.5	$3.30 \pm 0.70$	3.07	3.12	3.07
BL Lacertae	0.069	Albert et al. (2007b)	MAGIC	0.15	0.9	$3.60 \pm 0.50$	3.31	3.37	3.30
IES 1011+496 (+)	0.212	Albert et al. (2007c)	MAGIC	0.12	0.75	$4.00 \pm 0.50$	3.14	3.33	3.13
IES 0229+200	0.139	Aharonian et al. (2007b)	H.E.S.S.	0.5	15.0	$2.50 \pm 0.19 \pm 0.10$	0.60	0.78	0.95
IES 0347-121	0.188	Aharonian et al. (2007a)	H.E.S.S.	0.25	3.0	$3.10 \pm 0.23 \pm 0.10$	2.00	2.28	2.02
W Comae (+)	0.102	Cogan (2008)	VERITAS	0.15	2.8	$3.81 \pm 0.35 \pm 0.34$	3.32	3.44	3.32
3C279 (+)	0.536	Albert et al. (2008a)	MAGIC	0.09	0.48	$4.11 \pm 0.68$	2.12	2.59	2.08
IES 0806+524	0.138	Acciari et al. (2009a)	VERITAS	0.3	0.7	$3.6 \pm 1.0 \pm 0.3$	2.84	3.01	2.84
3C66A (+)	0.444†	Acciari et al. (2009b)	VERITAS	0.2	0.5	$4.1 \pm 0.4 \pm 0.6$	1.82	2.36	1.78

Table 4.1: Reconstruction of the VHE spectral indices of a number of blazars using our three EBL realizations.  $\Gamma_{obs}$  is the index reported by the given reference at energies between  $E_{L\gamma}$  and  $E_{H\gamma}$ , reported in TeV. These are taken from the reference if explicitly stated, otherwise the highest and lowest data points presented are used.  $\Gamma_{fid}$ ,  $\Gamma_{low}$ , and  $\Gamma_{fid(Rieke)}$  are the average intrinsic indices after de-absorption by our three EBL models presented in the last chapter, over the range of energies claimed in the detections. Errors on this quantity are the same as in the observed indices, if provided by the author. Plus (+) and minus (-) after the source name are used to signify that the detection was claimed in an abnormally high or low state; readers should consult the references given for further details. Many of these reference were taken from Wagner (2008).

† The redshift of 3C66A quoted here is based upon two measurements of weak, single emission lines, and is considered uncertain; see reference for details.

Having warned the reader of these caveats, we present results for known blazars seen above  $\sim 100$  GeV in Table 4.4.1. Most of the objects presented are of the high frequency-peaked BL Lac (HBL) type, with the exceptions of intermediate-peaked W Comae and 3C66A, low-peaked BL Lacertae, and flat spectrum radio quasar 3C279. Values from this table should only be taken as approximate, particularly for more distant sources. In the cases where the spectrum is claimed to continue above the turnover in optical depths seen at several TeV, the results become strongly dependent upon the highest energy extent of the fit. We have used the level claimed by the authors in each case, or when an explicit value is not mentioned, the highest energy point displayed in the spectrum in the reference. In the case of 3C279, which is at a redshift more than twice that of most of the other sources listed, there is likely to be significant error in our estimate of the spectral modification, compared to the method of Albert et al. (2008a) which included the de-absorption in the data analysis.

It is argued in at least a couple of cases (Markarian 421 and 501, (Konopelko et al., 2003)) that the de-absorbed spectrum shows the rollover at the top of the IC peak. Recent MAGIC observations of Mrk 501 have detected a spectral peak at energies which vary in correlation with flaring activity (Albert et al., 2007e). As simple power-law functions do not provide a good fit in this case, we have omitted Mrk 501 from our analysis. Two spectra in our analysis show unusually hard reconstructed spectra. In the case of H 1426+428 (Aharonian et al., 2002), the reported spectrum which we have used does not conform well to a power law, a fact that the authors attribute to EBL absorption. The spectral index of 1ES 0229+200 (Aharonian et al., 2007b) is sensitive

to the highest energies used in the calculation. If we disregard the highest energy data point and instead cut off the spectrum at the second-highest point,  $\approx 6$  TeV, we find more reasonable indices  $\Gamma_{fid} = 1.30$  and  $\Gamma_{low} = 1.49$ , both within one  $1\sigma$  of 1.5, after accounting for both statistical and systematic error, and  $\Gamma_{fid(Rieke)}=1.52$ . In general, the reconstructed spectral indices for spectra extending above a few TeV are highly sensitive to the highest energy data point included.

It is also interesting to compare the effect that dust modeling has on spectral reconstruction, by comparing the results of the Devriendt and Rieke templates. The closest blazars typically have spectra that extend well above 1 TeV, and therefore are affected by the wavelength regime where dust modeling is uncertain ( $\gtrsim 10\mu\text{m}$ ) and our dust templates produce different results. Higher redshift blazars have generally only been seen at lower energies, where gamma-ray attenuation is produced by the optical-near IR EBL peak created mostly by redshifted direct starlight. None of the blazars in our sample at redshifts higher than about 0.15 has a spectral reconstruction that is significantly affected by dust modeling. This may change as more sensitive observations take place in the future, but it does give an indication of the maximum redshift at which dust reemission has a practical effect on gamma-ray observations.

The results in the table are also shown in graphical form in Figure 4.6. This plot shows the amount of change in spectral index after EBL deconvolution for a number of blazars, as a function of source redshift. The results for the fiducial model using Rieke templates are not shown here, as this model does not usually lead to results that are appreciably different from the other two.

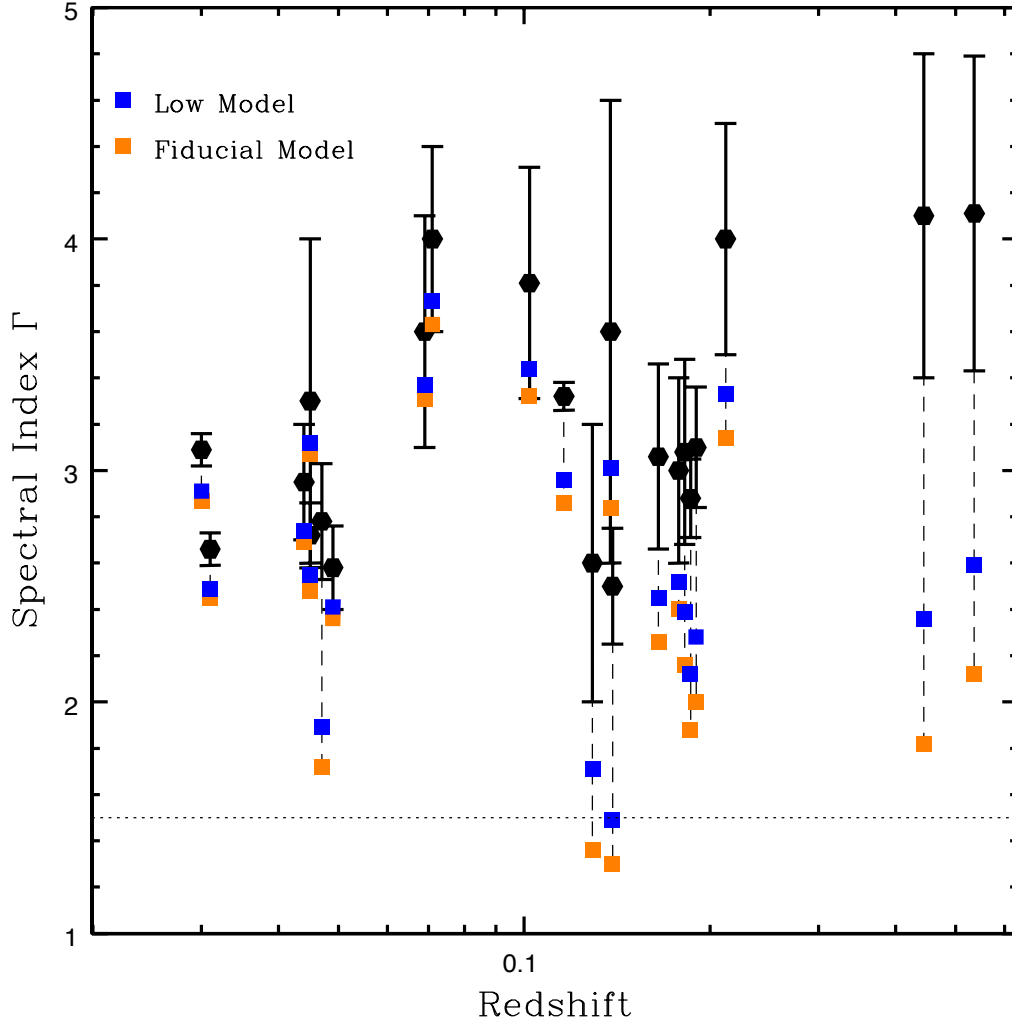


Figure 4.6: Here we show the results of Table 4.4.1 in graphical form. The measured spectral index ( $\Gamma$ ;  $dN/dE \propto E^{-\Gamma}$ ) and redshift of each blazar is shown as a black square with error bars, with the spectrum corrected via the fiducial EBL shown as a orange (lower) point and that of the low EBL in blue (higher). The horizontal dotted line shows  $\Gamma = 1.5$ , which is typically taken as the hardest spectrum possible under usual assumptions. Some points have been shifted sideways slightly for readability.

Given a background model, gamma-ray attenuation can be used to place limits on the redshift of the source. As mentioned in Acciari et al. (2009b), determining the redshift of blazars can be difficult due to the lack of strong line emission. The redshift of 3C 66A was initially determined from a single line, taken to be magnesium-II, and corroborated by a weak Ly $\alpha$  detection. Assuming this is correct, we find for this blazar a reconstructed spectrum that is harder than many others on the list, but still significantly softer than the standard limit. There is also a large amount of uncertainty in the reported spectral index. The case of PKS 1553+113 provides another opportunity to apply our model. This HBL has been detected by both MAGIC (Wagner et al., 2008) and H.E.S.S. (Aharonian et al., 2008a), but the redshift remains unknown at this time. Observations with the HST have been unable to find a precise distance, but suggest a redshift in the range  $0.3 < z < 0.4$  (Treves et al., 2007). If true, this object would be the second most distant source yet detected above 100 GeV, and the most distant BL Lac object. We can put an upper limit on the redshift using our two calculations of the EBL and the standard spectral limit  $\Gamma \geq 1.5$ . We find that in our fiducial EBL realization this object cannot be farther than  $z = 0.64$  based on MAGIC data, or  $z = 0.47$  using the H.E.S.S. spectrum, which goes to higher energies. Repeating this analysis with our low model, we find limits of  $z < 0.85$  and  $z < 0.67$  using the same data. In each case, we have used the claimed spectral index plus  $1\sigma$  to find a conservative limit. A similar analysis by Mazin & Goebel (2007) using a low-level EBL similar to the level set by galaxy counts found an upper limit of  $z < 0.69$ . Reconstructing the intrinsic spectrum at higher redshifts also was found to lead to a break in the power-law shape. Demanding

that such a break be absent leads to a tighter upper limit in this reference,  $z < 0.42$ .

## 4.5 Comparison with Other Work

In this section we compare the methodology and results of our EBL determination with others in the recent literature, including the previous products of our semi-analytic model. Our prior prediction for the EBL, presented in Primack et al. (2005), used a similar semi-analytic model of structure formation to that used in this work. The low model presented here has similar normalization to the 2005 model, leading to low flux in the optical and near-IR, with only a small amount of light unresolved in the deepest number count surveys. The differences in the spectral shape of the optical peaks are due to changes in the application of the dust absorption prescriptions; in this work we use the two-component model of Charlot & Fall (2000), which leads to more absorption in the UV and emission in the mid- and far-IR. Our implementation of the Devriendt templates has not changed. The fiducial model we have presented features a higher level of star-formation, particularly at early times, as a result of assuming a larger normalization in the initial dark matter power spectrum.

The EBL model of Franceschini et al. (2008) is based upon the interpolation of luminosity functions from a variety of survey data. Recognizing the need for separate treatments of evolution in different wavelength regimes, this model treats optical and IR components separately, using the recent body of data from Spitzer and other experiments. The  $z=0$  EBL calculated by these authors is quite similar to our own in

the optical and near-IR; it has a substantially higher peak in the far-IR and somewhat lower flux from 10 to 30  $\mu\text{m}$  than either of our models. As their model has been derived from the same body of cosmological data that our own have been carefully compared against, it is not surprising to see similar predictions at low redshift. A comparison of the infrared prediction from the evolving 24 $\mu\text{m}$  luminosity function in this work has been deferred to a future paper. In Figure 4.7 we show the EBL from our models compared with those of Franceschini et al. (2008), as well as the best fit model in Kneiske et al. (2004), and the two models presented in Stecker et al. (2006), which we discuss in the next two paragraphs, at  $z = 0$  and 1. Our model is seen to evolve similarly to the Franceschini model out to redshift 1.

The work of Kneiske et al. (2002) calculated the EBL from the UV to far-IR using a ‘semi-empirical’ method based on measured star formation rates and spectral synthesis models. Light is reprocessed by dust and gas; dust is modeled as a blackbody with 3 temperature components. Metallicity is assumed to increase slowly over cosmic time and an average global extinction curve is applied to starlight. A follow-up paper, Kneiske et al. (2004), expanded this earlier model into 6 realizations, varying in gas temperature contribution, star formation rate, and UV escape fraction. The ‘best-fit’ EBL in Kneiske et al. (2004) is considerably higher than our fiducial model in both the optical and far-IR peaks. While the methods employed in these papers are quite different from our own and are not easily compared, the discrepancy likely originates in the star formation rate densities assumed, which have a much different functional form than predictions from our model (Figure 3.1). The result from the Kneiske et al. papers

is based upon a broken power-law for the star-formation history, with a peak at  $z = 1.2$ . Our own history is considerably lower in this epoch, and does not peak until  $z \approx 3$  for our fiducial model, or  $z \approx 2.25$  for the low WMAP3 model (Figure 3.1). Thus our models have a lower present-day flux, but more at redshifts at and above the peak in their star-formation rate. The use of a blackbody spectrum to approximate emission in the PAH region also gives their EBL SED a somewhat different shape in the mid-IR than we find with our templates that include these sharp emission features.

The models of Stecker and collaborators, most recently Stecker et al. (2006, 2007), have explored the background using backward evolution models. This most recent work proposed two SEDs for the EBL, using two different assumptions about the pure luminosity evolution (PLE) of the  $60 \mu\text{m}$  luminosity function. The SEDs of all galaxies are assumed to be determined by this  $60 \mu\text{m}$  emissivity. The ‘baseline’ model features a PLE multiplier of  $(1+z)^{3.1}$  out to  $z=1.4$ , and constant luminosity from there to  $z=6$ . The ‘fast evolution’ model evolves even quicker, as  $\sim (1+z)^4$  to  $z=0.8$  and  $\sim (1+z)^2$  for  $0.8 < z < 1.5$ . Both of these models are considerably higher than ours in the optical and near-IR, with the fast evolution model about 50% higher in this range than the baseline; the discrepancy in the far-IR with our models is smaller. It is difficult to compare our model, which deals with galaxies in a system of hierarchically merging dark matter halos, with this model, in which it is assumed that the present galaxy population grows brighter with redshift. Our  $60 \mu\text{m}$  luminosity density is not found to increase nearly as quickly as assumed in either of these models. In both of our models it can be well-described by a luminosity density multiplier of  $\sim (1+z)^{1.7}$

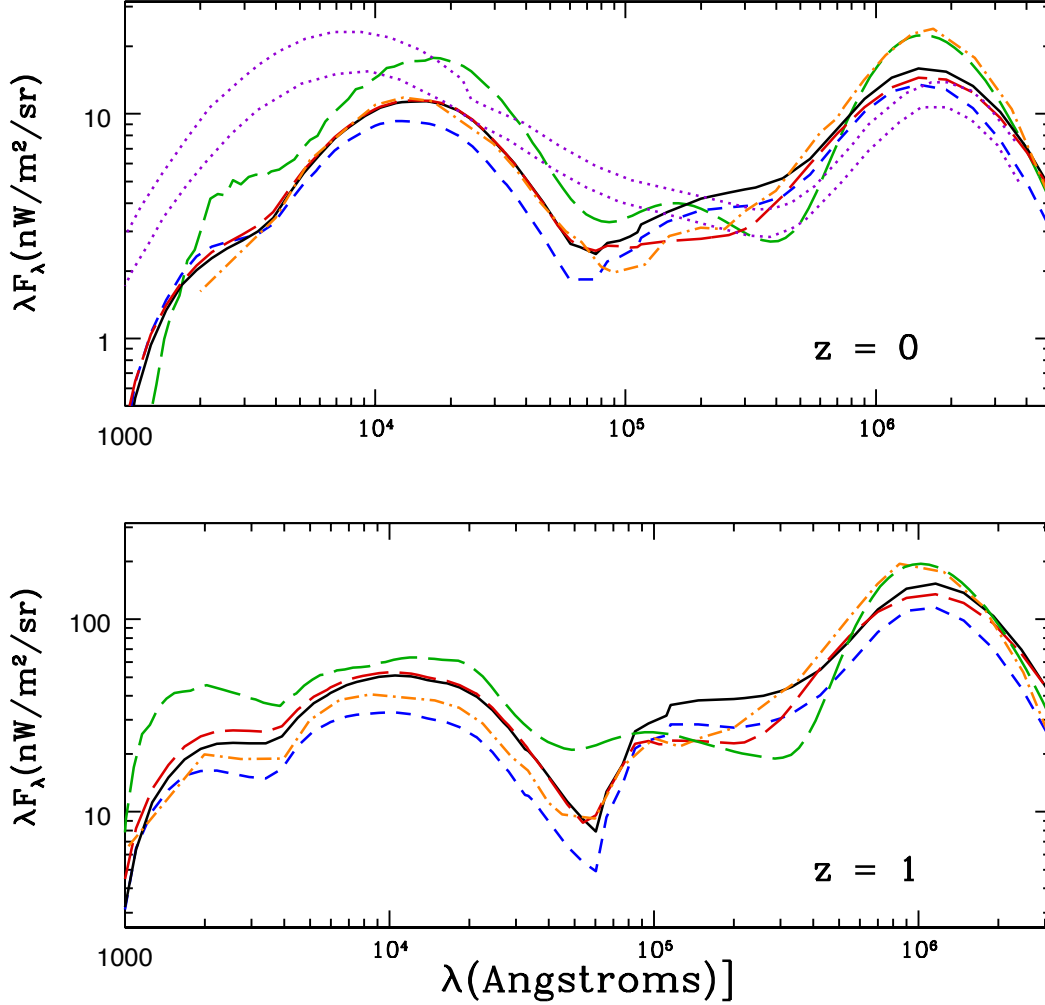


Figure 4.7: Our EBL models compared with those of (Franceschini et al., 2008) and the best-fit model of (Kneiske et al., 2004), at present-day and  $z = 1$ . In each plot, our fiducial and low models with Devriendt dust templates are solid black and dashed blue, respectively, and the fiducial model using Rieke templates is long-dashed red. Kneiske’s best-fit model is shown as long-dashed green and Franceschini as dot-dashed orange. The baseline and fast evolution models of Stecker et al. (2006) are the low and high dotted violet points in the  $z = 0$  panel.

out to  $z \approx 1.4$  at this wavelength. As mentioned above, the high optical and near-IR flux of the fast-evolution model puts it at odds with the detection of 3C279 by MAGIC (Albert et al., 2008a), which was disputed by Stecker in another analysis (Stecker & Scully, 2009). However, the large error on the determined de-absorbed spectral index ( $0.5 \pm 1.2$ ), and the possibility of hardening of the spectrum by internal absorption (Liu et al. 2008, Aharonian et al. 2008b, but see also Tavecchio & Mazin 2009), make it difficult to claim this observation as a firm limit on the EBL. Further observations of this and other high-redshift sources will likely improve constraints on flux in the optical EBL peak.

## 4.6 Discussion

The EBL presents one of the primary barriers to extragalactic gamma-ray astronomy with ground-based instruments. Our determination of a fairly low extragalactic background, supported by convergence with alternative methods such as Franceschini et al. (2008) as well as recent limits from gamma-ray experiments in the optical to mid-IR, is an optimistic prediction for the future of the field. The ability of current- and next-generation experiments to detect blazars at higher distances is a function of several factors: the luminosity function and spectral evolution of these objects, the effective area (especially at the lowest energies) and duty cycles of these instruments, and the details of the increasingly uncertain non-local EBL at higher redshifts. Considerable progress on the instrumentation front suggests that an explosion of new detections

may be coming. The energy thresholds of the upcoming upgrades to the H.E.S.S. and MAGIC experiments will be pushed down below 50 GeV. The upgrade to MAGIC, which is operational at the time of writing, consists of a second 17-meter telescope and an improved triggering system (Carmona et al., 2007). H.E.S.S. is currently adding a central 32 by 24 meter dish to its current array of four 12-meter instruments. This central dish is expected to see gamma-rays at energies as low as 20 GeV (Horns, 2006).

The Fermi Gamma-ray Space Telescope is now in survey mode and viewing the entire sky every 3 hours. In addition to detecting a large number of extragalactic sources in its own right, it will serve as a valuable tool to ground-based IACTs by acting as a finder of flaring blazars. Follow-up observations by IACTs to Fermi discoveries and opportunistic viewing of reported flaring sources will effectively enhance the discovery capabilities of these current instruments. We will discuss Fermi's capabilities more in the next two chapters, which specifically target the high-redshift UV background.

The advent of these new detectors requires a shift in the nature of our studies of background absorption, as the emphasis shifts to larger redshifts and lower energies. As mentioned, the approximation of a local EBL in optical depth calculations is only valid for close extragalactic observations. At redshifts above  $\sim 0.3$ , differences in the evolution of star formation and galaxy emissivity begin to have a substantial effect on attenuation; two different EBL models with the same present-day normalization could have widely varying behavior at these times. For instance, the Kneiske models and Stecker's fast evolution models have star-formation history peaks at a lower redshift than we assume. In addition to predicting different results for the present-day EBL than

our model, the evolution with redshift is also quite a bit different in these cases. As no direct observations of the EBL or number counts exist at nonzero redshift, predicting attenuation from sources past these distances must be made on the basis of models of galaxy evolution, constrained by surveys of luminosity functions at high-redshift. Recent surveys of the non-local universe such as DEEP2 and the multi-wavelength GOODS and AEGIS surveys will help provide constraints to the EBL at these distances. An upcoming companion paper to this work will provide a detailed comparison of our current models to high-redshift luminosity function data, with a discussion of the limits in current data and future prospects. This will help establish how reliable our predictions for the evolving EBL are at high redshifts.

The other impact of the shift to higher redshift observations by lower energy-threshold instruments is the change in the relevant absorbing photon population to UV wavelengths. Our models, and the others we reference in the last section, predict a rapid falloff in transmission of gamma rays above 500 GeV for blazars at the redshift of 3C279. Detecting emission at or above 1 TeV from sources at this distance will require orders-of-magnitude gains in instrument effective area, or observations of flare events with similar increases in output. The energy range of primary interest for these types of sources is going to be 50 to 500 GeV for the next generation of IACTs, plus lower energy data from Fermi. Below 200 GeV, it is the UV background that is primarily responsible for absorption, and at energies much below 80 GeV it is the ionizing background that must be considered. Our background models as presented do not include photons at energies above the Lyman limit. Studies of the ionizing background present additional

difficulties, including the lack of direct observation, the highly uncertain escape fraction of this radiation from star-forming galaxies and contribution from quasars, and the need to model the propagation and processing of this radiation through the inter-galactic medium. We will address the question of the extreme UV in the next chapter, when we use the galaxy models of this work in conjunction with a radiative transfer code and estimates of the quasar emissivity to make flux predictions above the Lyman limit. This model will probe the opacity of the universe to gamma-rays between 1 and 100 GeV.

One other weakness in our model is our use of templates to describe reemission by dust at mid- and far-IR wavelengths. This method makes the assumption that galaxies of a given bolometric luminosity emit light with a similar spectral distribution. Spitzer observations suggest that this is not true at low redshift, and it is likely an even worse approximation for rapidly star-forming galaxies at high redshift, which may require additional cold dust components for correct emission (Symeonidis et al., 2008). Better modeling of dust absorption may rely on a better understanding of the galaxy parameters which most closely correlate with observed spectra. For example, recent models have found that specific star formation rate correlates closely with observed galaxy colors (da Cunha et al., 2008; Jonsson et al., 2006). Using newer templates that account for the changing emission of the most powerful starbursting galaxies at different redshifts will enable us to more closely reproduce number counts and EBL flux in the far-IR, particularly at submillimeter wavelengths. Our hope is that we will eventually be able to treat dust self-consistently in our models, using realistic radiative transfer codes such as SUNRISE (Jonsson, 2006; Jonsson et al., 2006). While there is

much progress to be made modeling this part of the background SED, particularly in matching submillimeter number counts, new models of dust will only have a substantial effect on our calculation of gamma-ray opacities for the nearest sources.

## Chapter 5

# GeV Gamma-ray Attenuation and the High-Redshift UV Background

In this chapter, we focus on modeling the evolving UV and optical background out to the epoch of reionization. In addition to the contribution from stars, as determined by the semi-analytic models discussed in the previous chapters, we included the significant portion of the UV background created by quasars, which has not yet been included in our modeling. We also calculate the reprocessing of ionizing radiation by the intergalactic medium (IGM) using the radiative transfer code CUBA (Haardt & Madau, 1996), and use the observed ionization state of the IGM to constrain our models. Most previous modeling attempts, including our recent work with this new SAM, have focused on observational data in the optical and IR. These are the wavelengths most relevant to observations of relatively nearby ( $z < 0.5$ ) blazars with ground-based instruments, which until recently have typically featured energy thresholds above  $\sim 150$  GeV. With

the recent launch of Fermi with its Large Area Telescope (LAT) sensitivity range of 20 MeV to 300 GeV, as well as the advent of new ground-based experiments such as MAGIC-II with energy thresholds  $< 100$  GeV, it is now important to make theoretical predictions of the UV background at ionizing and non-ionizing wavelengths out to high redshift. This chapter attempts to specifically target absorption in this region of the gamma-ray spectrum. The results presented here are intended to extend the results presented in Chapters 3 and 4 into this high redshift, low gamma-ray energy regime. At gamma-ray energies where interactions with the UV are no longer significant, optical depths predicted here converge to those presented in the last chapter.

## 5.1 Introduction

Understanding the absorption that occurs for gamma rays observed between 1 and 100 GeV is an uncertain undertaking due to the lack of sensitive observations of the EBL at the corresponding UV wavelengths. Moreover, the declining opacities for gamma rays in this region means that sources are likely to be visible out to large redshift. Evolution of the background must be taken into account when calculating absorption for all but the nearest blazars, and at high redshifts the EBL can have a spectral energy distribution (SED) much different than observed locally. The most distant object with confirmed redshift that has been detected at VHE energies is currently the flat-spectrum radio quasar 3C279 (Albert et al., 2008a) at  $z = 0.536$ . This object was observed at energies between 90 and 500 GeV, with a steep spectrum that was likely due in part

to EBL absorption. In the 10 to 100 GeV energy decade that is now being probed by Fermi and upgraded ground experiments, the characteristic redshift at which the EBL becomes optically thick to pair-production is expected to increase to redshifts of several.

A small number of calculations have been performed that specifically addressed the question of the gamma-ray absorption by the UV background. In Madau & Phinney (1996), two different models of star-formation, based on different assumptions about the B-band normalization, were used to predict gamma-ray opacities from 10 to 200 GeV, with propagation of ionizing photons through the IGM taken into account. This work suggested that the universe becomes optically thick at a few tens of GeV for gamma rays emitted at  $z \sim 2$ . A second work which focused on the UV background, Oh (2001), argued that the absorption by ionizing photons was negligible, and that  $< 20$  GeV observed gamma rays would only be significantly attenuated at higher redshifts, where they would interact with photons below the Lyman limit. Ly $\alpha$  photons were found to be a significant component of the UV flux. This paper also explored the possibility of using Fermi to detect an evolving blazar attenuation edge, which would probe high-redshift star-formation. Finally, the background model of Salamon & Stecker (1998) targeted absorption of 10–500 GeV gamma rays, and used an estimate of high-redshift star-formation based on evolution seen in damped Ly $\alpha$  systems. This work also included a UV contribution from quasars.

At energies below the Lyman limit, lower bounds on galaxy emissivity exist from number counts by GALEX (Xu et al., 2005), and HST as well as balloon-based experiments (Gardner, Brown, & Ferguson, 2000). Such experiments are subject to

systematic errors in completeness and photometric measurement of apparent magnitude, and can only test the background out to moderate redshift. At higher redshifts we no longer have measurements that directly connect to the EBL, such as direct number counts and absolute photometry, and uncertainties and possible biases in cosmological measurements such as luminosity functions and star-formation rate density become increasingly problematic.

Measurements of the ionization state of the IGM can provide constraints on ionizing flux. At redshifts higher than the ‘breakthrough redshift’  $\approx 1.6$ , the universe is optically thick to Lyman continuum photons, and ionizing fields become local, with a mean free path that decreases rapidly at larger redshifts (Madau, Haardt, & Rees, 1999), while below this redshift the mean free path becomes longer than the horizon length. Studies of the opacity of Ly $\alpha$  and other redshifted absorption lines place constraints on the emission of UV photons by probing the neutral fraction, and therefore the balance between photoionizations and recombinations (Haehnelt et al., 2001; Madau et al., 2004). As these lines are affected by the local radiation, they provide information about sources existing at approximately the redshift of the absorber (Haardt & Madau, 1996).

Two methods of determining the ionization state of the IGM include the proximity effect, in which one searches for the decrease in Ly $\alpha$  emissions near an AGN (Dall’Aglia, Wisotzki, & Worseck, 2008; Liske & Williger, 2001), and flux decrement analysis, which utilizes hydrodynamic simulations to model the distribution of Ly $\alpha$  absorption along the line of sight to an AGN (e.g. Bolton et al., 2005). The line-of-sight

proximity effect utilizes the decrease in absorption lines in the vicinity of a quasar, compared to farther away along the line of sight, due to increased ionization fraction. As the quasar has a known UV luminosity, the deficit of absorption in this region can be used to estimate the background; a larger change indicates a lower background flux. As quasars do not reside in typical cosmological environments, a number of potential biases exist. Quasars tend to be found in overdense environments, which can lead to overestimates of the background flux by as much as a factor of 3 (Loeb & Eisenstein, 1995). Time variation in luminosity on the time-scale of photoionization, typically  $\sim 10^4$  years, will also tend to bias results towards a high background, as quasars tend to be selected in their brightest phases (Schirber, Miralda-Escudé, & McDonald, 2004). It is also now recognized that using broad emission lines such as Ly $\alpha$  tends to lead to underestimated redshifts and therefore higher quasar luminosity (Richards et al., 2002). This may have been a problem in many determinations of the proximity effect. The assumed cosmological model also affects the resulting background inferred by these measurements. The second method mentioned, the less-direct flux decrement technique (Rauch et al., 1997), is not without its own potential biases; it relies on correct cosmological parameters and knowledge of the quasar’s unabsorbed continuum level, a problem at high redshift where absorption is strong. Newer attempts to correct for the biases in proximity effects measurements, such as Dall’Aglio et al. (2008), have found lower values for the ionizing background flux that are more consistent with the flux decrement technique.

Observations of the Ly $\alpha$  forest can also provide clues about the types of sources producing the ionizing background, which in our model include star-forming galaxies

and quasars. The quasar luminosity function (LF) has been measured by large-scale surveys such as the Two-degree Field (2dF) (Boyle et al., 2000) and the Sloan Digital Sky Survey (SDSS) (Jiang et al., 2006; Richards et al., 2006; Croom et al., 2004), and data are also available at a variety of frequencies from experiments such as XMM, Chandra, and Spitzer (Barger et al., 2005; Matute et al., 2006; Brown et al., 2006). The hydrogen of the intergalactic medium (IGM) is known to be fully ionized below a redshift of  $\sim 6$  (Fan et al., 2006). Photons above the Lyman limit are responsible for reionizing the universe and maintaining it in a highly ionized state. The relative contributions of star-forming galaxies and AGN to this process are not fully understood, but there is evidence that quasars are a sub-dominant component at this epoch. The decline of the quasar luminosity function observed beyond redshift three constrains the quasar contribution to the ionizing background to be  $\sim 10^{-2}$  (Fan et al., 2001; Madau et al., 1999), unless there is an unexpected steep upturn in the quasar luminosity function at low luminosities. A new approach by Srbinovsky & Wyithe (2007) utilizing semi-analytic modeling sets limits on the quasar contribution to ionizing radiation of 1.4 to 14.5 % at  $z = 5.7$ . Another strategy is to constrain the quasar contribution from the unresolved component of the soft X-ray background; Dijkstra, Haiman, & Loeb (2004) found that a 100% contribution from quasars at the time of reionization would oversaturate the observed level. There are also arguments on both observational (Bunker et al., 2004) and theoretical grounds (Gnedin, 2008; Bolton & Haehnelt, 2007) that forming galaxies may not produce sufficient numbers of ionizing photons for hydrogen reionization with standard assumptions.

Increased quasar emission is believed to be responsible for He II reionization, which as tracked by He II Ly $\alpha$  absorption takes place at a lower redshift than hydrogen,  $z \sim 3$  (e.g. Bolton et al., 2005). The shape of the ionizing background therefore evolves in redshift, with a hardening of the spectrum that is indicative of an increased contribution from quasars. The degree to which AGN dominate the UV background at the time of He reionization is a debated issue, with some suggestions that stars and AGN provide roughly equal contributions to the background at  $z \sim 3$  (Kriss et al., 2001; Smette et al., 2002). One of the major sources of uncertainty in this transition lies in the unresolvable faint end of the AGN luminosity function (Schirber & Bullock, 2003). The ratio between hydrogen and helium ionization fractions, particularly H I (13.6 eV) and He II (54.4 eV), can be used to measure the slope of the total UV spectrum in this regime. The decrease in the optical depth of He II indicates that the harder radiation from quasars increases with time between  $z = 5$  and 3 (Shull et al., 2004; Fan et al., 2006).

Aside from quasars, the known dominant sources of UV radiation are short-lived massive stars, mainly of O- and B-type, which closely trace the star formation rate density. Estimating the ionizing contribution from star-forming galaxies directly is complicated by the fact that only a small fraction  $f_{esc}$  of this radiation escapes from galaxies due to neutral gas and dust in the interstellar medium, as we will discuss in Section 2.4.

Because of the uncertain nature and evolution of sources of ionizing radiation, in this chapter we consider four models that attempt to span a realistic range of assumptions. In Section 5.2 we discuss the inputs to our model, including a short de-

scription of our semi-analytic models, assumed quasar luminosity density, and radiative transfer code. In Section 5.3, we introduce our four UV background models and present results, including the evolving background radiation and comparisons with Ly $\alpha$  forest measurements. The main results of the chapter, gamma-ray opacities, are presented in Section 5.4, with a discussion following in Section 5.5. Our four models are summarized in Table 5.1, and their successes and failures in accounting for the data are summarized in Table 5.2.

## 5.2 Modeling

To calculate the evolving UV background we have used predictions of the UV luminosity density from galaxies, as provided by our low and fiducial semi-analytic models (SAMs) of galaxy formation described in Chapters 2 and 3, together with estimates of quasar emissivity. The combined emission from galaxies and quasars is integrated over redshift to find the evolving background flux. Photons from these sources at energies above the Lyman limit can be absorbed and reradiated by the IGM; we calculate the effect of these processes using the CUBA radiative transfer code. In this section we present UV-specific results from our SAMs, and then discuss the radiative transfer code used in calculating the background.

### 5.2.1 UV Output from Semi-Analytic Models

The predictions for attenuated and unattenuated emissivity from our fiducial semi-analytic model are shown for several redshifts in Figure 5.1. Predictions from the

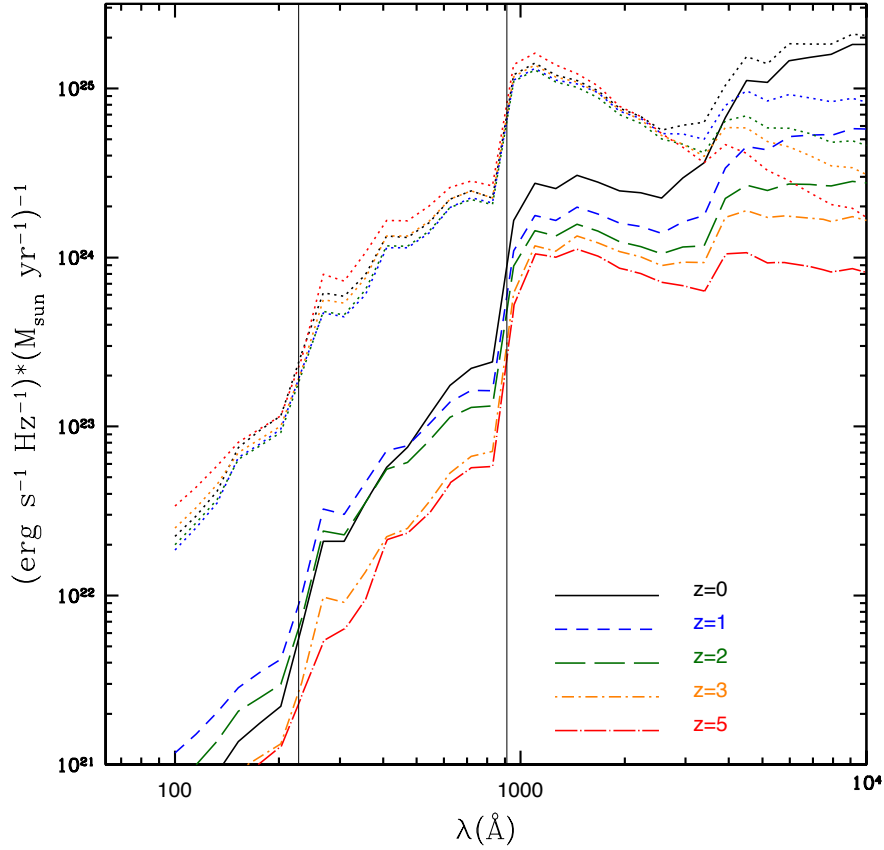


Figure 5.1: The emissivity due to galaxies predicted by our fiducial galaxy-formation model at a number of redshifts, normalized to  $1 M_{\odot}/\text{yr}$ . Dotted curves show the emission predicted in the absence of dust extinction. Vertical lines indicate the ionization energies of H I and He II at 912 and 228 Å.

‘low’ model are qualitatively similar, although because of the delayed star formation, galaxies tend to have higher gas surface densities, and therefore higher dust opacities and larger attenuation values are predicted.

In Figures 5.2 and 5.3 we compare our model predictions with galaxy number counts in two UV bands, using data from the GALEX satellite and other experiments. This provides a test of the low-redshift normalization of our model in the UV range.

GALEX has surveyed the UV sky in two UV bands and provided data down to magnitude  $\sim 23.5$  (Xu et al., 2005). At fainter magnitudes, there are measurements from the STIS instrument on the HST (Gardner et al., 2000), albeit with large uncertainty due to poor statistics. Populations of brighter objects have also been probed by the FOCA balloon-borne UV telescope, and counts from this instrument at  $2000 \text{ \AA}$  have typically yielded higher numbers than GALEX after correction, possibly due to differences in calibration. Our models show good agreement with the data at  $2310 \text{ \AA}$ , but are a bit higher than the GALEX observations at  $1530 \text{ \AA}$ , though they are not in disagreement with the FOCA data.

Recent data from a variety of instruments has constrained the UV luminosity density out to high redshift. In Figure 5.4 we have compared the UV emissivity in galaxies from our models against data at a rest frame emission wavelength of approximately  $1500 \text{ \AA}$ . We find that data from the GALEX-VVDS, GOODS, and Deep HST ACS imaging all agree reasonably well with the UV evolution of our fiducial model. The low model produces a UV luminosity density below that seen in the high redshift data.

### 5.2.2 Star Formation

The star-formation rate density (SFRD) out to high redshift in the ‘fiducial’ and ‘low’ models are shown in Figure 5.5, compared with observational estimates of star formation density at various redshifts, all of which has been converted to a Chabrier initial mass function (IMF). At  $z < 1$ , both of our models are in good agreement with the observational compilation of Hopkins (2004), while at  $1 < z < 2$  they tend to skirt

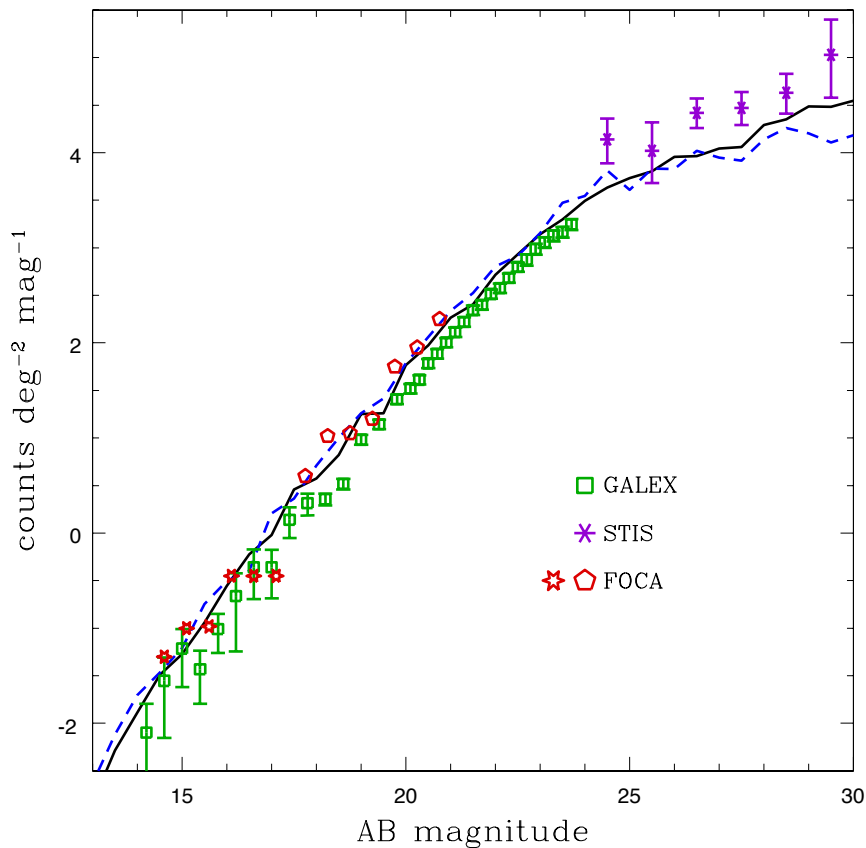


Figure 5.2: Number counts in the GALEX 1530 Å. The solid black line shows the fiducial model, and dashed blue shows the low model. Note that the low model has counts equal to or slightly greater than the fiducial model at some magnitudes due to differing amounts of dust extinction. Data are from GALEX (Xu et al., 2005, green squares), STIS on HST (Gardner et al., 2000, purple asterisks), and the balloon-borne FOCA experiment (Iglesias-Páramo et al., 2004; Milliard et al., 1992, red stars and open pentagons respectively). Following Xu et al. (2005), all counts have been converted to the GALEX band by assuming a UV spectral slope of -0.8.

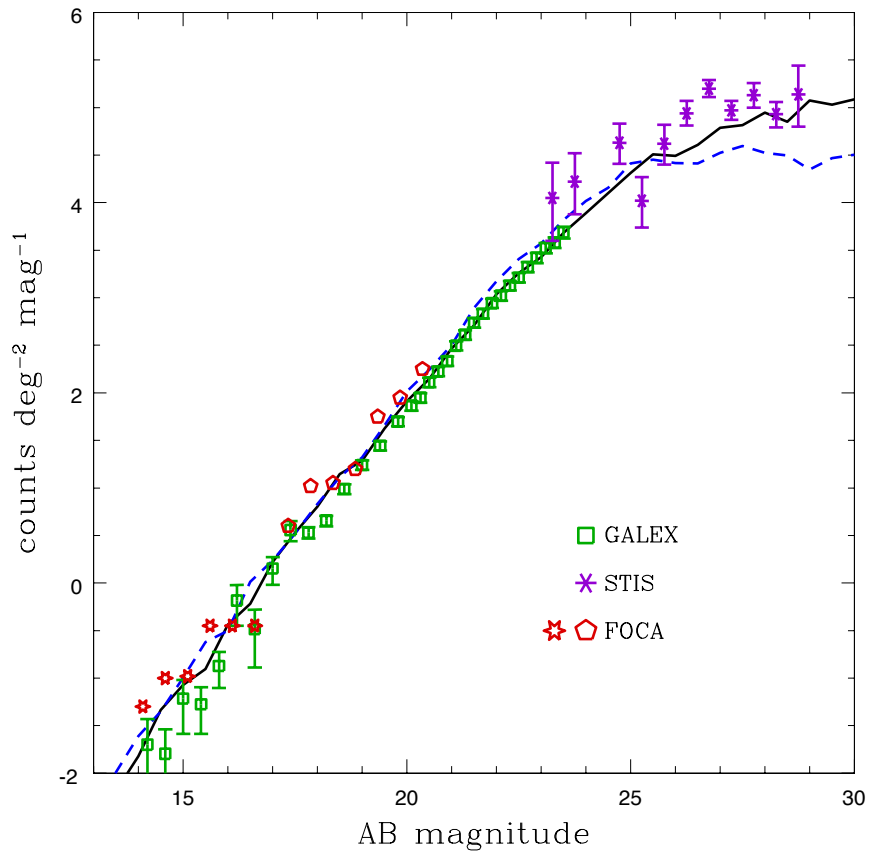


Figure 5.3: Number counts in the GALEX 2310 Å. Curves and data are the same as in the previous figure.

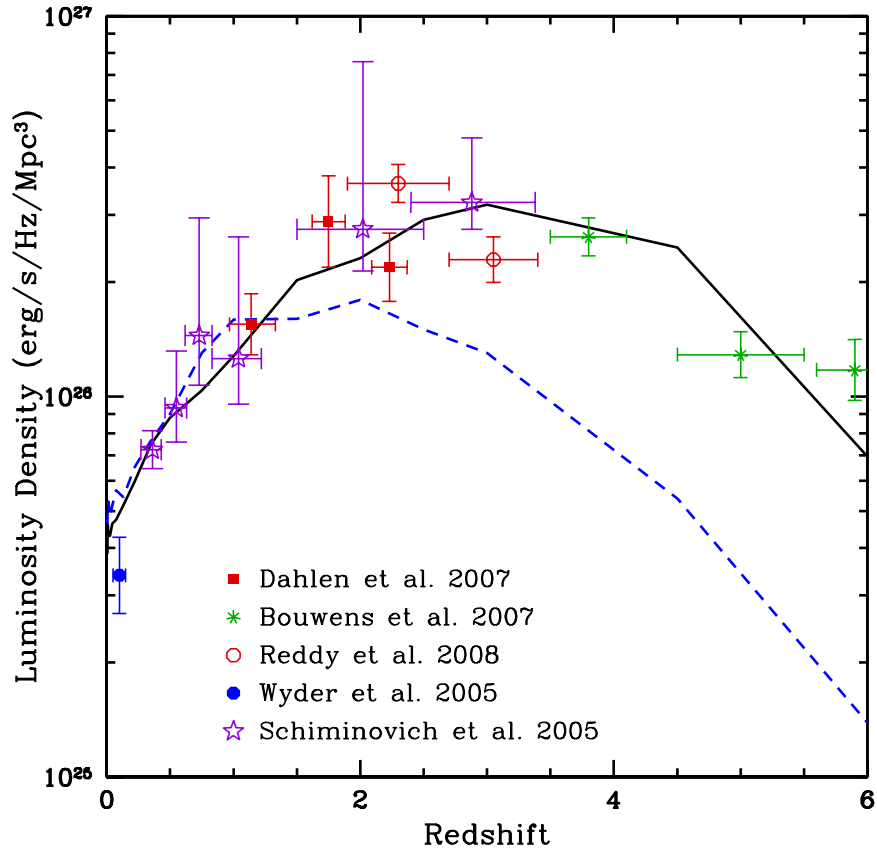


Figure 5.4: The emissivity at 1500 Å as a function of redshift in our models. As previously, the solid black line is the fiducial model, and the dashed blue line shows the low model. The blue circle at redshift 0.1 is GALEX data from Wyder et al. (2005) and the purple stars are measurements using GALEX and other data (Schiminovich et al., 2005). The red squares are from GOODS (Dahlen et al., 2007), the red circles are determinations from ground-based observations (Reddy et al., 2008), and the green stars are from Bouwens et al. (2007).

the lower envelope of observational values. However, there are still large discrepancies between SFR estimates from different indicators and different data sets at these redshifts, in part due to the increased fraction of star formation in heavily obscured systems (e.g. Hopkins, 2007), where the correction for dust obscuration is uncertain. At  $z > 2$ , the SFRD in the ‘low’ model declines fairly steeply, while in the fiducial model the SFRD remains nearly constant from  $2 < z < 5$  and then declines more gradually. As discussed above and in Somerville et al. (2008), this is because of the lower normalization of the power spectrum and reduced small scale power in this model, which delays the formation of structure.

Above redshift four, observational estimates of global star-formation rates diverge, and different measurements can disagree by as much as an order of magnitude. Studies of UV luminosity functions of dropout galaxies by Bouwens and collaborators (Bouwens et al., 2008, 2007) find relatively low values for the global SFR, with a monotonic decrease above redshift four. Higher rates have been found by other authors, including those who have derived star-formation history from detections of gamma-ray bursts (Yüksel et al., 2008). These studies suggest a much higher rate of star formation which does not decrease significantly until  $z > 6$ . This may be due in part to the fact that the Bouwens et al. data points that we report here were obtained by integrating the UV luminosity function down to a luminosity corresponding to 0.04 times the observed value of  $L_*$  at redshift three. Other authors make different choices for the lower limit of integration, and the relatively steep slope of the UV LF at these redshifts implies that this can make a significant difference. The SAM predictions shown include the star

formation in all galaxies (down to the mass resolution of the simulation).

Our ‘low’ semi-analytic model, based on the lower determination of  $\sigma_8$  in WMAP3, produces a star-formation rate that is lower than most of the data points at mid and high redshift, and reproduces the rapid fall-off in star formation indicated by the Bouwens points. Our ‘fiducial’ model, based on WMAP1, does a better job of matching the higher star-formation rates seen in other dropout analyses, as well as the data from gamma-ray bursts.

In addition to the star-formation histories predicted self-consistently in our fiducial and low semi-analytic models, we consider an additional ad hoc high-peaked fiducial form for the SF history above  $z = 3$ . This is not a semi-analytic model; it is simply a functional form that was chosen to be consistent with the highest observational determinations of the star-formation rate. We then utilize the same redshift-dependent dust extinction factors as the fiducial model. We include this case to illustrate the predictions for gamma-ray attenuation for an extreme model with the maximum plausible UV background at high redshift. However, we note that as the fiducial model already produces an integrated stellar mass density in excess of that observed at high redshift, the high-peaked model is strongly disfavoured by these observations.

### 5.2.3 Radiative Transfer

Ionizing photons from galaxies and quasars which escape into the intergalactic medium (IGM) are processed by neutral hydrogen and neutral and singly-ionized helium which resides in Ly $\alpha$  forest clouds (LAC) and thicker Lyman-limit systems (LLS),

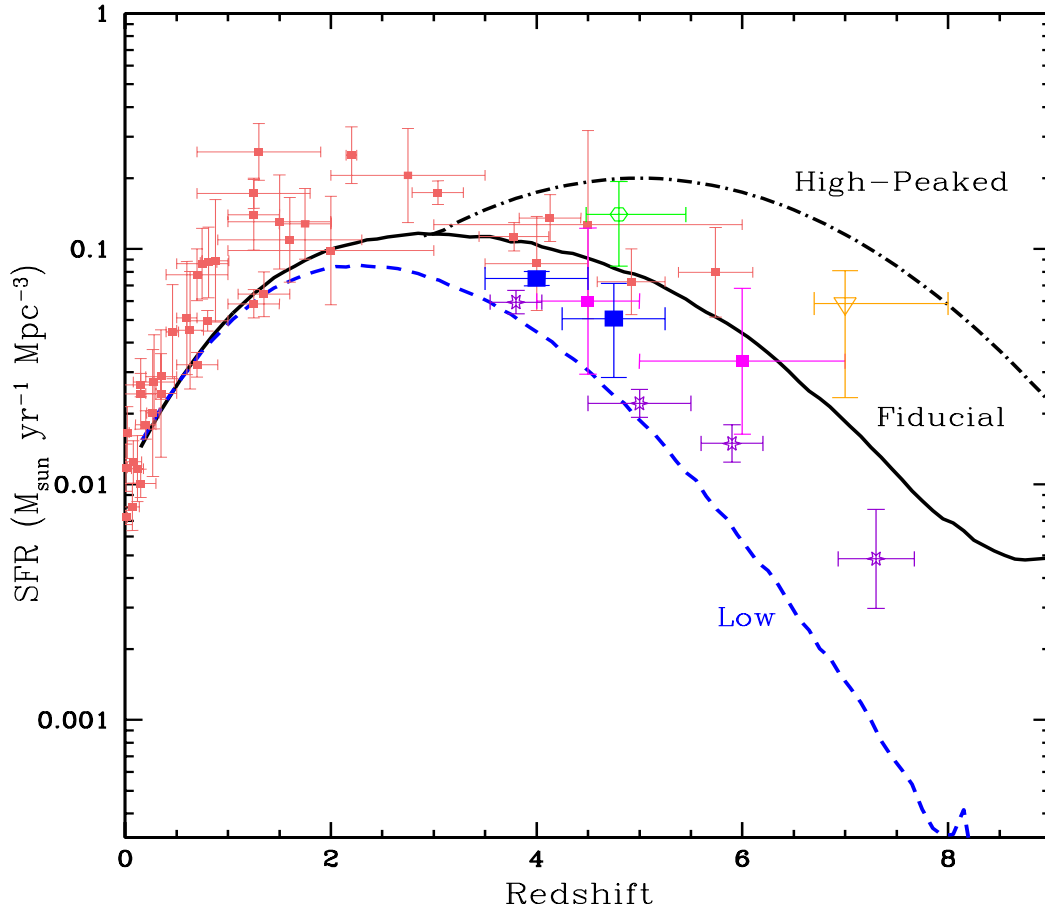


Figure 5.5: The global star formation rate density predicted by our models, compared with a compilation of observational data. The solid black and dashed blue curves show the SFRD history of our fiducial and low models, respectively. The black dash-dot curve which diverges from the fiducial curve above redshift three is the ‘high-peaked’ form which we discuss in the text. The red squares at lower redshift are from the compilation of Hopkins (2004). The purple stars are from observations by Bouwens et al. (2008, 2007) of dropout-selected galaxies. For these we show the dust-corrected results from integrating the luminosity functions down to a value of  $0.04 L_*$  at  $z = 3$ ; it is possible that fainter objects provide an additional contribution. The magenta squares at redshift 4.5 and 6 show inferred star formation rates from gamma-ray burst observations (Yüksel et al., 2008). The green circle is based on observations of Lyman-break galaxies at  $z \sim 5$  (Verma et al., 2007), and the orange triangle is an upper limit from VLT data (Mannucci et al., 2007). The blue squares are results from the Subaru Deep Field (Ouchi et al., 2004). All data have been corrected for extinction (by the authors) and converted to a Chabrier IMF.

defined here as having column densities  $> 10^{17.2} \text{ cm}^{-2}$ . This has a strong effect on the spectrum and intensity of the average background field. The propagation of ionizing flux through the IGM in our models is calculated using an updated version of the CUBA code. An earlier version of CUBA is described in Haardt & Madau (2001) and is based on the theory of Haardt & Madau (1996). Here we briefly summarize some of the main ideas and formalism from these papers.

The effect of residual neutral gas on the ionizing radiation field can be described in general terms by the radiative transfer equation:

$$\left(\frac{\partial}{\partial t} - \nu \frac{\dot{a}}{a} \frac{\partial}{\partial \nu}\right) J = -3 \frac{\dot{a}}{a} J - c \kappa J + \frac{c}{4\pi} \epsilon. \quad (5.1)$$

Here  $J(\nu)$  is the intensity of the radiation field for frequency  $\nu$ ,  $\epsilon(\nu)$  is the emissivity,  $a$  is the cosmological scale factor,  $c$  is the speed of light, and  $\kappa$  is the continuum absorption coefficient. This equation accounts for both the redshifting of photons to lower energies, and absorption by neutral gas. Quasars and star-forming galaxies contribute to  $\epsilon(\nu)$  in our model, along with the diffuse reemission of absorption systems. Lyman absorbers are taken to have a distribution that can be described in terms of power laws in column density and redshift

$$\frac{\partial^2 N}{\partial N_{HI} \partial z} \propto N_{HI}^{-1.5} (1+z)^\gamma \quad (5.2)$$

with parameters

$$\gamma = 0.16 \text{ (LAC, } 0 < z < 1.4)$$

$$\gamma = 3.0 \text{ (LAC, } 1.4 < z)$$

$$\gamma = 1.5 \text{ (LLS, all redshifts)}$$

used in these models. A distribution with slope -1.5 in column density has been shown to describe absorbers over a wide range in  $N_{HI}$  (Hu et al., 1995), and the slopes for redshift evolution are based on observational determinations (Kim et al., 1997; Stengler-Larrea et al., 1995; Bechtold, 1994). The effective optical depth from the Ly $\alpha$  forest absorption in this distribution is shown in Figure 5.6. Note that our Ly $\alpha$  optical depth does not follow the upturn seen at  $z \sim 6$ , where a rapid rise in absorption may signal that our assumption of a uniform UV background is no longer valid.

It should be noted that the exact form of the column distribution function is not critical, as it is the integrated value of this parameter from which we derive the effective optical depth and therefore the average background. The effective depth is dominated by clouds with opacity near unity. Using a power-law form simplifies the integration process, and speeds up our computation with little loss in accuracy. We do caution readers that the choice of distribution function can have a large effect on He II absorption, and in turn on the background above 54.4 eV which we report in Figure 5.10. The background at these energies is not expected to affect our gamma-ray attenuation significantly because the photon density at these high energies is so low.

Lyman systems reradiate a fraction of the absorbed light via recombination radiation. Our code accounts for the contribution of H I recombinations to the UV flux via free-bound, Ly $\alpha$ , and two-photon continuum emission. For the latter two, only the non-ionizing background is affected. The total proper volume emissivity from IGM

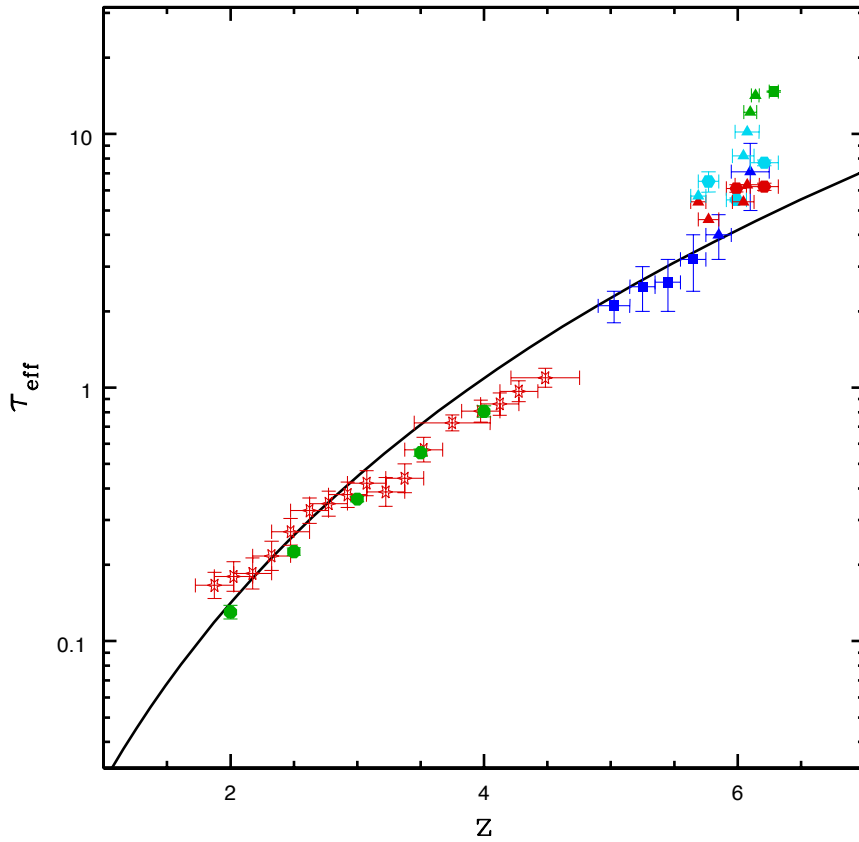


Figure 5.6: Effective optical depth as a function of redshift from our assumed absorption cloud distribution. Data from quasar spectra are shown at ( $5 < z < 6.5$ ) from Fan et al. (2006); here the blue points are averaged Gunn-Peterson measurements, and the red, cyan, and green symbols are  $\text{Ly}\alpha$ ,  $\beta$ , and  $\gamma$  measurements of the highest-redshift individual objects. Values at lower redshifts are from Schaye et al. (2003) (green circles) and Dall'Aglio et al. (2008) (red stars).

clouds from radiation released for a particular mode can be quantified as

$$\epsilon(\nu, z) = h\nu f_i(\nu) W_{abs}(z) \Xi(z, \nu) \frac{\alpha_i}{\alpha_{tot}} \frac{dz}{dl} \quad (5.3)$$

where  $\alpha_i$  is the fraction of recombinations leading to the particular mode, which has probability  $f_i(\nu)$  of creating a photon of energy  $\nu$ . In the case of Lyman- $\alpha$  emission this is simply a delta function at the line energy, and for the continuum distributions descriptions can be found in Osterbrock (1989). The remaining functions contain the details of emission and absorption from absorption systems

$$W_{abs}(z) = \int_{\nu_{th}}^{\infty} \frac{4\pi J(\nu', z)}{h\nu'} w_{abs}(\nu') d\nu' \quad (5.4)$$

$$\Xi(z, \nu) = \int_0^{\infty} \frac{\partial^2 N}{\partial N_{HI} \partial z} p_{em}(\nu, N_{HI}) dN_{HI}. \quad (5.5)$$

The first of these quantities is the rate of ionizations by the background field  $J(\nu', z)$ . Here  $w_{abs}(\nu')$  encodes the information about the optical depth for photons of a given energy, and thus the probability of being absorbed. Equation 5.5 is the integral over absorption systems, multiplied by  $p_{em}(\nu, N_{HI})$ , which is the probability of a photon of given energy escaping from a cloud after emission. The code does not include the contribution from sawtooth modulation due to H I and He II Lyman resonances (Madau & Haardt, 2009).

We do not include radiation from recombinations to He I, as neutral helium is small in number density compared to both H I and He II (though that may not be the case at redshifts on the verge of reionization). As shown in Haardt & Madau (1996),

thermal collisional effects can provide a sizable fraction (20 to 30 %) of the H I emission by Ly $\alpha$  and two-photon processes; these are not accounted for in our code. Collisions between He II atoms are never significant, as there is insufficient thermal energy to excite these modes.

#### 5.2.4 Ionizing Escape Fraction from Galaxies

The fraction of ionizing photons produced that escape from galaxies into the IGM is a free parameter in our model. This parameter is poorly constrained, with observations and simulations giving widely different and sometimes conflicting results. In the literature, the escape fraction may be defined in a couple ways. The absolute escape fraction is simply the fraction of radiation at wavelengths just shortward of 912 Å which escapes the dust and neutral hydrogen in a galaxy. This definition is most relevant for the purposes of modeling the ionizing background. What is actually measured in observations is the relative escape fraction, where the ionizing flux is compared to a non-ionizing wavelength, often 1500 Å. As described below, we use a relative definition which separates the amounts of attenuation due to dust and H I (Equation 5.6). Ionizing radiation from quasars is not attenuated in escaping the host galaxy.

Direct detection of escaping UV radiation has only been successful in a handful of individual cases. As two of these detections have been for galaxies at  $z \sim 3$  with large escape fractions measured (Shapley et al., 2006), the fact that many low redshift attempts to find ionizing radiation have failed with low upper bounds may suggest evolution in this quantity between redshifts one and three. Rather firm upper limits

on escape fraction from direct detection efforts exist for lower redshift galaxies (see the compilation in Siana et al. 2007). Steidel et al. (2001) reported ionizing flux from 29 stacked galaxies at  $z \sim 3.4$ , at a level indicating little or no attenuation. However, this result suffered from a selection bias, as the Lyman–break galaxies used were chosen from the bluest quartile of the population.

While observations have mainly determined upper limits on the ionizing escape fractions, some authors have used the ionization state of the IGM to derive lower limits. Ionization rates inferred from Ly $\alpha$  forest data and reasonable extrapolations of source number to faint luminosity can require a high escape fraction. Values of  $\gtrsim 20\%$  above redshift 5 were found to be needed in Bolton & Haehnelt (2007). Srbinovsky & Wyithe (2008) have found that constraints on the escape fraction from  $5.5 < z < 6.0$  from N-body simulations require a global minimum of 5% to match Ly $\alpha$  data, with a higher fraction needed in the event that star formation in galaxies in smaller halos is suppressed.

Recently, detailed adaptive mesh refinement N-body hydrodynamical simulations of high-redshift galaxies ( $3 < z < 9$ ) by Gnedin, Kravtsov, & Chen (2008) have found low escape fractions of 1–3%, without strong evolution in redshift or dependence on galaxy properties. This work found that most escaping ionizing radiation originated from stars in a thin shell at the outside of the H I disk. Smaller galaxies have less escaping radiation due to the fact that their H I disks are thicker relative to the distribution of young stars. Dust is found to have little effect on the escape of Lyman-continuum radiation, as the unobscured minority of stars that provide most of the escaping ionizing radiation have essentially no attenuation due to dust, while stars that have translucent

( $\tau \sim 1$ ) optical depths due to dust are generally completely obscured by HI. Another analysis has been undertaken using a smoothed particle hydrodynamics code by Razoumov & Sommer-Larsen (2007, 2006) and has found evolving escape fractions, with  $f_{esc} = 6$  to 10 % at  $z = 3.6$  decreasing to 1 to 2 % at  $z = 2.4$ . This simulation did not include the effects of dust.

Our semi-analytic models predict the emissivity from star-forming galaxies down to a minimum rest-frame wavelength of 100 Å. Lyman-continuum photons are attenuated by a factor  $f_{esc,HI}$ ; this determines the absorption of photons shortward of 912 Å and is a non-evolving input to our radiative transfer code. This parameter is defined as the following ratio of intrinsic and observable luminosities at 912 and 1500 Å

$$f_{esc,HI} = \frac{(L_{912}/L_{1500})_{\text{escaping}}}{(L_{912}/L_{1500})_{\text{intrinsic}}} = f_{esc} f_{1500}^{-1} \quad (5.6)$$

where  $f_{esc}$  is the absolute attenuation factor from both dust and H I for ionizing photons near the Lyman limit, and  $f_{1500}$  is the factor from dust alone at 1500 Å. As dust absorption is an evolving effect included in the semi-analytic model, total absorption  $f_{esc}$  for ionizing photons escaping from galaxies must be interpreted as the product of  $f_{esc,HI}$  and the average  $f_{1500}$  for a particular redshift in the model. The average value of  $f_{1500}$  in our model is higher at high redshift, and is higher in the low model than in the fiducial model at high redshift. Typical values of  $f_{1500}^{-1}$ , as seen in the difference between attenuated and unattenuated curves in Figure 5.1, vary from about 6.8 at  $z = 2$  to 11.2 at  $z = 5$  for our fiducial model, and 9.7 to 14.2 in the low model. As noted in Gnedin et al. (2008), taking the total absorption to be a product of the dust and H I factors

may not be physically realistic, as the two components are may not be distributed in the same way within the galaxy, however it is sufficient for the purpose of calculating emissivities, as we are dealing only with global quantities.

### 5.2.5 Quasar Emissivity

Quasar input to our model is accomplished using an assumed UV luminosity density, which determines the output at all energies via a fixed spectral form. We have used the quasar luminosity functions at  $912 \text{ \AA}$  determined by Hopkins, Richards, & Hernquist (2007, HRH07) which are based on a large observational data set and spectral and obscurational modeling. This work found that, with the appropriate corrections for obscuration, a single bolometric function could match data in each band. Both the bright- and faint-end slopes of the LF are argued to become more shallow at higher redshift, indicating a increasing contribution from bright, unobscured AGN, which dominate the total AGN luminosity above redshift  $\sim 2$ .

Another approach to modeling the quasar contribution to the background was presented in Schirber & Bullock (2003, SB03). This work estimated the evolution of the unobserved faint-end of the quasar luminosity function at high redshift using observational constraints on the ionizing background. They found very different results depending on whether they used constraints on the ionizing background from the quasar proximity effect or from the Lyman- $\alpha$  flux decrement method. Assuming the broken power law universal quasar spectrum we present below, the HRH07 luminosity density evolution at  $912 \text{ \AA}$  is similar to Model ‘A’ of SB03, which produced the lowest fluxes

and was found to be consistent with the flux decrement data when combined with a substantial contribution from star-forming galaxies. The highest derived flux, arising in Model ‘C’, was sufficient to produce ionizing photons at the level suggested by proximity effect measurements. While we recognize that it is probable that many of these proximity effect measurements overestimate the background due to aforementioned biases, we will use the SB03 Model ‘C’ for the purposes of creating and analyzing an extremely quasar-dominated background model.

Luminosity densities at the H I and He II Lyman limits for each of these models are shown in Figure 5.7. We have renormalized the original model proposed by SB03 by a factor of 0.8 to better match the HRH07 results below redshift 2.3.

Quasars are assumed to have a spectrum which can be modeled as a broken power law in  $F_\nu = dF/d\nu$ . In the extreme-UV, we have adopted the hard spectrum suggested by Telfer et al. (2002), from observations with the Faint Object Spectrograph on HST of quasars at a wide variety of non-local redshifts ( $z > 0.33$ ). The values we assume are as follows

$$F_\nu \propto \nu^{-\alpha} \tag{5.7}$$

with indices

$$\alpha = 0.4 \quad (12\mu\text{m} < \lambda)$$

$$\alpha = 1.3 \quad (1\mu\text{m} < \lambda < 12\mu\text{m})$$

$$\alpha = 0.2 \quad (500\text{nm} < \lambda < 1\mu\text{m})$$

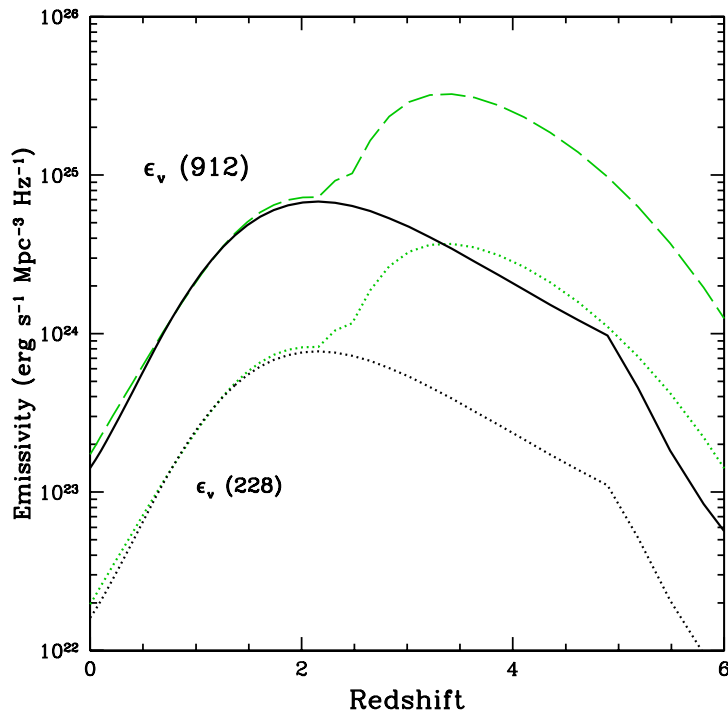


Figure 5.7: Quasar luminosity density for the Hopkins et al. (2007) (solid black) and Schirber & Bullock (2003) Model ‘C’ (broken green) models at 912 (upper lines) and 228 Å (lower lines). The latter has been multiplied by a factor of 0.8 to better match the observations at low redshift.

$$\alpha = 0.5 \quad (120\text{nm} < \lambda < 500\text{nm})$$

$$\alpha = 1.57 \quad (\lambda < 120\text{nm})$$

$$\alpha = 0.9 \quad (\text{Soft X-rays, } > 500 \text{ eV})$$

The contribution of quasars to the background is only non-negligible in the extreme-UV ( $\lambda < 120\text{nm}$ ). At other wavelengths we use slopes to roughly fit typical x-ray spectra of Seyfert 1 galaxies, and the optical and IR emission of quasars seen in SDSS and other observations (Vanden Berk et al., 2001; Sanders et al., 1989).

### 5.3 Cosmological Models and Resulting UV Background

To calculate the evolving background radiation field, we have combined three estimates of the star-formation rate density with two possible forms for the quasar luminosity density. The two quasar models are the ‘realistic’ estimate of Hopkins et al. (2007) from a large body of observational data, and a higher ‘extreme’ model motivated by proximity effect measurements for  $3 < z < 5$  from SB03. Our four models are summarized in Table 5.1.

#### 5.3.1 Ly $\alpha$ Forest Constraints

Inferred ionization rates and column density measurements from the Ly $\alpha$  forests of quasar spectra provide us with an independent measurement of the UV background through its ionizing properties, which we can compare with the IGM state computed by our radiative transfer code. In Figure 5.8, we compare the ionization rate (in

Table 5.1: The background models considered in this work. The second and third columns show the star-formation histories and quasar luminosity densities used as inputs in each model. The escape fraction in the last column refers to the values used in calculating the background flux and optical depth to gamma rays in Figs. 5.10 and 5.11, respectively. Our star formation history scenarios are discussed at the beginning of this section. ‘HRH07’ refers to the best-fit model of Hopkins et al. (2007), and ‘SB03 Model C’ to the model in Schirber & Bullock (2003). We have multiplied the latter by a factor of 0.8 to better match the observed quasar luminosity density at low redshift. The escape fraction refers to the attenuation of ionizing photons from star-forming galaxies by neutral hydrogen; attenuation by dust is included intrinsically in our semi-analytic model.

Model	SFR Density	Quasar Luminosity	$f_{\text{esc,HI}}$
1	Fiducial	HRH07	0.1
2	Low	HRH07	0.2
3	Fid. High-peaked	HRH07	0.1
4	Fiducial	SB03 Model C	0.02

terms of  $\Gamma_{-12}$ , the average rate per hydrogen ion with units of  $10^{-12} \text{ s}^{-1}$ ) with data from both the quasar proximity effect and the flux decrement in Ly $\alpha$  forest measurements. As discussed in the Introduction, these two techniques have tended to give disparate values for  $\Gamma_{-12}$ . For the fiducial and low models with the HRH07 QSO LF, we show ionization rates with several values for the escape fraction of ionizing radiation from the galactic H I disk. With a moderate H I escape fraction of 0.1 to 0.2, our fiducial model is able to reproduce the level of ionizing background detected by most determinations using flux decrement techniques. Including attenuation by dust, this corresponds to a total ionizing escape fraction of  $\sim 1$  to 3 per cent, consistent with upper limits from observations as well as values suggested by simulations (Gnedin et al., 2008; Razoumov & Sommer-Larsen, 2007). With the low model, a higher H I escape fraction of  $\sim 0.5$  is necessary to match the highest redshift points ( $z > 5$ ), due to the rapidly declining star-formation rate at high redshift. This escape fraction is higher than suggested by some

authors, but there are no direct constraints on escape fractions at such high redshifts.

Based on the quality of fits for our different models to these flux decrement data, we have chosen escape fractions of 0.1 and 0.2 for our fiducial and low models, respectively, as reasonable values to use in calculating the background and pair-production opacity. Both of these models predict ionization rates which decline above redshift 2.5; this is due both to the shape of the star-formation history and the increasing opacity of the IGM with redshift.

The flux decrement calculations from the largest quasar samples, Faucher-Giguère et al. (2008b) and Bolton et al. (2005), find ionization rates that are essentially flat from  $z = 2$  out to  $z = 4$ , albeit with differing normalizations. Our model predictions are reasonably consistent with these observational estimates, considering the uncertainties involved. The high-peaked model better reproduces the flatness of the ionization rate from  $z \sim 3 - 4$ , but still predicts too steep a rise from  $z \sim 2 - 3$ . The SF history predicted by our fiducial model could be made perfectly consistent with the Faucher-Giguère et al. (2008) data by assuming an escape fraction that evolves from  $\sim 0.2$  at  $z \sim 4$  to 0.02 at  $z \sim 2$ .

The final scenario we examine uses the higher quasar emissivities of Model ‘C’ in Schirber & Bullock (2003). As the ionizing contribution from star-formation is subdominant at all intermediate redshifts in this case, we have assumed a low escape fraction of 0.02. The ionizing flux in this model is capable of reproducing the highest measurements from the proximity effect. We have already mentioned several known biases which may have artificially elevated these values, and this model should

be considered an extreme possibility.

Another Ly $\alpha$  forest measurement which can provide insight into the UV background is the relative abundance of H I and He II present in the IGM. This may be presented in terms of relative column densities  $N(\text{HeII})/N(\text{HI})$ , or analogously as inverse ionization rates for these components  $\Gamma_{\text{HI}}/\Gamma_{\text{HeII}}$ ; this is often referred to as the UV softness parameter. In Figure 5.9 we show how softness evolves with redshift for each of our background models. Our low, fiducial, and high-peaked star-formation densities with the HRH07 QSO LF are able to provide a reasonable match to observations when a moderate escape fraction is assumed. High escape fractions  $\geq 0.5$ , which are required for the ‘low’ SFR model to match ionization rates at high redshift, tend to overpredict softness. Our quasar-dominated model (SB03 model C) does not reproduce the trend of increasing softness in the background field with redshift, another factor which disfavors such a dominant contribution from faint quasars. The column density ratio in this case is not found to be sensitive to the H I escape fraction.

### 5.3.2 The Background Flux

The key result of this chapter is a prediction of the evolving UV background out to redshift  $z \sim 9$ , which has been calculated from our models for the total (stellar + quasar) emissivity  $\epsilon(\nu, z)$  combined with a calculation of the absorption and re-emission by IGM radiative transfer processes. At wavelengths well above the Lyman limit, the background at a redshift  $z_0$  is therefore determined by total history of emission at higher redshifts  $z > z_0$ . At ionizing wavelengths, the mean free path of photons is shorter than

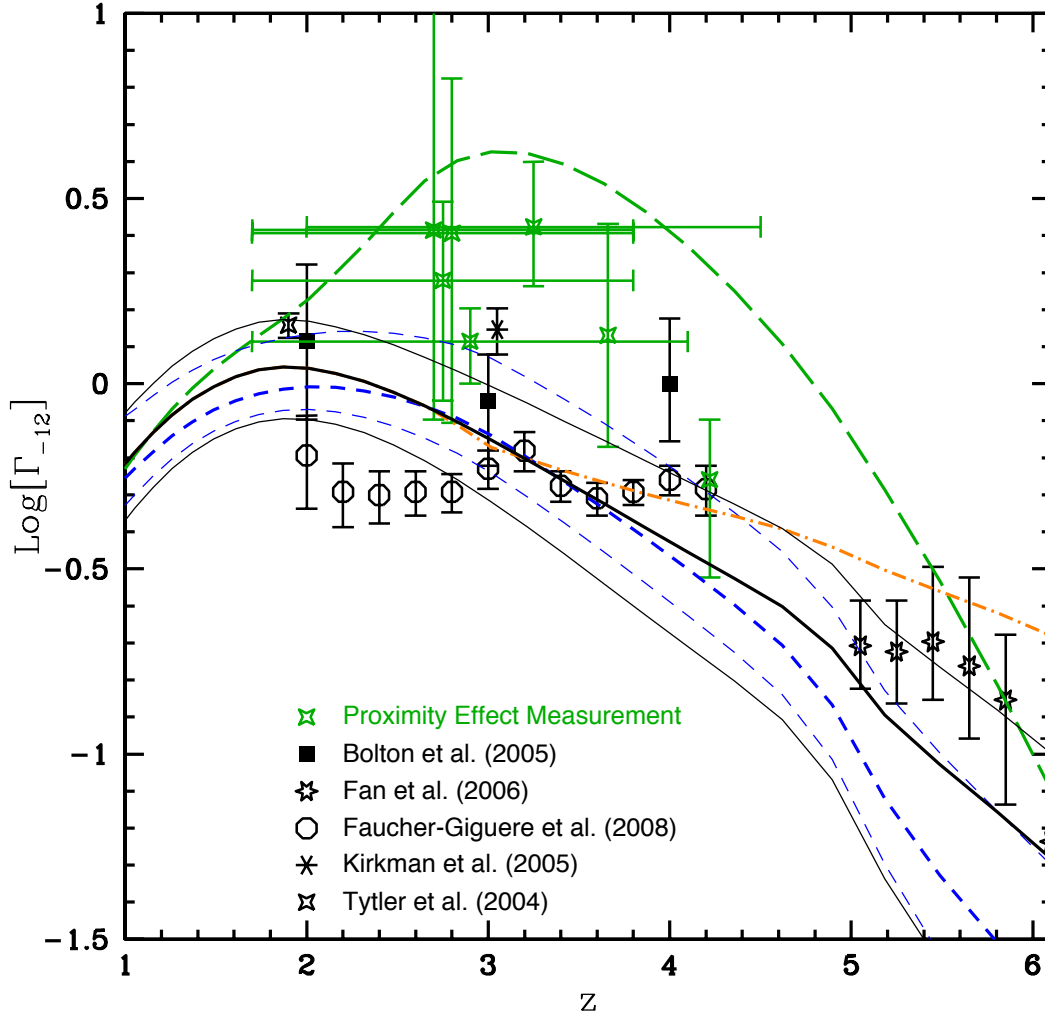


Figure 5.8: Ionization rate per hydrogen atom (with units of  $10^{-12} \text{ s}^{-1}$ ) in our four scenarios compared with data at a range of redshifts. Black solid lines: fiducial model with H I escape fractions from star-forming galaxies of 0.02, 0.1, and 0.2 (bottom to top). Dashed blue lines: low star-formation model, with escape fractions 0.1, 0.2, and 0.5. Orange dash-dotted line: high-peaked star formation rate with escape fraction 0.1. These aforementioned models all use the quasar emissivity of HRH07. The long-dashed green line shows the fiducial SFR model with quasar model C of Schirber & Bullock (2003), and escape fraction 0.02. Data points are divided into those obtained from flux-decrement analysis (black) and those obtained via proximity effect near quasars (green). References for the former are Bolton et al. (2005); Fan et al. (2006); Faucher-Giguère et al. (2008b); Kirkman et al. (2005); Tytler et al. (2004), and the latter include Scott et al. (2000); Cooke, Espey, & Carswell (1997); Giallongo, Fontana, & Madau (1997); Cristiani et al. (1995); Williger et al. (1994); Lu, Wolfe, & Turnshek (1991); Bajtlik, Duncan, & Ostriker (1988). Some points have been shifted slightly for readability.

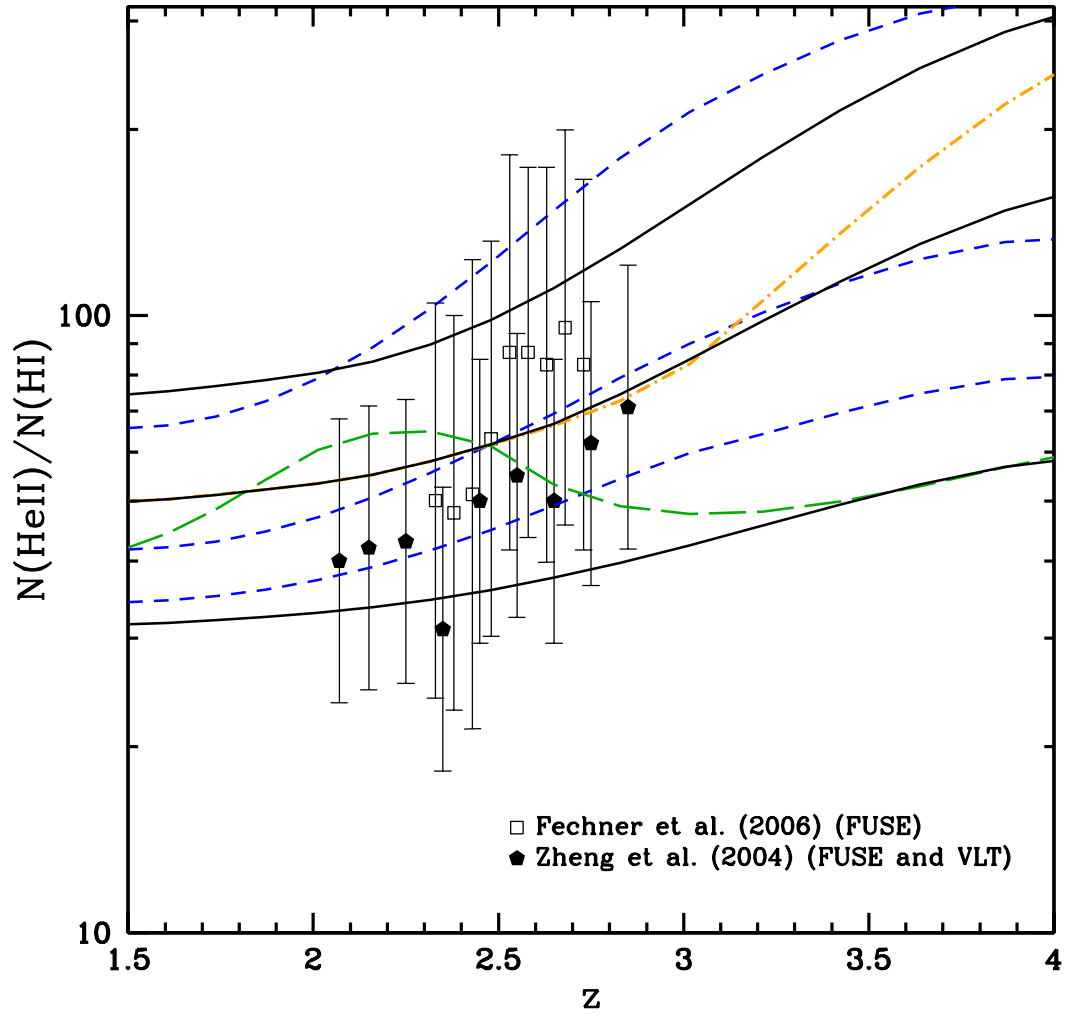


Figure 5.9: The ratio of He II to H I column densities plotted against redshift. Higher values indicate a softer ionizing background, with comparatively more ionizing photons available per hydrogen atom. Line types in this plot are the same as in Figure 5.8. Data are from observations of He II Ly $\alpha$  systems by Zheng et al. (2004) and Fechner et al. (2006).

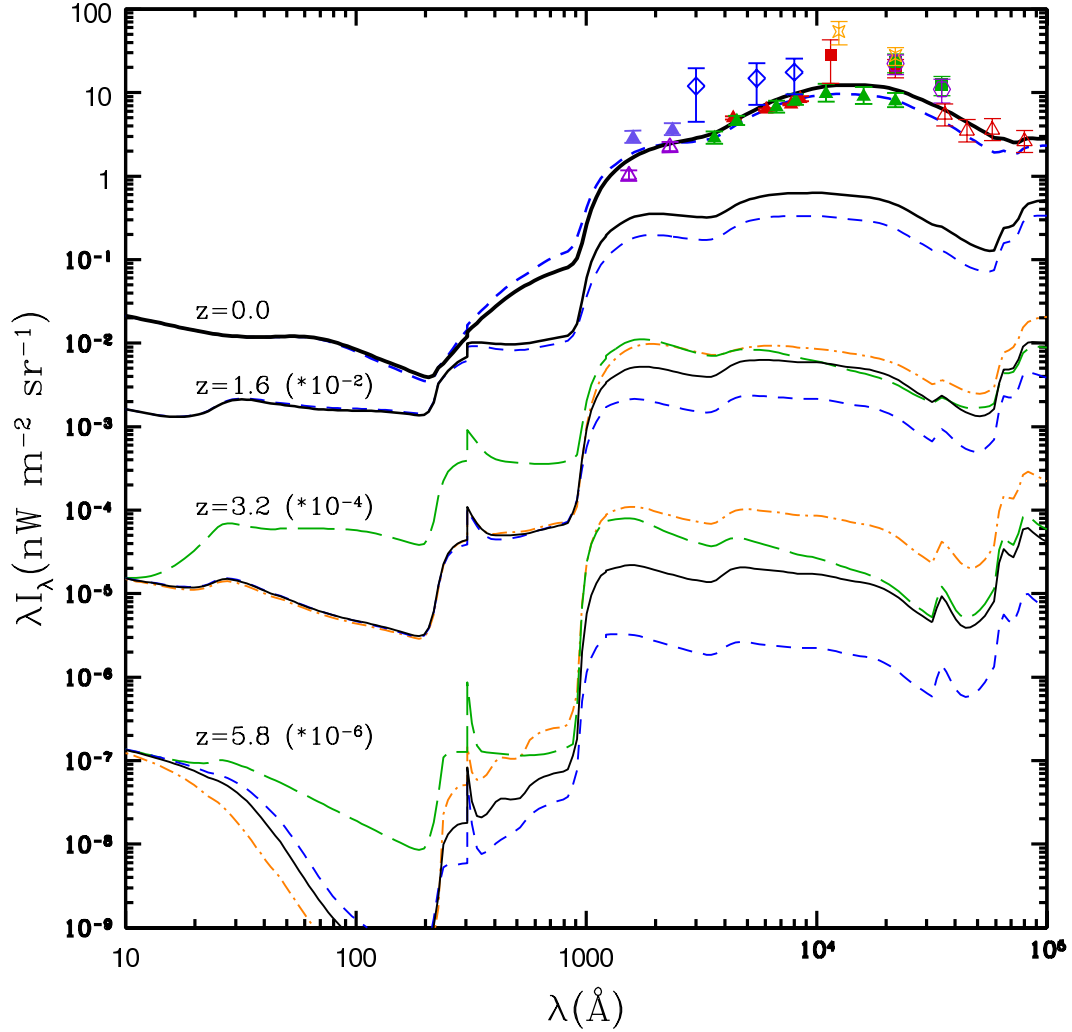


Figure 5.10: The history of the background flux, shown at the present day and three other redshifts. Intensities at the nonzero redshifts have been multiplied by the indicated factors ( $10^{-2}$ ,  $10^{-4}$ , and  $10^{-6}$  at  $z = 1.6$ ,  $3.2$ ,  $5.8$ , respectively) to separate the lines. Black solid line: fiducial model with H I escape fraction of 0.1. Dashed blue line: low star-formation model, with escape fraction 0.2. Orange dash-dotted line: high-peaked star formation rate with escape fraction 0.1. Green long-dashed: fiducial model with SB03 quasar contribution and escape fraction 0.02. At low redshift, only the first two models are shown, as the other models do not produce discernibly different levels of background at these times. We have also shown observational measurements of the background flux at  $z = 0$  in the UV, optical, and near-IR from Figure 3.9.

cosmological distances due to residual neutral hydrogen in the IGM at redshifts greater than the breakthrough redshift, and therefore the ionizing background at  $z_0 > z_{br}$  is determined by the emissivity of approximately contemporary sources.

In Figure 5.10 we show the background flux for our four models at several redshifts, including  $z = 0$  where we have also shown a compilation of observable data, including estimates from both absolute photometry and discrete source number counts. In each case, we assume the ‘best-fit’ escape fractions of Table 5.1, which we have chosen based on the comparisons with Ly $\alpha$  forest measurements. At all redshifts, the background shows a sharp drop at the Lyman edge; this is a combined consequence of absorption in stellar atmospheres, H I in galaxies (quantified as  $f_{\text{esc,H I}}$  in our models), and IGM reprocessing. The feature at  $\sim 300 \text{ \AA}$  is due to He II Ly $\alpha$ .

## 5.4 Gamma-ray Attenuation

For each of our four models, we have calculated the optical depth of gamma rays at all relevant energies and redshifts; see Section 4.2 for a review of this phenomenon. As in our calculation of the background flux above, we assume the H I escape fractions listed in Table 5.1. It should be emphasized that the choice of escape fraction has little effect on absorption of gamma rays at energies  $> 10 \text{ GeV}$ . We find, as argued in Oh (2001), that the background field at energies above 13.6 eV is negligible as a barrier to cosmological gamma rays, and that significant optical depth above this energy is due to photons longward of the Lyman limit, where photon density increases dramatically in all

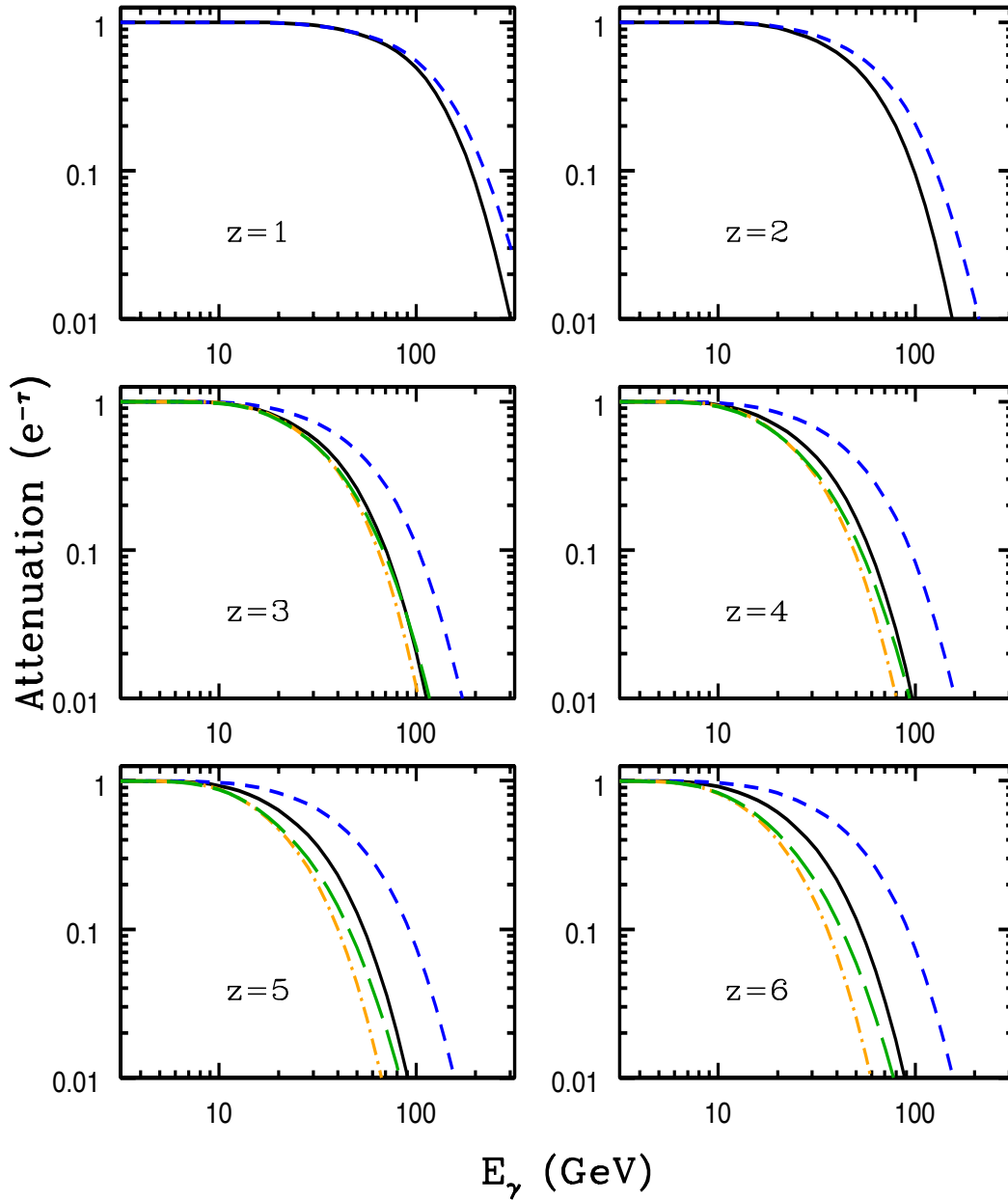


Figure 5.11: Attenuation factors ( $e^{-\tau}$ ) as a function of gamma-ray energy for the indicated source redshifts. Curves are as in Figure 5.10, and indicate the absorption resulting from our models of star-formation and quasar emissivity. Black solid line: fiducial model with H I escape fraction of 0.1. Dashed blue line: low star-formation model, with escape fraction 0.2. Orange dash-dotted line: high-peaked star formation rate with escape fraction 0.1. Green long-dashed: fiducial model with SB03 quasar contribution and escape fraction 0.02. Curves for the high-peaked star formation and high quasar models converge to the fiducial model for  $z \leq 2$ .

of our models. While gamma rays are limited to interactions with background photons of an absolute minimum energy  $E_{th} = m_e^2 c^4 / E_\gamma$  (with  $\cos\theta = -1$ ), redshifting places these gamma rays at higher energies at earlier epochs, where they can pair produce on the non-ionizing background. The increase of star-formation rate density by roughly an order of magnitude between present-day and peak rates means that gamma rays from high-redshift sources will tend to be attenuated most strongly at these early redshifts, where they have energies  $(1+z)$  times higher than at  $z = 0$ .

In Figure 5.11, the optical depth vs gamma-ray energy is shown for each model at various redshifts. These high-redshift results should be considered complementary to our other calculations of EBL with these semi-analytic models, which emphasized the absorption of  $> 100$  GeV gamma rays at lower redshift. The effect of the UV background is to produce a relatively sharp and featureless cutoff in energy. At energies above 100 GeV, the effect of the EBL has often been quantified as a change in the spectral index of observed blazar spectra (e.g. Aharonian et al., 2006), due to the relatively flat number density of EBL photons in the near and mid-IR. At lower energies, this approximation is not valid over any significant range in energy, due to the steepness of the cutoff that results in rapidly increasing numbers of photons with increasing wavelength in the UV.

Our high-peaked SFRD and quasar-dominated models give absorption features that are similar, despite being very different in terms of the spectral form of the background flux. While the emission from quasars produces a much higher ionizing background, the spectral cutoff at all redshifts we have explored is dominated by the photons longward of the Lyman limit.

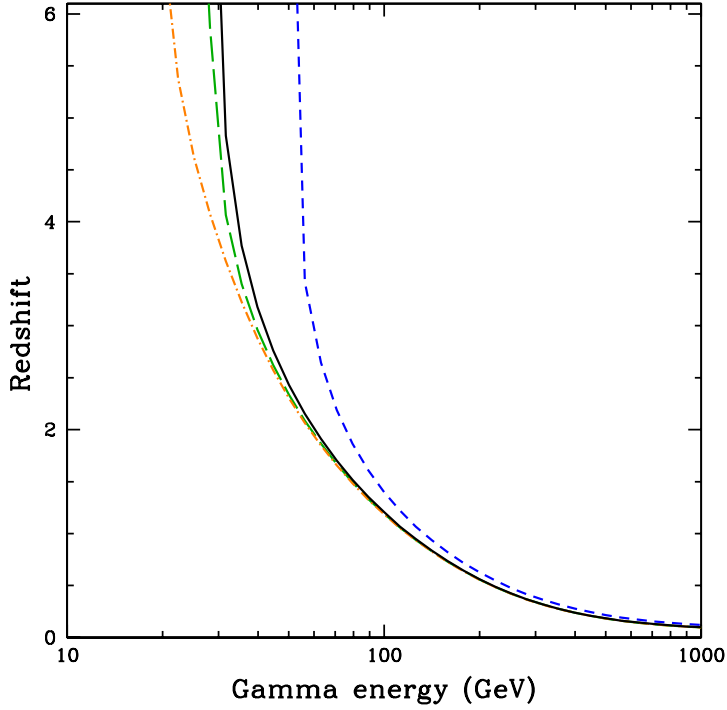


Figure 5.12: The redshifts at which the universe becomes optically thick ( $\tau > 1$ ) to gamma rays at a given energy. Line types and colors are as in Figure 5.11.

In Figure 5.12, we show the redshifts at which the universe becomes optically thick ( $\tau > 1$ ) for gamma rays of a given energy for each of our models. From this plot, we can see in a general sense how background attenuation affects different energy regimes at different redshifts. The low model shows little change at redshifts higher than about 3, due to the rapid decline in star formation after this point. The high-peaked model has the most impact at high redshift, and produces absorption features that evolve out to  $z > 6$ .

## 5.5 Discussion

We have created and analysed predictions for the UV background that are intended to broadly span the possibilities in star-formation rate and quasar-luminosity density. The degree to which each model is able to reproduce various observational findings is qualitatively summarized in Table 5.2. Our fiducial model with the HRH07 QSO LF (first entry in Table 5.1) provides a reasonable match to the level of ionizing flux inferred from Ly $\alpha$  forest measurements when an H I escape fraction of 0.1 is assumed; this corresponds to a total  $f_{\text{esc}}$  of 1 to 1.5 % when combined with the dust absorption values predicted by our semi-analytic galaxy formation model. The ‘low’ model for the SFR density, with the lower CDM power spectrum normalization of WMAP3, requires a larger escape fraction to match ionization rate data, especially the higher redshift points  $z > 5$ , where  $f_{\text{esc,HI}} \sim 0.5$  is required. The low model is also found to underpredict the high redshift UV luminosity density. This may indicate that this model does not have enough star formation at early times, or that the UV dust extinction factors are too high. Both of these models fail reproduce the nearly constant ionization rate between  $2 < z < 4.5$  seen in some flux decrement analyses. The high-peaked model, which has a star-formation rate that increases until redshift 5, does produce a somewhat flatter ionization rate, as suggested by Faucher-Giguère et al. (2008a). The large amount of high-redshift star-formation in this model is not supported by estimates of stellar mass buildup, and should be considered a somewhat extreme scenario. Another mechanism for producing a flatter ionization rate history is an evolving escape fraction that increases

with redshift, a possibility that we do not explore here but which has been seen in some simulations (Razoumov & Sommer-Larsen, 2007, 2006), and as already mentioned may be suggested by observations which have detected Lyman continuum radiation from distant ( $z \sim 3$ ) galaxies (Shapley et al., 2006), but not closer sources (Siana et al., 2007). This would have only a weak effect on the opacities we have calculated, as most attenuation of gamma rays is due to the non-ionizing UV background, which would have a much larger number density than the ionizing background even for a high escape fraction.

Table 5.2: Here we summarize a broad set of models, and the qualitative level of agreement of each with Ly $\alpha$  forest data, proximity effect measurements, and simulations of total ionizing escape fraction from star-forming galaxies. The numbers of the models shown in Figs. 5.10 and 5.11 are in bold.

Parameters			Fits with Data				
Model	SFR Density	QSO Emissivity $f_{escHI}$	Flux Decrement <sup>a</sup>	Proximity Effect <sup>b</sup>	Softness <sup>c</sup>	$f_{esc}$ <sup>d</sup>	
1.1	Fiducial	HRH07	0.02	x	x	o	✓
<b>1.2</b>	Fiducial	HRH07	0.10	o	x	✓	✓
1.3	Fiducial	HRH07	0.20	o	x	o	✓
2.1	Low	HRH07	0.10	x	x	o	✓
<b>2.2</b>	Low	HRH07	0.20	o	x	✓	✓
2.3	Low	HRH07	0.50	o	x	o	o
<b>3</b>	Fiducial High-peaked	HRH07	0.10	✓	x	✓	✓
<b>4</b>	Fiducial	SB03 Model C	0.02	x	✓	x	✓

✓ – best agreement

o – marginal agreement

x – poor agreement

<sup>a</sup> This refers to the relatively flat ionization rate for H I at a level seen in the quasar spectra data of Bolton et al. (2005) and Faucher-Giguère et al. (2008b) (Fig. 5.8).

<sup>b</sup> The higher levels of ionization rate determined in uncorrected proximity effect measurements (Fig. 5.8).

<sup>c</sup> The softness  $\eta \equiv N(\text{HeII})/N(\text{HI})$ , from data compiled in Fig. 5.9.

<sup>d</sup> The total escape fraction; recall from Section 2 that this is equivalent to  $f_{esc,HI} * f_{1500}$ . In our semi-analytic models,  $f_{1500}^{-1}$  ranges from about 7 to 14 at the redshifts of interest.

Our results suggest that observations of sufficient numbers of high-energy gamma-ray sources out to high redshift could provide a probe of the UV background at these epochs that is independent of any other observational test. Pair-production with target background photons produces a spectral cutoff at energies that are dependent upon redshift and assumed cosmological model. With enough detections of blazars and/or gamma-ray bursts (GRBs) at different confirmed redshifts in the 10 to 100 GeV energy decade, it should be possible to detect an evolving cutoff in energy, and distinguish between the different background levels proposed in this work. The exact number of blazars that will be detected at GeV energies over the coming years is uncertain and dependent upon the poorly-understood emission processes and number density evolution of these sources. However, even conservative estimates indicate that a large number of sources will be detectable by the Fermi spacecraft. The EGRET experiment detected more than 60 high-confidence blazars at energies of  $> 100$  MeV out to redshift 2.28, mostly of the flat-spectrum radio quasar (FSRQ) type (Mukherjee et al., 1997). An extrapolation of these results suggests that Fermi will see  $\sim 1000$  blazars extending to higher redshift (Dermer, 2007). An analysis of two different realizations of the blazar luminosity function by Chen, Reyes, & Ritz (2004) suggested that Fermi could detect thousands of blazars, and would potentially be able to measure attenuation at distances as great as  $z = 5$ . The 3-month Fermi LAT survey has already reported 106 AGN sources at high confidence (Abdo, 2009). In addition to analyzing blazar spectra in survey and pointed observations, Fermi will also act as a finder for new and upcoming ground-based experiments such as H.E.S.S.-II and MAGIC-II which will be capable of

resolving most of the energy ranges of interest.

None of our models predicts significant attenuation at 10 GeV or below for any redshift. This is true even for our extremely quasar-dominated model, where the opacity of a 10 GeV observed gamma ray is never higher than  $\tau \sim 0.2$ . As the ionizing flux in this model is higher than allowed by most measurements of the Ly $\alpha$  forest, it is unlikely that any cosmological model could produce significant gamma-ray opacity due to a large contribution of ionizing photons to the background. The high-peaked star formation model produces the most absorption in the 10–100 GeV energy range for  $z > 3$ , but despite having a very high UV output only has a moderate impact on the calculated optical depths relative to the fiducial model.

### 5.5.1 Comparison With Other Work

It is useful to compare the absorption predicted by our models with the calculations of other authors who have used different methods, in the cases where their results include our energy and redshift regime of interest. In many instances, our predicted attenuation is less than what has been previously proposed.

The background model of Franceschini et al. (2008) is based upon extrapolated luminosity functions determined from a large compilation of multiwavelength data, including deep ACS imaging of distant galaxies, and treats separately the evolutionary histories of spiral, elliptical, and star-bursting galaxy populations. While their EBL agrees well with our fiducial model at  $z=0$  and  $z=1$ , their absorption  $\tau$  in the 10–100 GeV energy decade is at least a factor of two greater at  $z=2-4$  than any of our mod-

els. The most recent models of Stecker and collaborators (Stecker et al., 2006, 2007) are based on a ‘backwards evolution’ model in which galaxies’ emission SEDs are determined by their brightness in one band, taken to be  $60 \mu\text{m}$ . The luminosity of the galaxy population at this wavelength is assumed to brighten with redshift as a power law in  $(1+z)$ . One disadvantage of this method is that it attempts to describe luminosity evolution over several orders of magnitude in wavelength from a single power law, which cannot take into account the complexity of galaxy evolution. This model predicts a UV background considerably higher than our own (see Figure 4.7). Gamma-ray opacities in this work are much higher than our predictions, with the universe optically thick ( $\tau > 1$ ) to 10 GeV gamma rays above  $z \sim 3$ , and for  $> 25$  GeV above  $z = 1$ . This level of absorption holds very different implications for experiments such as Fermi. At high redshifts, absorption cutoff spectral features would be visible between about 5 and 20 GeV, with no signal from higher energies due to optical thickness from the background. The galaxy SEDs in these models have no emission above Lyman energies, and therefore all attenuation at these very low energies is the result of near-threshold interactions with non-ionizing UV photons. The redshift-dependent optical and UV SEDs used are based on the population synthesis models of Bruzual A. & Charlot (1993), which do not include UV dust extinction, and as we have seen may therefore overestimate the far-UV background by a factor of  $\sim 10$ .

The recent observation by Fermi of high-energy emission from GRB 080916C at  $z=4.35$  (Greiner et al., 2009a) provides a valuable first test of these predictions for GeV absorption. The highest energy photon seen by the LAT was 13.2 GeV, with

over 10 photons seen above 1 GeV (Abdo, 2009). In all of our models, the gamma-ray optical depth is much less than 1 for this energy and redshift, and similar values are found in the star-formation models of Razzaque et al. (2008). The models of Stecker and collaborators predict a much higher opacity,  $\tau = 3.5$  to 4.5, for the 13 GeV photon. While it is difficult to draw conclusions from a single event, more bursts seen with GeV emission equal or greater to GRB 080916C could strongly disfavor such a large background flux, and observations of slightly higher energy photons ( $E \sim 30$  GeV) from similar redshifts could provide a test of our models.

### 5.5.2 Caveats and Future Work

We expect our approach to be reasonably accurate at predicting the ionizing and non-ionizing background fields out to redshift  $\sim 6$ , where H I Gunn-Peterson troughs appear in observed quasar spectra (Fan et al., 2006). At higher redshifts, during the epoch of reionization, the concept of a uniform background for ionizing photons is no longer valid, as photons above the Lyman limit are confined to the vicinity of their sources. In our Lyman absorption model (Equation 5.2), the sudden increase seen in H I opacity at redshift six is not represented, and our model would therefore be expected to overproduce the ionizing background above this redshift. A similar limitation exists in our treatment of He opacities above the redshift of He reionization  $z \sim 3$ . However, these factors alone are unlikely to have a significant effect on calculated opacities.

We have made the assumption of a universal stellar IMF in this work, and have not included a separate population of metal-free (population-III) stars or other

early source types such as miniquasars (Madau et al., 2004). These types of unobserved sources could have very different spectra than standard stellar populations, and could produce large contributions to the ionizing and non-ionizing UV backgrounds. Because of redshift effects, gamma rays with low ( $< 10$  GeV) observed energies for very high-redshift sources could have significant interactions with the freely-propagating non-ionizing background. It is therefore possible that opacities at reionization redshifts could be much higher than we propose here due to unseen UV production mechanisms. While models for gamma-ray blazars do not typically predict sources at these high redshifts, GRBs are known to exist above redshift six (Greiner et al., 2009b), and long-duration GRBs could potentially be seen as far out as star-formation occurs. The EGRET experiment, operating from 30 MeV up to  $\sim 30$  GeV, was able to view a small number of photons from GRBs, and the detection of high-energy emission from GRB 080916C by the Fermi LAT demonstrates the ability of this instrument to detect GeV photons from these events. Though predictions are highly uncertain, it is possible that GRBs could produce significant numbers of photons well above 10 GeV through inverse-Compton or hadronic processes (Le & Dermer, 2008; Ando, Nakar, & Sari, 2008). Calculations of the background flux from some possible reionization scenarios and source types at  $z > 6$  may therefore be a worthwhile undertaking.

It has been suggested by a number of authors that the discrepancy between observed stellar mass density and instantaneous star-formation rate density (see Section 5.2.2) could be explained by an IMF that evolves with redshift or is more top-heavy in rapidly star-forming galaxies (Davé, 2008; Fardal et al., 2007; Baugh et al., 2005).

Alternatively, an IMF with shallower high-end slope has been suggested as a source of early reionization (Chary, 2008). Altering the high-mass end of the IMF will change the spectrum produced by galaxies and also the attenuation by dust, although as probes of star-formation generally involve the same high-mass stars that produce the UV background, there is some degree of degeneracy between these two quantities when the assumed IMF is changed. This is also an issue that warrants further study.

## Chapter 6

# Attenuation in the Spectra of High-Redshift Gamma-ray Bursts

While blazars have been the primary target of efforts to detect the effects of EBL attenuation in high-energy spectra, another exciting possibility is to see these same effects in observations of gamma-ray bursts (GRBs). Until recently, limitations on the effective areas and energy ranges of high energy experiments, and their ability to respond sufficiently quickly to burst events have hindered their ability to make the necessary observations of GeV gamma-rays. In this chapter, we develop a simple phenomenological model to predict the amount of flux from high-redshift GRBs which might be visible to current experiments over a long period of observations. We show how the UV EBL predictions of the last chapter can affect observed spectra from these sources. These preliminary results will demonstrate the potential for detecting GeV emission from high-redshift GRBs and using these observations to study the UV and optical backgrounds

in place at these times.

## 6.1 Introduction

The EGRET experiment on the Compton Gamma-ray Observatory (CGRO) operated with energy range 20 MeV–30 GeV and effective area  $\sim 1000 \text{ cm}^2$ . This experiment detected a total of 5 bursts above 30 MeV in 4 years of operation, including 4 individual photons above 1 GeV (Dingus, 1995). In contrast, the Swift mission has been finding bursts at a rate of about 8 per month since its launch in December 2004 at energies between 15 and 150 keV (Sakamoto et al., 2008), and the BATSE instrument on CGRO detected thousands of GRBs at energies between 20 keV and 2 MeV (Paciesas et al., 1999). While these EGRET detections do suggest the presence of a very-high energy component in the spectrum of some GRBs, it is difficult to draw more conclusions due to the small effective area of the instrument.

The other possibility to view high-energy emission from GRBs is with ground-based experiments – imaging atmospheric Cherenkov telescopes (IACTs) such as MAGIC, H.E.S.S., or VERITAS, or air shower arrays such as Milagro. While IACTs have the advantage of much larger effective collecting areas than any satellite, they are limited by their low duty cycles and small fields of view, which make a serendipitous GRB detection very unlikely. Therefore, these telescopes must be alerted to a burst event by another detector, usually a gamma- or x-ray satellite, and slew to its position. This introduces a new technical limitation on ground-based observations; the delay time in receiving an

alert and moving the telescope means that much or all of the primary emission for a burst can be missed. Air shower arrays like Milagro do not have slewing issues, but have generally not been as sensitive as their IACT counterparts, particularly at lower energies.

Despite the difficulties involved, followup observations have been made of many GRBs by all major experiments mentioned above. MAGIC responded to 35 burst alerts between January 2005 and June 2008, a rate of about 1 per month, with an average slew time of 45 seconds (Garczarczyk et al., 2008, see also Albert et al., 2007a). The attempts were only able to place upper limits on the flux. Negative results were also found in 32 observations over 4 years by H.E.S.S. (Aharonian et al., 2009). Most of these observations did not begin until several hours after the initial detection of the event. VERITAS has reported limits for a small number of bursts (Horan, 2008). Air shower arrays are generally less sensitive than IACTs, but have the advantage of much larger fields of view and duty cycles. The Milagro prototype, Milagrito, claimed a possible detection of prompt emission from GRB 970417A at  $> 650$  GeV energies (Atkins et al., 2003). The redshift of this burst was not known, but to be detected at these energies it would have had to have been quite nearby, as the universe becomes optically thick due to EBL attenuation for these energies at low redshift ( $z < 0.2$  for our low EBL model).

In this work, we will be focusing on two telescopes which have recently begun observations, the Fermi Gamma-ray Space Telescope and the Major Atmospheric Gamma-ray Imaging Cherenkov Telescope (MAGIC). Fermi, launched on June 11, 2008, contains two instruments. The GLAST Burst Monitor (GBM) is designed for finding

prompt emission from GRB from 10 keV to 30 MeV, and the Large Area Telescope (LAT) views gamma rays from 20 MeV to 300 GeV, with effective area  $\sim 9000 \text{ cm}^2$ , giving it both detection area and upper energy threshold about 10 times that of EGRET. Fermi has been operated in survey mode, in which it views the entire sky every 3 hours, since shortly after its launch, and will be continue to be in this mode for most of its  $>5$ -year life span. The MAGIC experiment was recently upgraded to its second phase, MAGIC-II, and consists of 2 large IACTs, each with area  $236 \text{ m}^2$  (this is the mirror area of the instrument; the effective detection area for gamma rays is much larger,  $> 10^5 \text{ m}^2$  at optimal energies). In this work, we will be modeling the properties of a single telescope, as detailed information about binocular observations that are now possible with both telescopes is not yet available. These telescopes are designed to have a low energy threshold,  $<50 \text{ GeV}$  near zenith, and are capable of repositioning to any point on the sky within 30 seconds (Bastieri et al., 2005; Albert et al., 2007a).

## 6.2 Model

In order to estimate the number of GeV gamma-rays from GRBs that will be available to Fermi and MAGIC-II, we develop a simple model to estimate the fluence that could be seen by these experiments over a given time. As only bursts with known redshift are useful to our ultimate goal of probing UV and optical background fields via attenuation effects, we base our analysis on the population of bursts observed by the Swift Burst Alert Telescope (BAT) with measured redshift. Data for these bursts

has been taken from the Swift GRB table online <sup>1</sup>. Our model rests upon two assumptions about high-energy emission: (1) that the population of bursts seen by Fermi and MAGIC-II, with redshifts that are eventually determined, will be similar to these Swift bursts in number and fluence statistics, and (2) that these bursts produce high energy emission both prompt and afterglow with fluence that is proportional to that observed in the BAT energy range, 15–150 keV. Our model is purely observational and phenomenological, and does not attempt to quantify in any way the intrinsic parameters of the bursts, nor do we make assumptions about the actual population statistics of these events.

### 6.2.1 GRB Emission

The populations of bursts seen by BATSE and Swift were analyzed in Dai (2009), who argued that these populations were similar, and that there were no difference between the subset of optically detected Swift bursts with and without redshifts. Ignoring the existence of a separate population of low luminosity ‘dark bursts’ (Virgili et al., 2009), this suggests that the events for which we now have redshift information are not different from the GRB population as a whole. There have been suggestions that the low luminosity population of bursts are distinct from their brighter counterparts (Liang et al., 2007). The BATSE sample should be very similar to that viewed by GBM on Fermi, and this should enable a test the consistency of assumption (1).

We use the 132 bursts which were observed by Swift BAT between January

---

<sup>1</sup>[http://heasarc.gsfc.nasa.gov/docs/swift/archive/grb\\_table/](http://heasarc.gsfc.nasa.gov/docs/swift/archive/grb_table/)

2005 and February 2009 and have known redshift. Figure 6.1 shows these bursts plotted as a function of redshift and BAT fluence. A considerable amount of fluence from these bursts arises largely from a few bright events; the brightest 10 per cent of bursts in the sample account for approximately 55 per cent of the fluence. While high energy flux has only been seen from a handful of bright GRBs using EGRET, the fact that these bursts account for a large fraction of fluence seen at lower energies means that our assumption (2) should be reasonable even if the proportionality does not hold for faint bursts. We have not included LAT bursts such as GRB080916C in this analysis, although we do show where this event would have been in Fig. 6.1 based on its GBM fluence. We will discuss this event in the context of our emission model in the conclusion.

Two recent papers have related the keV/MeV flux from GRBs to high energy emission, and have estimated the ratio of fluences in these regimes. Le & Dermer (2008) estimated the count rate for GeV photons in the LAT based on the bursts seen by the EGRET spark chamber. The  $F_{LAT}/F_{BATSE}$  fluence ratio inferred there varied from 5 to over 30 per cent. Based on the deadtime factors affecting some EGRET GRB observations these authors argue that a >30 per cent ratio between BATSE and EGRET is reasonable. Ando et al. (2008) made the assumption that there is a log-normal distribution of  $F_{GeV}/F_{MeV} \approx F_{EGRET}/F_{BATSE}$  in the roughly 100 BATSE bursts that were in the field of view of EGRET. A maximum likelihood fit to the available data suggested a ratio of  $0.003 \leq F_{GeV}/F_{MeV} \leq 0.06$ . Slightly different assumptions about the high-energy spectrum and energy range of the GeV emission were used in each case. The Ando work assumed an spectral index of -2.4 in the EGRET energy range,

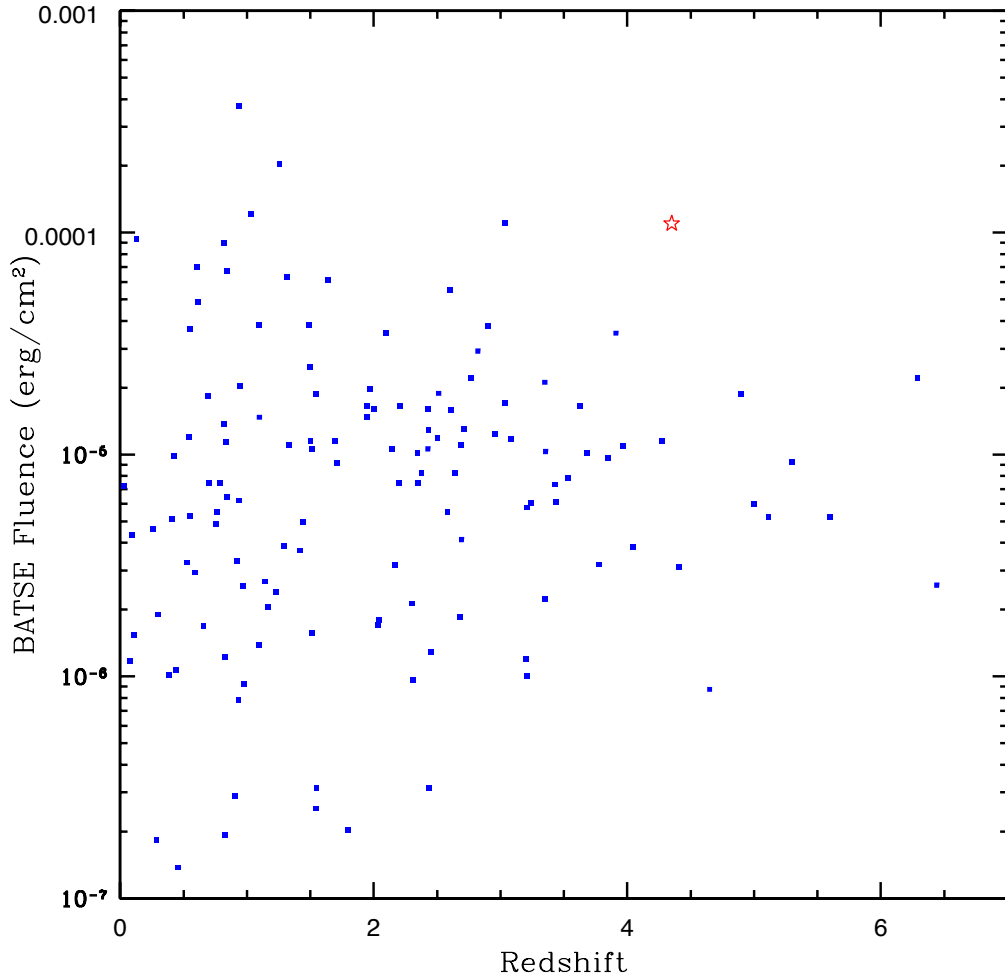


Figure 6.1: The bursts seen by Swift BAT for which we have well-measured redshifts, shown on axes of redshift and fluence. The fluences observed by BAT at energies from 15–150 keV have been converted to the BATSE energy range (20 keV – 2 MeV) using a Band function over these energy ranges with peak 250 keV and low and high energy spectral indices of -1 and -2.2, respectively. For reference, we also show the position of GRB 080916C on this plot based on its GBM fluence (single red star). This burst was not seen by Swift until nearly 17 hours after its detection by GBM and LAT (Kennea, 2008), and was not included in our analysis.

while Le & Dermer used the best fit to the EGRET bursts of -1.95 from Dingus (1995). Hardening the spectral index in the former case could have increased their values for the flux ratio coefficient significantly.

In this chapter we use the energy fluences seen by Swift BAT to predict GeV emission using the ratio

$$\rho \equiv F_{\text{EGRET}}/F_{\text{BATSE}} \quad (6.1)$$

where  $F_{\text{EGRET}}$  and  $F_{\text{BATSE}}$  refer to the fluence over the EGRET spark chamber and BATSE energy ranges, taken to be 100 MeV – 5 GeV and 20 keV – 2 MeV respectively. A constant spectral index is assumed to be valid from the EGRET energy range up to  $> 100$  GeV. We take a more conservative approach than Le & Dermer and use a value of 0.1 for prompt phase emission, which does a reasonable job matching high energy fluence seen for recent GRB 080916C, see Section 6.4.1. This is higher than the range of values proposed by Ando et al., but this paper also assumed a softer high energy spectrum in deriving results.

Afterglows are also a possible source of high-energy emission, though one that is even more poorly constrained than the prompt phase. There are a variety of mechanisms that have been hypothesized as possible sources of GeV photons. A popular assumption invokes inverse-Compton upscattering of synchrotron photons in the GRB outflow (SSC mechanism), though a variety of other sources are possible, such as SSC emission from the internal x-ray flares seen in afterglows or Compton upscattering of these photons by electrons accelerated in the external shock (Fan et al., 2008). Limits from EGRET observations suggest a typical fluence ratio of 0.01 to 0.1, and a spectral index of -1.5

to -2 (Ando et al., 2008). For afterglows, we assume in this work a ratio of  $\rho = 0.01$ .

In converting the fluence seen by Swift BAT (15 – 150 keV) to BATSE flux, we assume a common Band (Band et al., 1993) functional form over the BAT–BATSE energy range.

$$\frac{dN}{dE} = A_0 \left[ E^{\alpha_1} e^{-\frac{E}{E_{br}}(\alpha_1 - \alpha_2)} \Theta(E_{br} - E) + E_{br}^{\alpha_1 - \alpha_2} e^{\alpha_2 - \alpha_1} E^{\alpha_2} \Theta(E - E_{br}) \right]. \quad (6.2)$$

Here  $\alpha_1$  and  $\alpha_2$  are the low and high energy indices,  $E_{br}$  is the break energy, and  $\Theta$  is the Heaviside step function. Unfortunately, the relatively narrow energy band of the BAT does not allow one to resolve the structure of the Band peak in most cases for the Swift sample. We use parameters -1 and -2.2 for the low and high indices, and assume a break energy of 250 keV; these are the typical values seen in an analysis of BATSE bursts by Preece et al. (2000), and lead to a ratio of 4.6 between the BATSE and BAT fluences. The high energy flux in this model, effective in the EGRET energy range and at GeV energies, is taken to be a power law with normalization found from the MeV–GeV proportionality, and is separate from the high-energy Band slope  $\alpha_2$ . The GeV flux is then

$$\frac{dF}{dE} = \frac{\rho F_{\text{BATSE}}}{\int_{\text{EGRET}} E^\beta dE} E^\beta \quad (6.3)$$

where  $\beta$  is the high-energy spectral index and is determined independently of the Band function parameters. We assume a high energy spectral index of  $-1.95$  for prompt phase photons, consistent with the EGRET results, and a harder spectral index of  $-1.5$  for the afterglow component, which would occur if the spectral peak from inverse Compton emission is at energies equal to or higher than those being observed. We do

not discriminate between long and short bursts in our analysis. As can be seen in Figure 6.2, only a small fraction of the bursts in our sample can be classified as short ( $T_{90} \leq 2$  sec), and their contribution to the total flux is very low.

The inverse-Compton scattering of photons to high energies is limited by Klein-Nishina suppression, which reduces the flux of photons at energies which are higher than the electron rest mass  $m_e$  in the particle's rest frame. We will not include a possible cutoff due to this effect in our calculation, but will reserve discussions of the implication until Section 6.4.2. In the simple SSC case (Chiang & Dermer, 1999; Zhang & Mészáros, 2001; Sari & Esin, 2001), this can be written as

$$E_{KN} \gtrsim \Gamma_b \gamma_e m_e c^2, \quad (6.4)$$

where  $\Gamma_b$  is the bulk Lorentz factor of the outflow, and  $\gamma_e$  is the typical factor for the electrons responsible for the synchrotron peak. Including the effect of redshift, the affected observed gamma-ray energies are (Panaitescu, 2008)

$$E_{obs} \gtrsim \frac{\Gamma_b \gamma_e}{1700(1+z)} \text{ GeV}. \quad (6.5)$$

Constraints from beaming and escape of high-energy radiation suggest large Lorentz factors for the bulk flow of material in the prompt and early afterglow phases of bursts,  $\Gamma_b \sim 100$  (Meszaros, 2006). The electron will typically have a power law distribution in energy determined by the cooling rate and therefore this is not a abrupt spectral cutoff, but if the typical factor is sufficiently low then Klein-Nishina effects could impact the observations in the 10–100 GeV energy range. As mentioned in Ando et al. (2008), the electron Lorentz factor in external shocks in the afterglow is expected to be higher

than that of the prompt emission, and therefore this may be a more likely source of detectable high energy photons.

### 6.2.2 Instrument Properties

The LAT instrument on Fermi can be described with a relatively small number of parameters. We take the LAT to have an effective area of  $9000 \text{ cm}^2$  up to an upper energy threshold of 300 GeV. The integrated field of view for Fermi is found to be approximately  $\sim 20500 \text{ cm}^2 \text{ sr}$ ; we therefore assume a field of view  $20500/9000 \approx 2.28 \text{ sr}$ . It is assumed in our analysis that Fermi will be in survey mode at all times, and that triggered rotations to view GRBs will not significantly raise the number of high-energy photons gathered.

The observations of GRBs by IACTs such as MAGIC are highly sensitive to the capabilities of the instrument. While these telescopes have much larger effective collection areas than space-based instruments such as the LAT, other constraints such as the energy threshold, duty cycle, and time to respond to an alert must be taken into account in the analysis. The much larger area of these telescopes compared to Fermi is compensated by the relatively small probability that any single event will be observable. The effective area of IACTs becomes a strong function of energy in the sub-TeV regime, as the difficulty in reconstructing low energy showers leads to a sharp decrease in effective coverage near threshold. Observations of GRBs are strongly affected by the low energy capabilities of the instrument, due to the rapidly increasing opacity of the universe to gamma rays above a couple hundred GeV for all but the

closest bursts. For MAGIC, we have used the ‘after cuts’ form for the effective area as a function of energy from Albert et al. (2008b), and assume an absolute lower energy threshold of 50 GeV for observations at zenith. For observations away from zenith, the threshold typically increases due to the increasing amount of atmosphere through which the particle shower is being observed. Following Baixeras (2004), we model this effect as the following function of angle from zenith  $\theta$ ,

$$E_{th}(\theta) = E_{th}(0) \cdot (\cos \theta)^{-3.1}, \quad (6.6)$$

with  $E_{th}(0) = 50$  GeV.

A realistic estimate of the instrument duty cycle is critical for our analysis. As outlined in Bastieri et al. (2005), there are several requirements for operation of MAGIC, including distance of the sun from zenith ( $> 108$  deg), a minimum angular distance of the moon from the observation field ( $> 30$  deg), and humidity and wind requirements. For the duty cycle of the instrument, we use the standard value of 10 per cent, and note that this is supported by the fraction of acceptable GRBs (9.2 per cent) which were responded to in 42 months of observations (Garczarczyk et al., 2008), and is similar to what other IACTs have traditionally experienced.

A major challenge for ground-based attempts to detect GRBs has been the highly transitory nature of the emission. Responding to an event requires the minimization of the several components of the total delay time, including the time for the detecting satellite to confirm a burst in progress, the time to transmit this information, and then the time for the ground-based telescope to slew to the coordinates and begin

taking data. The first quantity is dependent on the satellite responsible for initial detection and strength of the burst, but typical numbers for the Swift BAT are  $< 15$  sec to confirm and transmit a coordinate with precision of a few arcminutes. Communications of these coordinates are received in real time ( $\sim 2$  sec, Bastieri et al., 2005) over the GRB Coordinate Network (GCN)<sup>2</sup>. However, the final step of repositioning a telescope the size of MAGIC (or even the marginally smaller VERITAS or H.E.S.S. telescopes) on the required time scale presents a major engineering challenge. Ensuring personnel safety is also a major practical concern in minimizing response time, which requires that the telescope be able to reposition without warning at any time during operation.

For our analysis, we assume a delay time  $T_{delay}$ , which incorporates all three times discussed above, in prompt observations. For MAGIC, we assume a typical report time of 15 seconds for the burst alert to reach the instrument, and 30 sec slew time to move to the target and begin observations. This total of 45 seconds is about equal to the lowest time, 43 sec, reported in Garczarzyk et al. (2008) for all of MAGIC GRB responses to date, and is therefore optimistic. To compute the flux in the prompt phase of a GRB which can be seen by ground-based observations after this delay time we use the T90 variable in BAT flux reported for our sample of bursts. The fluence of the burst is modified by a factor

$$F = F_{BAT} \cdot \text{MAX} \left[ \frac{T_{90} - T_{delay}}{T_{90}}, 0 \right] \quad (6.7)$$

that is, we take the prompt phase emission profile to be approximately flat over this timescale, and reduce the fluence by the proportion of the prompt phase that was

---

<sup>2</sup><http://gcn.gsfc.nasa.gov/>

missed. Delays due to IACT response time do not affect the observation of afterglows. We also do not account for the fact that on a timescale of hours sidereal motion can bring afterglows into and out of the viewing region of the telescope. In Figure 6.2, we show how the time delay in IACT observations affects received flux in our model. It is worth pointing out here that we do not find  $T_{90}$  to be correlated with either fluence or redshift in our sample; its correlation coefficients with these variables are -0.017 and -0.014, respectively.

### 6.3 Results

Based on the model for GRB emission and instrument performance developed in the previous section, we predict the number of observable high-energy gamma rays available per year using the data set of Swift BAT GRBs with confirmed redshifts. We present these results in terms of broad bins in redshift, so as to have a reasonable statistical sample in each bin. In Table 6.1 we show the redshift bins, number of bursts seen in 50 months operations, and total fluence. Also, in Table 6.2, we review the parameters for the emission model and instrument properties which we are using in this section.

After calculating the high energy gamma-ray fluence for each burst in the sample, the flux is attenuated using optical depths calculated from the evolving background spectral energy distribution; see Madau & Phinney (1996) for a review of these

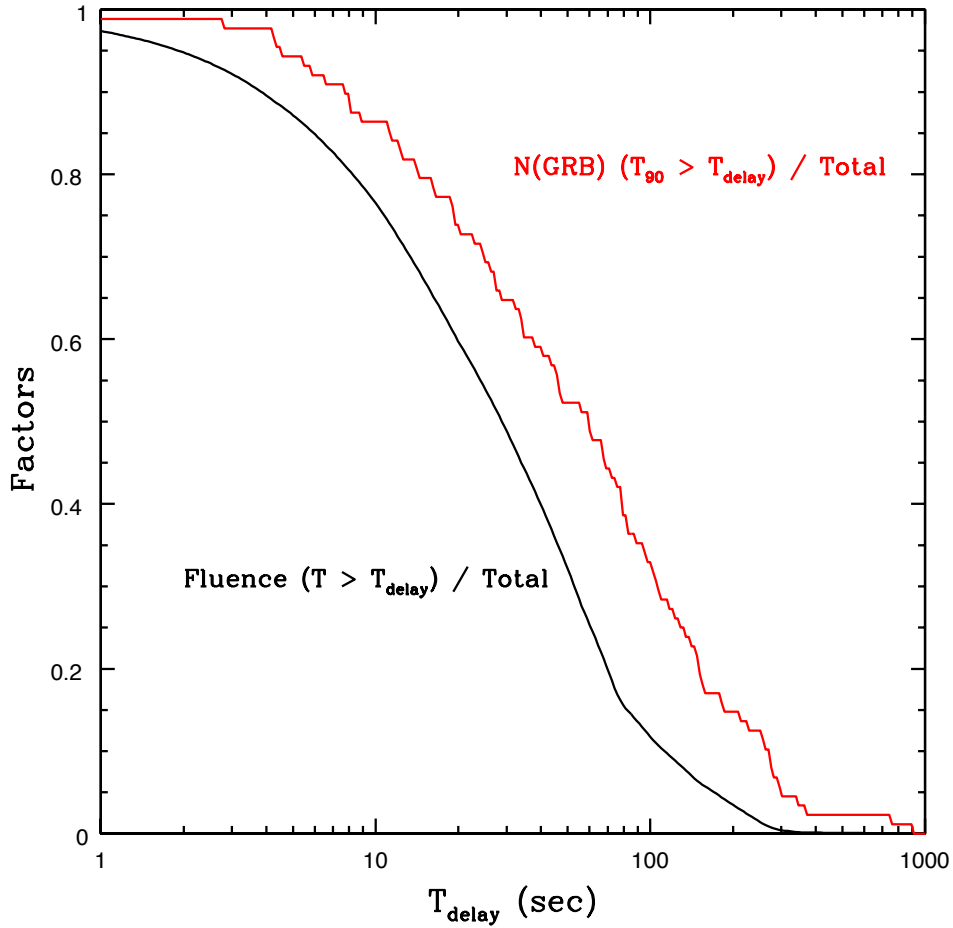


Figure 6.2: The fluence factors arising due to the slow time delay for ground-based telescopes. The solid black curve shows the percentage of prompt fluence in the total sample which is seen after a time  $T_{\text{delay}}$ , if the GeV flux is proportional to that in the BAT energy range and is constant across  $T_{90}$ . The red curve shows the fraction of GRBs for which  $T_{90}$  is longer than  $T_{\text{delay}}$ . This plot shows the percentage of high energy emission that will be missed by a telescope with a given delay time (due to slewing and other factors) in our model, after averaging over all Swift bursts.

Table 6.1: The redshift bins we use in our analysis and the numbers of GRBs and total fluence in each bin for the sample of Swift bursts. The fluences shown are in the BAT energy range, 15–150 keV. These data are over 50 months of observations, from January 2005 to February 2009.

Redshift Bin	N(GRB)	Fluence ( $10^{-7}$ erg cm $^{-2}$ )
$1 < z < 2$	28	1549.9
$2 < z < 3$	31	856.3
$3 < z < 4$	19	639.1
$4 < z < 6$	9	138.3

Table 6.2: Some of the parameters we use for calculations of this section. See Sections 6.2.1 and 6.2.2 for more details.

$F_{\text{BATSE}}/F_{\text{BAT}}$	4.6	BAT to BATSE fluence ratio
$\rho_{pr}$	0.1	Fluence ratio for prompt phase
$\beta_{pr}$	-1.95	Prompt phase spectral index
$\rho_{ag}$	0.01	Fluence ratio for afterglow phase
$\beta_{ag}$	-1.5	Afterglow spectral index
$T_{\text{delay}}$	45 sec	Delay time for MAGIC observations

calculations. In each redshift bin, we use attenuation factors averaged in redshift,

$$\frac{dF_{\text{obs}}}{dE} = \frac{dF}{dE} \int_{z_1}^{z_2} \frac{e^{-\tau(E,z)}}{z_2 - z_1} dz, \quad (6.8)$$

where  $dF/dE$  is the high energy spectrum from Equation 6.3, and  $\tau(E, z)$  is the EBL optical depth as a function of observed gamma-ray energy and source redshift. High-energy gamma rays are therefore assumed to originate from sources evenly distributed across the redshift bin.

### 6.3.1 Predicted Fluences for Fermi

In this section we present predictions for the number of GeV gamma rays which are visible per year to Fermi. Figure 6.3 presents the main results of this section; the mean number of photons above a given energy available without absorption by the EBL,

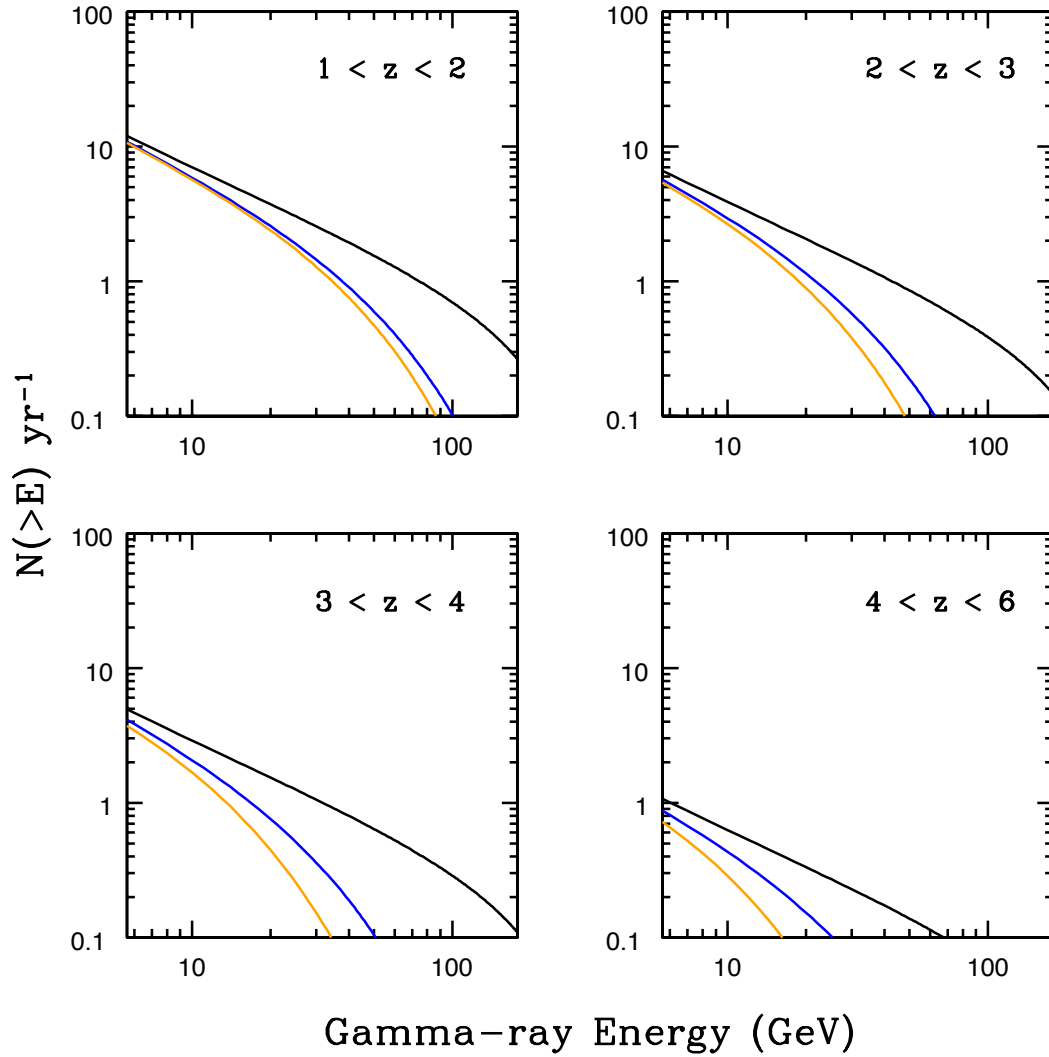


Figure 6.3: The mean number of integrated photons above a given energy visible to Fermi per year, up to the maximum LAT energy of 300 GeV. The black line shows the unabsorbed rate, while the blue and orange lines show results with attenuation due to the low and high-peaked EBL models.

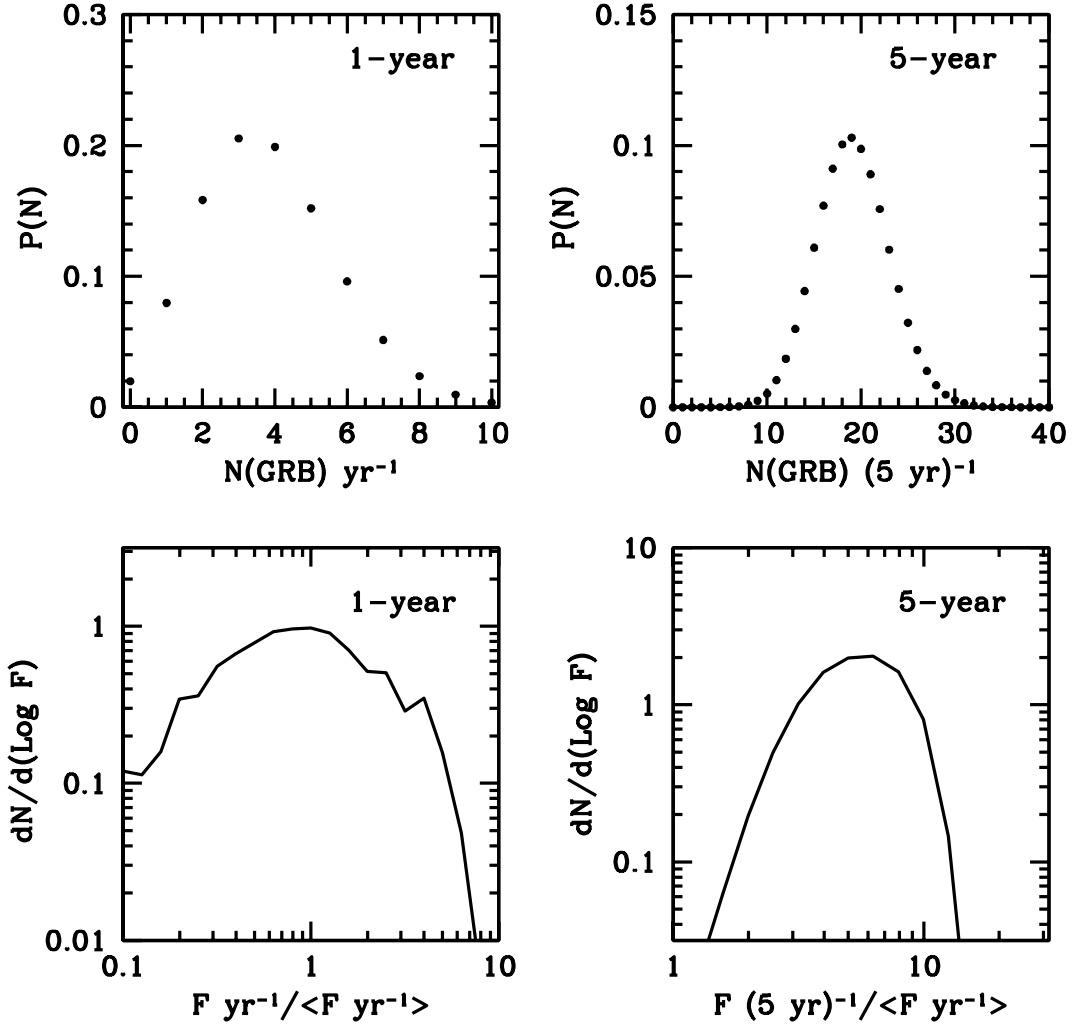


Figure 6.4: The variation in yearly predictions for observations of GeV gamma rays from GRBs with the Fermi LAT. The upper-left plot shows the annual probability of a given number of GRBs occurring in view of the LAT with redshifts between 1 and 6. This does not take into account the expected number of GeV photons from each GRB, which may be less than one. The lower-left plot is the yearly distribution of stacked fluences, normalized to the mean yearly predictions in Figure 6.3. On the right-hand side we show the same quantities computed for a 5-year period.

and after absorption by our two background models. These predictions are made by combining our models for high energy GRB emission for the Swift population and Fermi instrument properties, making adjustments for the field of view and effective areas for each satellite. Our results here are divided into the four redshift bins, and show the averaged total amount of fluence from sources at these redshifts per year.

In Figure 6.4 we show how the mean fluence predictions can be expected to vary from year to year, based on the number of bursts in the Swift sample and the variance in fluence in this population. This plot has been created using a year-by-year simulation of LAT observations, and assuming randomly occurring bursts with the flux and redshift distribution of the Swift population. The upper plots show the number of high-redshift ( $1 < z < 6$ ) bursts falling in the field of view of the detector over a period of 1 (upper-left) and 5 (upper-right) years; this simply follows a Poisson distribution. As before, we do not account for the possibility of the spacecraft autonomously slewing to view events with the LAT after being triggered by the GBM or another experiment. The lower plots show how the stacked fluence collected over a year can be expected to vary from the predictions in the previous figure.

### 6.3.2 Predicted Fluences for MAGIC

For MAGIC, we begin by considering the year-to-year probability that a given number of high-redshift GRBs will occur in a region of sky where they can be seen with low threshold. By multiplying the duty cycle of the instrument (10 per cent) with the sky coverage (11.7 per cent for  $\theta_{max} = 40$  deg), we find that only  $\sim 1$  per cent of

bursts can be observed with a reasonably low energy threshold. Our sample consists of 132 bursts seen over 50 months, 89 of which are at  $z > 1$ , and therefore the expected number of bursts per year is somewhat less than 1. Therefore, we begin by predicting the probability that any bursts will be visible in a given year. Once we understand this probability, we will look at the photon statistics for the years in which one or more bursts are seen.

The sky coverage of the telescope increases approximately as the square of the maximum allowed angle from zenith. However, we find that the number of photons predicted from distant ( $z > 1$ ) bursts does not increase significantly beyond an angle of about 40 degrees, as the energy threshold of the instrument rises above the energies at which the universe is transparent to gamma-rays. GRBs which occur far from zenith are therefore shrouded from view by EBL attenuation unless they are at low redshift. The number of bursts per year will also depend on whether prompt or afterglow phases are being considered, as the  $T_{90}$  duration of some GRBs will be less than  $T_{delay}$ , preventing most or all of their prompt emission being viewed. In Table 6.3 we present probabilities for the number of GRBs visible to MAGIC per year, within a given maximum angle from zenith.

Table 6.3: The annual probabilities of a given number of GRBs falling within a given angle from zenith, assuming a duty cycle of 10 per cent. Under ‘afterglows’, we include all bursts, and for ‘prompt’ only those with  $T_{90} > T_{delay}$ . Note that this calculation is for the number of GRBs falling in view of the instrument, and does not predict the number of expected photons, which may be less than one. In Figure 6.5 and 6.6 we show the number of photons received in years with a non-zero (usually 1) number of bursts, using our emission model, and taking into account EBL attenuation and instrument effective area. Based on Equation 6.6, the energy threshold for MAGIC, taken to be 50 GeV at zenith, is 60 GeV at 20 degrees, 78 GeV at 30 deg, and 115 GeV at 40 deg.

N(GRB) yr <sup>-1</sup>	Prompt ( $T_{delay} = 45$ )			Afterglow ( $T_{delay} = 0$ )		
	20 deg	30 deg	40 deg	20 deg	30 deg	40 deg
0	0.965	0.924	0.871	0.939	0.869	0.783
1	0.034	0.073	0.120	0.057	0.121	0.192
$\geq 2$	0.001	0.003	0.009	0.002	0.010	0.025

We find that the probability of a high redshift burst falling within the field of view of the instrument in any particular year are small,  $\sim 20$  per cent for  $\theta_{max} = 40$  deg. At this zenith angle, the energy threshold is 115 GeV, and rises rapidly for larger angles. It is not realistic to expect to see GRBs at  $z > 1$  at larger zenith angles for either of our EBL models due to attenuation, though low redshift bursts could be visible if photon emission takes place at high enough energies. In years in which a nonzero number of bursts are in view of the telescope, the predicted flux is expected to vary highly due to the large range of fluences seen the Swift sample (y-axis in Figure 6.1). It is therefore not particularly useful to describe an ‘average’ year, as we did in the previous section when discussing Fermi, as the median number of gamma-rays from GRBs in this case is zero.

In Figure 6.5 we show the probability distribution for the number of detected photons expected in those years that MAGIC has the opportunity to view at least 1 distant ( $z \geq 1$ ) GRB within  $\theta_{max}$  as a histogram. The predicted high energy flux has been attenuated using our two evolving background models. The distribution of bursts within the disk of radius  $\theta_{max}$  surrounding zenith is also randomized, and the energy threshold calculated using Equation 6.6. Figure 6.6 shows the same plot including only the prompt phase photons.

Figure 6.7 shows the expected  $dN/dE$  spectrum of photons arriving from GRBs at different redshifts. This plot takes into account the assumed gamma-ray spectrum, the instrument effective area, the energy threshold vs angle from zenith relation, and EBL attenuation. As the actual attenuation factors vary over a given redshift bin, these

results are approximate. For MAGIC, we find that photons are expected to be seen in a fairly narrow energy range peaking at  $\sim 100$  GeV. The number of photons expected near the minimum energy of the instrument are suppressed due to the small effective area and limited sky coverage for low threshold observations. At higher energies, the spectrum declines rapidly due to EBL attenuation. As none of these spectral factors depend on absolute fluence in our model, these results are valid regardless of the luminosity of the GRB. We have normalized the spectra to the average yearly flux for convenience, however this normalization in itself has little meaning due to the large amount of variance in our predictions.

## 6.4 Discussion

We have attempted to make predictions for the number of high-energy gamma rays that can be seen by current generation of telescopes targeting the GeV energy range. Although we have strived to design a simple and straightforward model, there are a large number of uncertainties in predicting the high-energy emission of GRBs. Over the next few years, observations in the GeV energy band will be able to constrain many of the assumptions that we have used here.

Our findings suggest that Fermi will typically observe at least 3 to 4 bursts per year with redshift that are determined to be greater than 1. Over the lifetime of the mission ( $>5$  yr), this means that multiple events will likely be seen in each of the redshift bins. While not all these GRBs will necessarily have detectable GeV emission,

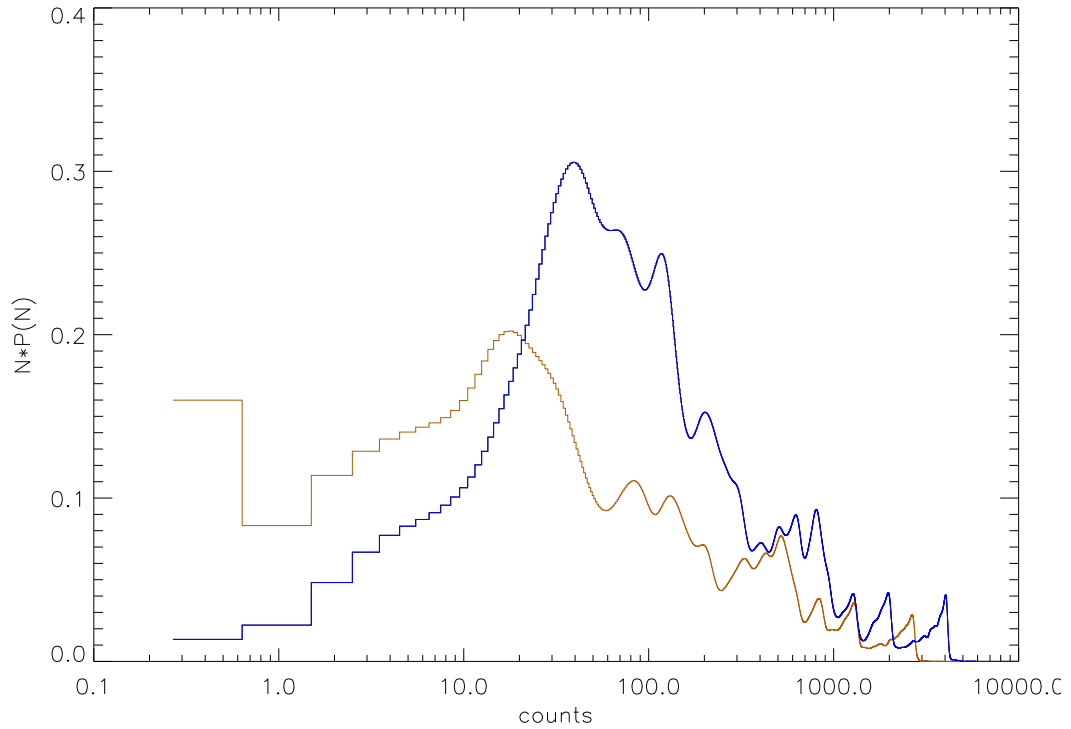


Figure 6.5: The number of gamma-rays seen by MAGIC per year, for those years in which at least 1 GRB falls within the field of view of the telescope (see Table 6.3), using parameters  $T_{delay}=45$  sec and  $\theta_{max} = 40$  deg. Blue and orange lines show the results after attenuation by the low and high-peaked EBL models, respectively. The leftmost bin is the probability of zero photons being received.

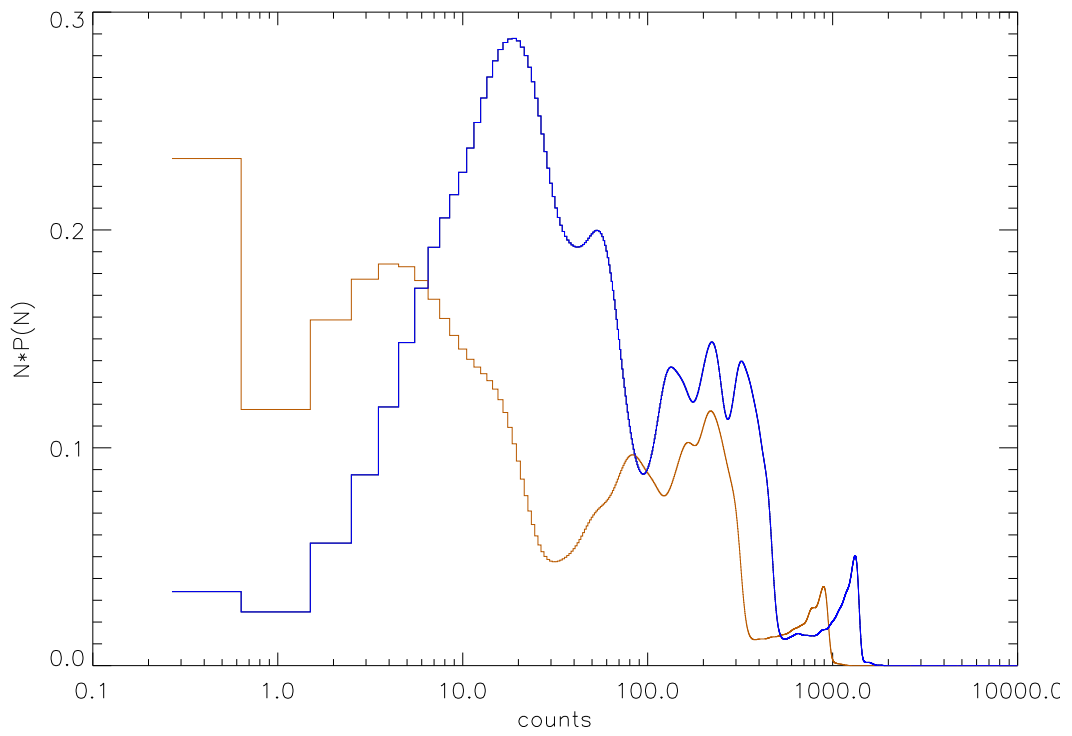


Figure 6.6: As in the previous figure, but showing only the photons from the prompt phase of emission.

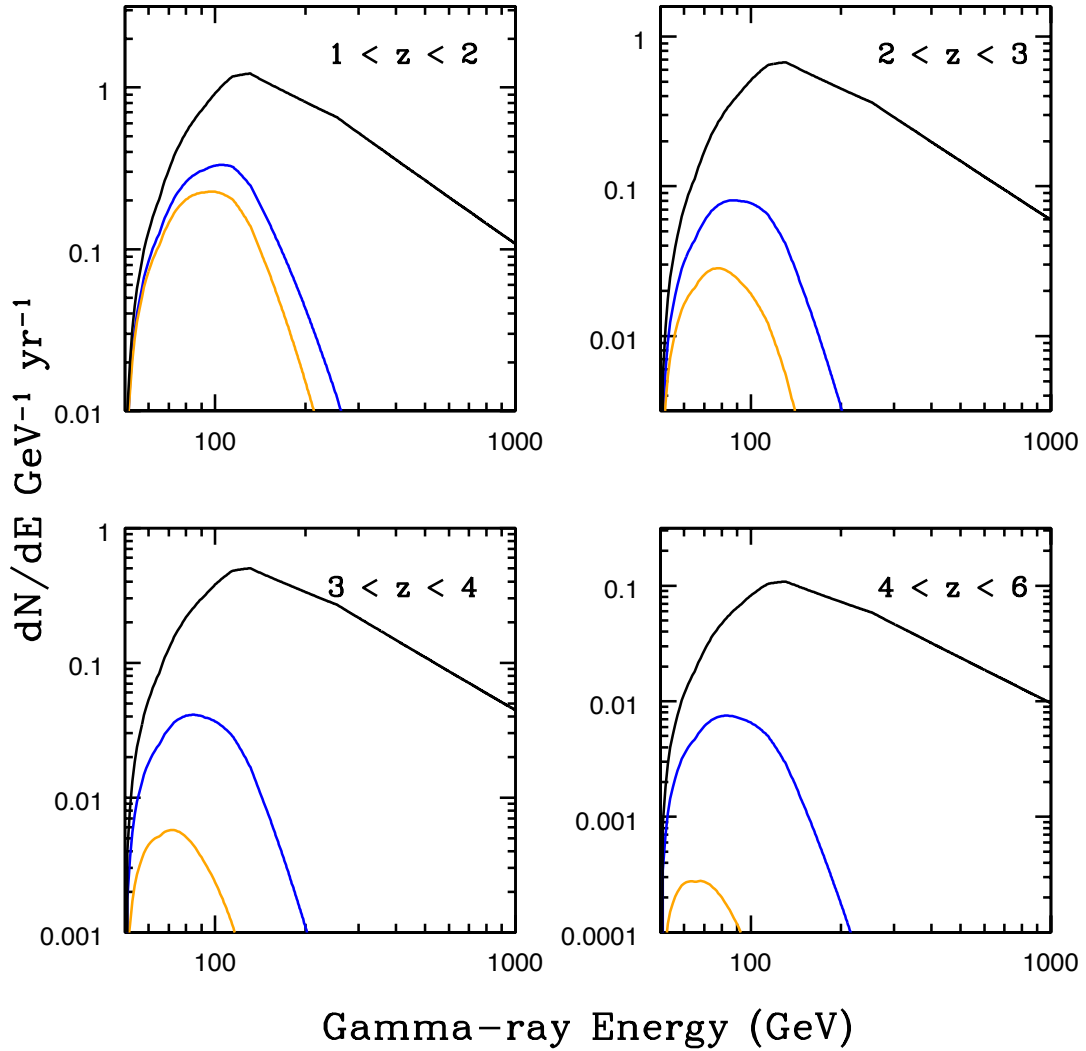


Figure 6.7: Predictions for the spectrum observable by MAGIC from distant GRBs, at 4 different redshifts. The black line is the unattenuated spectrum, and the orange and blue lines show the flux after attenuation by the high-peaked and low EBL models. The fluence is normalized to the average per year, as was done for our Fermi results. However, as we have seen, the year-to-year prediction is highly variable. So the vertical scale of the plot should be taken as arbitrary, and Figs. 6.5 and 6.6 used as a gauge of expected number of counts.

the stacked results could yield enough photons above 10 GeV to place constraints on the EBL, and possibly differentiate between the two models we have presented here. It is difficult to make generalizations about yearly predictions, due to the large amount of variance in both number of bursts viewed and fluence per individual burst, which vary over orders of magnitude. Our predictions become more stable over the 5-year instrument lifetime (right-hand panels of Fig. 6.4); the probability of our results varying by more than a factor of  $\sim 2$  from predictions on this timescale is small, at least when totals from all redshift bins are considered (this is likely smaller than the expected variation in  $\rho$  from Section 6.2.1). We predict, on average, several photons per year above 10 GeV for  $1 \leq z \leq 2$  and two or three from  $2 \leq z \leq 3$ . This is somewhat more optimistic than the prediction of in Le & Dermer (2008), who considered all long-duration bursts over the full sky. We did assume a harder spectrum for prompt emission than in this work (-1.95 versus -2.2). We have not included autonomous repoints of the instrument in response to a GBM trigger in our model. If repoints are performed frequently and prove an effective way to view GeV emission from bursts, then this could effectively increase the LAT field of view to 1/2 the sky, a factor of 2.5 higher than we consider.

For an IACT like MAGIC, the annual likelihood of viewing one or more distant GRBs within 40 degrees of zenith is only about 1 in 5. At this angle, the energy threshold for the telescope is about 115 GeV, using Equation 6.6. We have chosen this cutoff due to the rapidly growing energy threshold at higher angles, and the fact that the EBL absorption attenuates most emission at these energies for sources at  $z > 1$  in all of our

EBL models. As shown in Figure 6.7, the majority of photons from these bursts can be expected to arrive at  $\sim 100$  GeV, or lower for high redshift sources. This means that it is the capabilities of the detector near to the lower end of its energy range that are most important to viewing distant GRBs, not the energies at which the instrument necessarily has the most sensitivity. For GRBs at lower redshifts, more photons may be observable in the 100 GeV to 1 TeV decade, but these bursts only represent a minority of those for which we have redshifts. Another reason for restricting ourselves to the 10 to  $\sim 100$  GeV decade is that we are relying on EGRET observations at maximum energies of  $\sim 10$  GeV to model our high-energy emission, and we expect this model to become increasingly uncertain at higher energies. Our main results from this section show the potential of receiving a large number of photon counts from a single GRB. Even a relatively small number of gamma rays could be very useful in constraining the EBL through its effects on the spectrum and total power of the VHE emission. Our results suggest that there is a large degree of chance involved in seeing GRBs from the ground, but there could be a large payoff for our knowledge of cosmology from even one success.

For both MAGIC and Fermi, we have based our calculation on the population of bursts seen by Swift for which redshifts were eventually determined. However, Fermi is a capable finder of transients, covering approximately  $1/5^{th}$  of the sky with the LAT and possibly more after GBM-triggered repointings are taken into account. Above 10 GeV, the LAT has an angular resolution of  $\leq 0.1$  degrees, allowing strong bursts to be targeted for multiwavelength observations. It is therefore possible that Fermi will

enable the calculation of many GRB redshifts on its own, and the number of high-redshift bursts we have predicted for the next few years could be an underestimate. This could improve the prospects for detecting GeV photons from these sources with both Fermi and IACTs.

Another factor that was not taken into account in this analysis, but which could increase the number of GRBs falling within the view of IACTs, is the anti-solar bias in the distribution of Swift GRBs. As the determination of redshifts from afterglow observation is hampered by glare from the sun, Swift preferentially finds GRB events in the anti-solar direction. This would work to the advantage of IACTs, which can only operate at night, by effectively increasing the duty cycle with respect to Swift-triggered bursts. A preliminary look at the distribution of GRBs relative to the sun finds that about 2/3 of GRBs in our sample occurred at  $> 90$  deg from the position of the sun. In the future, we hope to include in our calculation a more precise estimate of the impact of this bias.

#### **6.4.1 Simulated Results for GRB 080916C**

One exciting implication in our findings is the potential payoff from a single bright GRB. For MAGIC, we find that while the probability of seeing photons from any single event is quite small, the reward for catching a burst of intermediate to high fluence could be hundreds or thousands of photons observed within a narrow energy range. The detailed spectrum from such an event could be invaluable for constraining the UV background and high-redshift galaxy formation. Just as a demonstration of

how many photons one event could provide, we consider recent GRB 080916C which was observed in its full prompt phase by the Fermi LAT, as well as GBM. Swift did not observe this event until nearly a day afterwards, and it was not included in the calculations of the previous section. This burst, which occurred on September 16, 2008, is among the brightest GRBs ever seen, and with a redshift of  $4.35 \pm 0.15$  it is the most energetic burst currently known (Greiner et al., 2009a). As described in Abdo et al. (2009), it was seen by the LAT at an angle of 48 degrees from boresight following a trigger from the GBM. A total of 145 gamma rays above 100 MeV and 14 gamma rays above 1 GeV were reported. The last of those 14 gamma rays arrived approximately 46 seconds after the initial trigger. The highest energy gamma was measured to be  $13.22^{+0.77}_{-1.54}$  GeV, and occurred 16.54 seconds after the trigger.

A useful test of our emission model is to ask if we arrive at similar results for the number of LAT-observed photons above 1 GeV, using the GBM fluence of  $1.1 \times 10^{-4}$  erg  $\text{cm}^{-2}$  as the basis for our calculation. Following the same analysis as in Section 6.3.1 for this single GRB, we predict 24 and 23 photons above 1 GeV respectively for our low and high-peaked EBL models. For photons above 10 GeV, we predict 1.9 and 1.4 photons for the two models. The number of predicted cumulative counts falls below 1 for energies of 15 and 11 GeV. Thus, while our emission model overpredicts the number of photons around 1 GeV, it does a remarkably good job of predicting the highest energy photon seen by the LAT for this event. The discrepancy at 1 GeV may be an instrumental effect, or it could be that the spectrum near 1 GeV is harder than we have assumed. The role of the EBL in this energy range is minimal. Our low and high-peaked

models give optical depths of 0.06 and 0.22 for a photon of 13.2 GeV from redshift 4.35, corresponding to attenuation factors ( $e^{-\tau}$ ) 0.94 and 0.80. The reason our models give different values for cumulative photon counts is mainly due to attenuation at higher energies, where less than one photon is actually predicted.

Next, we consider a hypothetical observation of this GRB by MAGIC. As the last photon from GRB 080916C above 1 GeV arrived at about 46 seconds after the initial trigger, it is unlikely that MAGIC or other IACTs could have seen much of the prompt emission, and the counts we calculate here are entirely from a hypothesized afterglow component. For an IACT, observations of this burst would have heavily dependent on the assumed EBL model, due to its high redshift. We calculate that MAGIC could have seen 350 gamma rays for the EBL in our low model; in the fiducial and fiducial high-peaked models 58 and 19 gamma rays would be seen. This assumes ideal viewing conditions, with the GRB occurring directly overhead, and in reality the chances of such an occurrence are exceedingly small. At higher angles from zenith, the number of observable photons declines rapidly due to the EBL attenuation being a strong function of energy. If the event is instead seen at 40 degrees from zenith, the MAGIC energy threshold would have been  $\approx 115$  GeV, and the predicted gamma-rays counts for those same three EBL models would be 61, 2, and 0.24. As we see, predictions can vary enormously for high-redshift GRBs depending on the background model. The fiducial and high-peaked models create a dense background of UV photons due to earlier star formation, and 100 GeV gamma-rays from a source at  $z \sim 4$  are attenuated by a factor  $> 100$ . Our low model has much less star formation at high redshift, and the optical

depth to gamma rays is much lower, though the universe is still optically thick ( $\tau > 1$ ) at this redshift for photons above 50 GeV.

As mentioned in Abdo et al. (2009), the high energy emission measured by the LAT was delayed slightly compared to the GBM flux. The highest energy photon, and two others which had energies above 6 GeV did not arrive until over 83 per cent of the prompt GMB fluence had been received (as seen in Table 1 of this reference). While it is difficult to draw conclusions from one event, this may indicate that the VHE photons produced in the prompt phase may arrive later than the lower energy fluence which defines  $T_{90}$ , or possibly that the spectrum hardens with time and GeV photons tend to arrive later than lower energy emission. We have assumed in our analysis that MeV and GeV prompt-phase flux are directly proportional in time with a constant spectrum. If there is a delay or spectral hardening it could work to the advantage of ground-based instruments, allowing them more time to react to a GRB report than we have granted here.

#### 6.4.2 Intrinsic Spectral Cutoffs

One hurdle in detecting gamma-ray attenuation features could be the existence of a spectral cutoff due to either the Klein-Nishina cutoff or internal absorption of gamma rays. As described in Equation 6.5, the relevant energy scale is determined by the bulk Lorentz factor of the GRB ejecta and the typical electron relativistic Lorentz factor. The analysis of GRB 080916C suggests a bulk factor of  $\Gamma_{bulk} \geq 887 \pm 21$  during the time intervals when the highest energy gamma rays were emitted. If the electron

Lorentz factor was at least  $\sim 10^3$ , then emission that could be observed by MAGIC would not be affected. However, as the most powerful GRB on record, parameters for GRB 080916C may not be representative of the total sample. One potential danger is that the typical energy of the cutoff could exist at roughly the same GeV energies where we expect EBL attenuation features to be seen. Not only could a sharp spectral cutoff be mistaken for attenuation by background radiation, but the factor of  $(1+z)^{-1}$  from cosmology could mimic the redshift evolution of EBL attenuation.

### 6.4.3 Future Experiments

One reason we have restricted ourselves to current experiments in this discussion is that, as we have seen, the details of instrument capabilities can have a large impact on predictions, and our results are most meaningful when we can incorporate well-tested and verified instrument parameters into our model. But as the understanding of GeV emission and spectra of GRBs is certainly not a question which is going to be decided by the current generation of instruments, our discussion would not be complete without mentioning in brief a few important upcoming experiments. The next phase of the H.E.S.S. array will feature a 600 m<sup>2</sup> mirror at the center of its current 4-telescope configuration; this central ‘T5’ telescope will be the largest IACT yet built. This upgrade is scheduled for completion later this year, and will lower the energy threshold down to  $\sim 30$  GeV at zenith angle 18 degrees (Becherini et al., 2008). Over the next decade, several ground-based experiments will provide more sensitivity to VHE photons from GRBs (Williams et al., 2009). The Advanced Gamma-Ray Imaging System (AGIS)

(Buckley et al., 2008) and Cherenkov Telescope Array (CTA) (Martinez, 2008) are two future concepts for IACT arrays that may be constructed during the next decade. Both of these arrays, when fully constructed, would have much larger collection areas than any current experiment, and would likely have energy coverage over most of the 10 to 100 GeV decade. Unfortunately, these telescopes will not be able to overcome the intrinsic difficulties of the Cherenkov technique, namely low duty cycle, loss of sensitivity away from zenith, and the need to be triggered for transient observations by another experiment. Our results suggest that due to the stochastic nature of GRBs, persistence may ultimately be the key to detecting one of these events from the ground.

## Chapter 7

### Conclusions and Future Work

I have presented new models for the evolving extragalactic background light over a wide range of wavelengths, from the extreme-UV to the submillimeter, and discussed how this photon field obscures gamma-ray observations for extragalactic sources. We have found results that are generally near the lower bounds set by number counts across the optical and IR. This finding of a minimal background field implies that most of the sources producing the present-day EBL have been resolved in surveys. Our predicted EBL is good news for ground-based gamma-ray experiments that are searching for more AGN-type sources at redshifts higher than those that have currently been found. At 100 GeV, the universe remains optically thin out to  $z > 1$  for both of our models, suggesting that the EBL will not be a major barrier to low energy observations by current and upcoming experiments with energy thresholds lower than this value.

Our calculated EBL is lower than those proposed by many other authors using backwards evolution models (Stecker et al., 2006) and modeling of the cosmic star-

formation history (Kneiske et al., 2004). Directly inferring the EBL from observed evolution of the galaxy population has become a much more powerful technique in the past few years, thanks to large-scale surveys with powerful telescopes such as HST and Spitzer. More recent models such as those of Franceschini et al. (2008) and also Razzaque et al. (2008) have found results quite similar to ours, particularly in the optical peak. This suggests that there is a convergence among these methods that utilize observed luminosity evolution and results from semi-analytic models.

However, at high redshift, measurements of the luminosity density remain very uncertain. At  $z > 2$ , the UV background is poorly understood due to uncertainties in the star-formation rate, the quasar contribution, and other factors such as typical dust attenuation in star-forming galaxies. The UV background models that I have presented in Chapter 5 broadly span the possibilities in these parameters. In this chapter, we also employed the technique of using the inferred ionization rate of the Lyman- $\alpha$  forest as a test of the background. Though it is difficult to directly draw conclusions from these data alone due to uncertainty in the ionizing escape fraction of galaxies, we do find that the models with higher star-formation rates can match observations reasonably well with a standard value for the escape fraction, while the low model requires an escape fraction that is higher than generally assumed. Our extremely quasar-dominated model, which produced a large contribution to the background at  $z > 2.3$ , is disfavored by new flux-decrement analysis data as well as measurements of the relative He II and H I column densities, which tentatively rule out such a large contribution from a hard-spectrum source.

The UV background predicted in this model gives rise to a cutoff in gamma rays between 10 and 100 GeV, with the exact energy dependent on redshift and EBL model. The models with high quasar emission and star-formation rates have cutoffs at only slightly lower energies than the fiducial model. The rapidly-falling star formation rate density in the low model at  $z > 3$  results in very little change in attenuation features for redshifts higher than this. We also find that the ionizing component of the background does not lead to large gamma-ray opacities, even in an extremely quasar-dominated case, and that there is little attenuation for gamma rays with observed energies of  $< 10$  GeV at any redshift for any of our models.

The last part of this dissertation focused on the possibility of using high-redshift GRBs as a source of gamma rays which could be used to probe the EBL. GRBs are known to emit at GeV energies, but have not yet been seen by ground-based gamma-ray telescopes. The model used here is based on the population of bursts viewed by the Swift satellite, and predicts GeV emission by using the typical flux ratios between MeV and GeV energy ranges found by experiments on the Compton Gamma-ray Observatory. Our results suggest that while the number of GeV photons seen by Fermi is likely to be small, the summed results over the lifetime of the experiment could provide constraints on the EBL. For an IACT such as MAGIC, the probability of being able to view any particular GRB is small ( $\sim 1$  %) due to the low duty cycle and available sky coverage of the instrument, though this number might be higher due to the anticorrelation of detected GRBs with the position of the sun. The fact that these telescopes must be alerted to the GRB signal by another experiment means that much or all of the prompt

phase of the burst is likely to be missed in many cases. The typical rate at which GRBs with  $z > 1$  are expected to be observed by these experiments with reasonably low energy threshold is only about 1 every 5 years, and less if only prompt phase emission is considered. The number of photons that are predicted to be seen when a burst does fall in view of the instrument can vary by a large amount due to intrinsic flux and EBL absorption, but could be as high as  $10^2$  to  $10^3$ , which could provide a lot of information about the EBL in place at the source redshift. There are many uncertainties in our emission model, including whether the flux ratios and high energy spectra assumed apply to all GRBs, and whether the Swift bursts represent an accurate sample of the GRBs that will be detected at high energy.

Modeling of dust reemission is still a major challenge for calculating the IR portion of the EBL. I have shown preliminary results in this dissertation using new spectral templates based on state-of-the-art observations with the three Spitzer instruments (Rieke et al., 2009). We hope to also calculate the EBL using the templates with the low model. Ultimately, doing a better job of computing the IR background may require moving beyond using reemission templates, which are based on an average of galaxies at a particular IR bolometric luminosity and rely on observations of the Milky Way and nearby galaxies to understand the galactic distribution of dust. This could involve incorporating dust radiative transfer codes such as SUNRISE (Jonsson, 2006) into the model. Improvements in dust modeling will largely affect emission in the mid- and far-IR. While calculating the spectral distribution of EBL flux in the far-IR peak is important for understanding the history of star-formation, this wavelength regime is

not relevant to attenuation of gamma rays. Changes in the EBL at the mid-IR PAH wavelengths could affect reconstructed spectra for the closest AGN sources.

Studies of the blazar population seen with Fermi could provide us with a lot of information about the optical and UV backgrounds, by extending observations of blazars to higher redshifts and improving statistics by increasing the numbers of such sources to hundreds or thousands. The 3-month Fermi catalogue already lists 106 sources with high confidence detections (Abdo, 2009). 42 of these are listed as BL Lac, while 57 are determined to be flat spectrum radio quasars (FSRQs). Results from EGRET suggest that FSRQs will be an increasing fraction of the AGN with increasing redshift. Whether these types of sources typically emit above 10 GeV is uncertain, but the claimed detection by MAGIC of FSRQ 3C279 at energies up to 500 GeV suggests that these sources could be a valuable probe of the UV-optical background out to high redshift.

Another manifestation of EBL effects in high energy astronomy lies in the formation of electron-positron ‘pair halos’ around AGN sources. Electron-positron pairs produced by gamma-ray interactions with the EBL will lose energy through inverse-Compton scattering background photons. This leads to an electromagnetic cascade as inverse-Compton produced photons give rise to a second generation of electron-positron pairs, and so on, until there is insufficient energy for pair-production to occur (Aharonian et al., 1994a). This process transfers energy from more energetic gamma-rays (TeV-scale) to less (GeV or MeV). Because the strength of this effect is dependent upon local background flux around the source, observations of pair-halos are one potential way to

study the infrared background, which affects gamma-rays at energies of  $> 1$  TeV, at distances much too far for these gammas to be observed directly. Even for the closest blazars, such as Mrk 421 at  $z = 0.03$ , the high opacity to gamma-rays above energies  $\sim 20$  TeV makes it impossible to test the far-IR background peak through absorption. In addition to being potentially detectable, the halo effect will alter the gamma-ray background by shifting GeV and TeV photons to lower energies, typically  $< 100$  GeV (D’Avezac et al., 2007).

The models of the high- $z$  background shown in Chapter 5 are intended to predict the background flux out to the epoch of reionization. However, we have not modeled the sources of reionization themselves, which could include primordial population-III stars, or miniquasars produced by the remnant black holes of these first stars. Ionizing photons would be quickly absorbed by the dense neutral hydrogen present at early times. Non-ionizing flux, however, would not be impeded, and could give rise to a large amount of near-UV and optical background at times during and immediately following reionization. While there are constraints on how high this flux could be, as discussed in Chapter 1, it remains an open question whether the high- $z$  background might be significantly higher than we proposed as a lingering effect of these early sources.

The results for GRBs suggest that these objects could be an source of gamma rays with which to probe the high-redshift background. While our current model is limited by our lack of knowledge about the high-energy emission from these sources, Fermi LAT has already detected multiple bursts with GeV emission. Since our understanding of these sources is rapidly advancing, it will be worthwhile to revisit this topic

in the near future, and update predictions with what we have learned from Fermi in its first year of operation. Effects such as intrinsic spectral cutoffs and internal absorption (by pair production with thermal photons originating near the GRB) have not been included in these predictions, and should be addressed in the future.

# Bibliography

Abdo, A. A. et al. 2009, preprint (ArXiv:0902.1559 [astro-ph])

Abdo, A. A., et al. 2009, *Science*, 323, 1688

Acciari, V., et al. 2009a, *ApJ*, 690, L126

Acciari, V. A., et al. 2009b, *ApJ*, 693, L104

Aharonian, F., et al. 2002, *A&A*, 384, L23

—. 2005a, *A&A*, 436, L17

—. 2005b, *A&A*, 430, 865

—. 2007a, *A&A*, 473, L25

—. 2008a, *A&A*, 477, 481

—. 2007b, *A&A*, 475, L9

—. 2009, *A&A*, 495, 505

—. 2006, *Nature*, 440, 1018

- Aharonian, F. A. 2001, in International Cosmic Ray Conference, Vol. 27, International Cosmic Ray Conference, ed. O. G. Gladysheva, G. E. Kocharov, G. A. Kovaltsov, & I. G. Usoskin, I250+
- Aharonian, F. A., et al. 1999, *A&A*, 350, 757
- Aharonian, F. A., Coppi, P. S., & Voelk, H. J. 1994a, *ApJ*, 423, L5
- . 1994b, *ApJ*, 423, L5
- Aharonian, F. A., Khangulyan, D., & Costamante, L. 2008b, *MNRAS*, 387, 1206
- Albert, J., et al. 2008a, *Science*, 320, 1752
- . 2006a, *ApJ*, 642, L119
- . 2006b, *ApJ*, 648, L105
- . 2006c, *ApJ*, 639, 761
- . 2007a, *ApJ*, 667, 358
- . 2007b, *ApJ*, 666, L17
- . 2007c, *ApJ*, 667, L21
- . 2007d, *ApJ*, 662, 892
- . 2007e, *ApJ*, 669, 862
- . 2008b, *ApJ*, 674, 1037

- Alcock, C., et al. 2000, *ApJ*, 542, 281
- Ando, S., Nakar, E., & Sari, R. 2008, preprint (ArXiv:0807.0012 [astro-ph])
- Atkins, R., et al. 2003, *ApJ*, 583, 824
- Atwood, W. B., et al. 2009, *ApJ*, 697, 1071
- Baixeras, C. 2004, preprint (astro-ph/0403180)
- Bajtlik, S., Duncan, R. C., & Ostriker, J. P. 1988, *ApJ*, 327, 570
- Band, D., et al. 1993, *ApJ*, 413, 281
- Barger, A. J., Cowie, L. L., Mushotzky, R. F., Yang, Y., Wang, W.-H., Steffen, A. T.,  
& Capak, P. 2005, *AJ*, 129, 578
- Barro, G., et al. 2009, *A&A*, 494, 63
- Bastieri, D., Bigongiari, C., Mariotti, M., Peruzzo, L., & Saggion, A. 2001, in International Cosmic Ray Conference, Vol. 7, International Cosmic Ray Conference, 2759
- Bastieri, D., Galante, N., Gaug, M., Garczarczyk, M., Longo, F., Mizobuchi, S., Peruzzo, L., & The MAGIC Collaboration. 2005, *Nuovo Cimento C Geophysics Space Physics C*, 28, 711
- Baugh, C. M., Lacey, C. G., Frenk, C. S., Granato, G. L., Silva, L., Bressan, A., Benson, A. J., & Cole, S. 2005, *MNRAS*, 356, 1191
- Becherini, Y., Djannati-Atai, A., & Punch, M. 2008, in SF2A-2008, ed. C. Charbonnel, F. Combes, & R. Samadi, 165

- Bechtold, J. 1994, *ApJS*, 91, 1
- Begelman, M. C., Fabian, A. C., & Rees, M. J. 2008, *MNRAS*, 384, L19
- Bell, E. F., McIntosh, D. H., Katz, N., & Weinberg, M. D. 2003, *ApJS*, 149, 289
- Bell, E. F., et al. 2004, *ApJ*, 608, 752
- Benson, A. J., Bower, R. G., Frenk, C. S., Lacey, C. G., Baugh, C. M., & Cole, S. 2003, *ApJ*, 599, 38
- Benson, A. J., Lacey, C. G., Baugh, C. M., Cole, S., & Frenk, C. S. 2002, *MNRAS*, 333, 156
- Bernstein, R. A. 2007, *ApJ*, 666, 663
- Bernstein, R. A., Freedman, W. L., & Madore, B. F. 2002a, *ApJ*, 571, 56
- . 2002b, *ApJ*, 571, 107
- Bertone, S., De Lucia, G., & Thomas, P. A. 2007, *MNRAS*, 379, 1143
- Birnboim, Y., & Dekel, A. 2003, *MNRAS*, 345, 349
- Blanton, M. R., Eisenstein, D., Hogg, D. W., & Zehavi, I. 2006, *ApJ*, 645, 977
- Blanton, M. R., et al. 2003, *ApJ*, 592, 819
- Blumenthal, G. R., Faber, S. M., Primack, J. R., & Rees, M. J. 1984, *Nature*, 311, 517
- Bolton, J. S., & Haehnelt, M. G. 2007, *MNRAS*, 382, 325

- Bolton, J. S., Haehnelt, M. G., Viel, M., & Springel, V. 2005, MNRAS, 357, 1178
- Bondi, H. 1952, MNRAS, 112, 195
- Borch, A., et al. 2006, A&A, 453, 869
- Bouwens, R., Broadhurst, T., & Illingworth, G. 2003, ApJ, 593, 640
- Bouwens, R. J., Illingworth, G. D., Franx, M., & Ford, H. 2007, ApJ, 670, 928
- . 2008, ApJ, 686, 230
- Bowyer, S., Korpela, E. J., Edelstein, J., Lampton, M., Morales, C., Pérez-Mercader, J., Gómez, J. F., & Trapero, J. 2001, Ap&SS, 276, 155
- Boyle, B. J., Shanks, T., Croom, S. M., Smith, R. J., Miller, L., Loaring, N., & Heymans, C. 2000, MNRAS, 317, 1014
- Brown, M. J. I., et al. 2006, ApJ, 638, 88
- Bruzual, G., & Charlot, S. 2003, MNRAS, 344, 1000
- Bruzual A., G., & Charlot, S. 1993, ApJ, 405, 538
- Buckley, J., et al. 2008, in American Institute of Physics Conference Series, Vol. 1085, American Institute of Physics Conference Series, ed. F. A. Aharonian, W. Hofmann, & F. Rieger, 902–905
- Bullock, J. S., Kolatt, T. S., Sigad, Y., Somerville, R. S., Kravtsov, A. V., Klypin, A. A., Primack, J. R., & Dekel, A. 2001, MNRAS, 321, 559

- Bunker, A. J., Stanway, E. R., Ellis, R. S., & McMahon, R. G. 2004, *MNRAS*, 355, 374
- Cambrésy, L., Reach, W. T., Beichman, C. A., & Jarrett, T. H. 2001, *ApJ*, 555, 563
- Cardelli, J. A., Clayton, G. C., & Mathis, J. S. 1989, *ApJ*, 345, 245
- Carmona, E., Majumdar, P., Moralejo, A., de Sabata, F., & Vitale, V. 2007, *Astronomische Nachrichten*, 328, 616
- Catanese, M., & Weekes, T. C. 1999, *PASP*, 111, 1193
- Cattaneo, A., Dekel, A., Devriendt, J., Guiderdoni, B., & Blaizot, J. 2006, *MNRAS*, 370, 1651
- Cattaneo, A., Dekel, A., Faber, S. M., & Guiderdoni, B. 2008, *MNRAS*, 389, 567
- Cesarsky, C., Elbaz, D., Aussel, H., Fadda, D., Franceschini, A., Flores, H., & Chagnial, P. 2002, in *Lighthouses of the Universe: The Most Luminous Celestial Objects and Their Use for Cosmology: Proceedings of the MPA/ESO/MPE/USM Joint Astronomy Conference Held in Garching, Germany, 6-10 August 2001*, ESO ASTROPHYSICS SYMPOSIA. ISBN 3-540-43769-X., Springer-Verlag, 2002, p. 119, ed. M. Gilfanov, R. Sunyeav, & E. Churazov, 119
- Charlot, S., & Fall, S. M. 2000, *ApJ*, 539, 718
- Chary, R., et al. 2004, *ApJS*, 154, 80
- Chary, R.-R. 2008, *ApJ*, 680, 32
- Chen, A., Reyes, L. C., & Ritz, S. 2004, *ApJ*, 608, 686

- Chen, Y.-M., Wild, V., Kauffmann, G., Blaizot, J., Davis, M., Noeske, K., Wang, J.-M.,  
& Willmer, C. 2009, MNRAS, 393, 406
- Chiang, J., & Dermer, C. D. 1999, ApJ, 512, 699
- Cogan, P. 2008, in American Institute of Physics Conference Series, Vol. 1085, American  
Institute of Physics Conference Series, ed. F. A. Aharonian, W. Hofmann, & F. Rieger,  
403
- Cole, S., Lacey, C. G., Baugh, C. M., & Frenk, C. S. 2000, MNRAS, 319, 168
- Cole, S., et al. 2001, MNRAS, 326, 255
- Conselice, C. J., Bundy, K., U, V., Eisenhardt, P., Lotz, J., & Newman, J. 2008,  
MNRAS, 383, 1366
- Cooke, A. J., Espey, B., & Carswell, R. F. 1997, MNRAS, 284, 552
- Cooray, A., et al. 2007, ApJ, 659, L91
- Coppin, K., et al. 2006, MNRAS, 372, 1621
- Cortina, J. 2005, Ap&SS, 297, 245
- Costamante, L., Aharonian, F., Horns, D., & Ghisellini, G. 2004, New Astronomy  
Review, 48, 469
- Cox, T. J., Jonsson, P., Somerville, R. S., Primack, J. R., & Dekel, A. 2008, MNRAS,  
384, 386

- Cristiani, S., D'Odorico, S., Fontana, A., Giallongo, E., & Savaglio, S. 1995, *MNRAS*, 273, 1016
- Croom, S. M., Smith, R. J., Boyle, B. J., Shanks, T., Miller, L., Outram, P. J., & Loaring, N. S. 2004, *MNRAS*, 349, 1397
- Croton, D. J., et al. 2006, *MNRAS*, 365, 11
- Cusumano, G., et al. 2006, *Nature*, 440, 164
- da Cunha, E., Charlot, S., & Elbaz, D. 2008, *MNRAS*, 388, 1595
- Dahlen, T., Mobasher, B., Dickinson, M., Ferguson, H. C., Giavalisco, M., Kretchmer, C., & Ravindranath, S. 2007, *ApJ*, 654, 172
- Dahlen, T., Mobasher, B., Somerville, R. S., Moustakas, L. A., Dickinson, M., Ferguson, H. C., & Giavalisco, M. 2005, *ApJ*, 631, 126
- Dai, X. 2009, *ApJ*, 697, L68
- Dale, D. A., et al. 2007, *ApJ*, 655, 863
- Dall'Aglio, A., Wisotzki, L., & Worseck, G. 2008, *A&A*, 491, 465
- Daniel, M. K., et al. 2005, *ApJ*, 621, 181
- Davé, R. 2008, *MNRAS*, 385, 147
- D'Avezac, P., Dubus, G., & Giebels, B. 2007, *A&A*, 469, 857
- de Jager, O. C., Stecker, F. W., & Salamon, M. H. 1994, *Nature*, 369, 294

- De Lucia, G., & Blaizot, J. 2007, MNRAS, 375, 2
- Dekel, A., et al. 2009, Nature, 457, 451
- Dekel, A., & Silk, J. 1986, ApJ, 303, 39
- Dermer, C. D. 2007, ApJ, 659, 958
- Devlin, M. J., et al. 2009, Nature, 458, 737
- Devriendt, J. E. G., & Guiderdoni, B. 2000, A&A, 363, 851
- Devriendt, J. E. G., Guiderdoni, B., & Sadat, R. 1999, A&A, 350, 381
- Dijkstra, M., Haiman, Z., & Loeb, A. 2004, ApJ, 613, 646
- Dingus, B. L. 1995, Ap&SS, 231, 187
- Dolch, T. 2009, in prep
- Dole, H., et al. 2006, A&A, 451, 417
- . 2004, ApJS, 154, 87
- Dwek, E., Arendt, R. G., & Krennrich, F. 2005, ApJ, 635, 784
- Dwek, E., & Krennrich, F. 2005, ApJ, 618, 657
- Dwek, E., & Slavin, J. 1994, ApJ, 436, 696
- Dye, S., et al. 2006, ApJ, 644, 769

- Elbaz, D., Cesarsky, C. J., Chaniel, P., Aussel, H., Franceschini, A., Fadda, D., & Chary, R. R. 2002, *A&A*, 384, 848
- Elbaz, D., Le Floch, E., Dole, H., & Marcillac, D. 2005, *A&A*, 434, L1
- Faber, S. M., et al. 2007, *ApJ*, 665, 265
- Fan, X., et al. 2001, *AJ*, 122, 2833
- . 2006, *AJ*, 132, 117
- Fan, Y. Z., Dai, Z. G., & Wei, D. M. 2004, *A&A*, 415, 483
- Fan, Y.-Z., Piran, T., Narayan, R., & Wei, D.-M. 2008, *MNRAS*, 384, 1483
- Fardal, M. A., Katz, N., Weinberg, D. H., & Davé, R. 2007, *MNRAS*, 379, 985
- Faucher-Giguère, C.-A., Lidz, A., Hernquist, L., & Zaldarriaga, M. 2008a, *ApJ*, 682, L9
- Faucher-Giguère, C.-A., Prochaska, J. X., Lidz, A., Hernquist, L., & Zaldarriaga, M. 2008b, *ApJ*, 681, 831
- Fazio, G. G., et al. 2004, *ApJS*, 154, 39
- Fazio, G. G., & Stecker, F. W. 1970, *Nature*, 226, 135
- Fechner, C., et al. 2006, *A&A*, 455, 91
- Finkbeiner, D. P., Davis, M., & Schlegel, D. J. 2000, *ApJ*, 544, 81
- Fixsen, D. J., Dwek, E., Mather, J. C., Bennett, C. L., & Shafer, R. A. 1998, *ApJ*, 508,

- Fontana, A., et al. 2006, *A&A*, 459, 745
- Fontanot, F., De Lucia, G., Monaco, P., Somerville, R. S., & Santini, P. 2009, preprint (ArXiv:0901.1130 [astro-ph])
- Fortin, P. 2008, preprint (ArXiv:0810.0301 [astro-ph])
- Fossati, G., Maraschi, L., Celotti, A., Comastri, A., & Ghisellini, G. 1998, *MNRAS*, 299, 433
- Franceschini, A. 2001, in *IAU Symposium, Vol. 204, The Extragalactic Infrared Background and its Cosmological Implications*, ed. M. Harwit & M. G. Hauser, 283
- Franceschini, A., Aussel, H., Cesarsky, C. J., Elbaz, D., & Fadda, D. 2001, *A&A*, 378, 1
- Franceschini, A., Mazzei, P., de Zotti, G., & Danese, L. 1994, *ApJ*, 427, 140
- Franceschini, A., Rodighiero, G., & Vaccari, M. 2008, *A&A*, 487, 837
- Frayer, D. T., et al. 2006, *ApJ*, 647, L9
- Fujita, A., Martin, C. L., Mac Low, M.-M., & Abel, T. 2003, *ApJ*, 599, 50
- Gabasch, A., et al. 2006, *A&A*, 448, 101
- . 2004, *ApJ*, 616, L83
- Gallazzi, A., Charlot, S., Brinchmann, J., White, S. D. M., & Tremonti, C. A. 2005, *MNRAS*, 362, 41

- Garczarczyk, M., et al. 2008, in American Institute of Physics Conference Series, Vol. 1065, American Institute of Physics Conference Series, ed. Y.-F. Huang, Z.-G. Dai, & B. Zhang, 342–344
- Gardner, J. P., Brown, T. M., & Ferguson, H. C. 2000, *ApJ*, 542, L79
- Gardner, J. P., Sharples, R. M., Carrasco, B. E., & Frenk, C. S. 1996, *MNRAS*, 282, L1
- Ghisellini, G., Celotti, A., & Costamante, L. 2002, *A&A*, 386, 833
- Ghisellini, G., Celotti, A., Fossati, G., Maraschi, L., & Comastri, A. 1998, *MNRAS*, 301, 451
- Ghisellini, G., & Tavecchio, F. 2008, *MNRAS*, 387, 1669
- Giallongo, E., Fontana, A., & Madau, P. 1997, *MNRAS*, 289, 629
- Gilmore, R. C., Madau, P., Primack, J. R., Somerville, R. S., & Haardt, F. 2009a, submitted to *MNRAS*
- Gilmore, R. C., Primack, J. R., & Somerville, R. S. 2009b, in prep
- Gnedin, N. Y. 2008, *ApJ*, 673, L1
- Gnedin, N. Y., Kravtsov, A. V., & Chen, H.-W. 2008, *ApJ*, 672, 765
- Gorjian, V., Wright, E. L., & Chary, R. R. 2000, *ApJ*, 536, 550
- Gould, R. J., & Schreder, G. P. 1967, *Phys. Rev.*, 155, 1404
- Greiner, J., et al. 2009a, preprint (ArXiv:0902.0761 [astro-ph])

- . 2009b, *ApJ*, 693, 1610
- Guiderdoni, B., & Devriendt, J. E. G. 1999, preprint (astro-ph/9911162)
- Haardt, F., & Madau, P. 1996, *ApJ*, 461, 20
- Haardt, F., & Madau, P. 2001, in *Clusters of Galaxies and the High Redshift Universe Observed in X-rays*, ed. D. M. Neumann & J. T. V. Tran
- Haehnelt, M. G., Madau, P., Kudritzki, R., & Haardt, F. 2001, *ApJ*, 549, L151
- Hartman, R. C., et al. 1999, *ApJS*, 123, 79
- Hauser, M. G., et al. 1998, *ApJ*, 508, 25
- Hauser, M. G., & Dwek, E. 2001, *ARA&A*, 39, 249
- Heitler, W. 1960, *The Quantum Theory of Radiation*, Dover Publications
- Hinton, J. A. 2004, *New Astronomy Review*, 48, 331
- Hogan, C. J., & Dalcanton, J. J. 2000, *Phys. Rev. D*, 62, 063511
- Hopkins, A. M. 2004, *ApJ*, 615, 209
- Hopkins, A. M. 2007, in *Astronomical Society of the Pacific Conference Series*, Vol. 380, *Deepest Astronomical Surveys*, ed. J. Afonso, H. C. Ferguson, B. Mobasher, & R. Norris, 423
- Hopkins, A. M., & Beacom, J. F. 2006, *ApJ*, 651, 142
- Hopkins, P. F., Richards, G. T., & Hernquist, L. 2007, *ApJ*, 654, 731

- Horan, D. 2008, in International Cosmic Ray Conference, Vol. 3, International Cosmic Ray Conference, 1107–1110
- Horns, D. 2006, in Society of Photo-Optical Instrumentation Engineers (SPIE) Conference Series, Vol. 6267, Society of Photo-Optical Instrumentation Engineers (SPIE) Conference Series
- Hu, E. M., Kim, T.-S., Cowie, L. L., Songaila, A., & Rauch, M. 1995, *AJ*, 110, 1526
- Iglesias-Páramo, J., Buat, V., Donas, J., Boselli, A., & Milliard, B. 2004, *A&A*, 419, 109
- Jelley, J. V. 1966, *Phys. Rev. Lett.*, 16, 479
- Jiang, L., et al. 2006, *AJ*, 131, 2788
- Jones, D. H., Peterson, B. A., Colless, M., & Saunders, W. 2006, *MNRAS*, 369, 25
- Jonsson, P. 2006, *MNRAS*, 372, 2
- Jonsson, P., Cox, T. J., Primack, J. R., & Somerville, R. S. 2006, *ApJ*, 637, 255
- Kannappan, S. J. 2004, *ApJ*, 611, L89
- Karimabadi, H., & Blitz, L. 1984, *ApJ*, 283, 169
- Kashlinsky, A., Arendt, R. G., Mather, J., & Moseley, S. H. 2005, *Nature*, 438, 45
- Kashlinsky, A., Mather, J. C., & Odenwald, S. 1996a, *ApJ*, 473, L9
- Kashlinsky, A., Mather, J. C., Odenwald, S., & Hauser, M. G. 1996b, *ApJ*, 470, 681

- Kashlinsky, A., & Odenwald, S. 2000, *ApJ*, 528, 74
- Katarzyński, K., Ghisellini, G., Tavecchio, F., Gracia, J., & Maraschi, L. 2006, *MNRAS*, 368, L52
- Kauffmann, G., et al. 2003, *MNRAS*, 341, 33
- Kawada, M., et al. 1994, *ApJ*, 425, L89
- Kelsall, T., et al. 1998, *ApJ*, 508, 44
- Kennea, J. A. 2008, *GRB Coordinates Network*, 8253, 1
- Kennicutt, Jr., R. C. 1989, *ApJ*, 344, 685
- Kennicutt, Jr., R. C., et al. 1998, *ApJ*, 498, 181
- Keres, D., Katz, N., Fardal, M., Dave, R., & Weinberg, D. H. 2008, preprint (ArXiv:0809.1430 [astro-ph])
- Kim, T.-S., Hu, E. M., Cowie, L. L., & Songaila, A. 1997, *AJ*, 114, 1
- Kirkman, D., & Tytler, D. 2008, *MNRAS*, 391, 1457
- Kirkman, D., et al. 2005, *MNRAS*, 360, 1373
- Kneiske, T. M., Bretz, T., Mannheim, K., & Hartmann, D. H. 2004, *A&A*, 413, 807
- Kneiske, T. M., & Mannheim, K. 2008, *A&A*, 479, 41
- Kneiske, T. M., Mannheim, K., & Hartmann, D. H. 2002, *A&A*, 386, 1

- Kochanek, C. S., et al. 2001, *ApJ*, 560, 566
- Komatsu, E., et al. 2009, *ApJS*, 180, 330
- Konopelko, A., Cui, W., Duke, C., & Finley, J. P. 2008, *ApJ*, 679, L13
- Konopelko, A., Mastichiadis, A., Kirk, J., de Jager, O. C., & Stecker, F. W. 2003, *ApJ*, 597, 851
- Kriss, G. A., et al. 2001, *Science*, 293, 1112
- Lagache, G., Haffner, L. M., Reynolds, R. J., & Tufte, S. L. 2000, *A&A*, 354, 247
- Lagache, G., Puget, J.-L., & Dole, H. 2005, *ARA&A*, 43, 727
- Le, T., & Dermer, C. D. 2008, preprint (ArXiv:0807.0355 [astro-ph])
- Levenson, L. R., & Wright, E. L. 2008, *ApJ*, 683, 585
- Levenson, L. R., Wright, E. L., & Johnson, B. D. 2007, *ApJ*, 666, 34
- Liang, E., Zhang, B., Virgili, F., & Dai, Z. G. 2007, *ApJ*, 662, 1111
- Liske, J., & Williger, G. M. 2001, *MNRAS*, 328, 653
- Liu, H. T., Bai, J. M., & Ma, L. 2008, preprint (ArXiv:0807.3133 [astro-ph])
- Loeb, A., & Eisenstein, D. J. 1995, *ApJ*, 448, 17
- Lu, L., Wolfe, A. M., & Turnshek, D. A. 1991, *ApJ*, 367, 19
- MacMinn, D., & Primack, J. R. 1996, *Space Science Reviews*, 75, 413

- Madau, P., & Haardt, F. 2009, *ApJ*, 693, L100
- Madau, P., Haardt, F., & Rees, M. J. 1999, *ApJ*, 514, 648
- Madau, P., & Phinney, E. S. 1996, *ApJ*, 456, 124
- Madau, P., & Pozzetti, L. 2000, *MNRAS*, 312, L9
- Madau, P., Pozzetti, L., & Dickinson, M. 1998, *ApJ*, 498, 106
- Madau, P., Rees, M. J., Volonteri, M., Haardt, F., & Oh, S. P. 2004, *ApJ*, 604, 484
- Madau, P., & Silk, J. 2005, *MNRAS*, 359, L37
- Maier, G. 2007, preprint (ArXiv:0709.3654 [astro-ph])
- Malkan, M. A., & Stecker, F. W. 1998, *ApJ*, 496, 13
- . 2001, *ApJ*, 555, 641
- Mannucci, F., Buttery, H., Maiolino, R., Marconi, A., & Pozzetti, L. 2007, *A&A*, 461, 423
- Maraschi, L., Ghisellini, G., Tavecchio, F., Foschini, L., & Sambruna, R. M. 2008, *International Journal of Modern Physics D*, 17, 1457
- Marchesini, D., et al. 2007, *ApJ*, 656, 42
- Martinez, M. 2008, in *American Institute of Physics Conference Series*, Vol. 1085, American Institute of Physics Conference Series, ed. F. A. Aharonian, W. Hofmann, & F. Rieger, 824–829

- Martini, P. 2001, *AJ*, 121, 598
- Matsuhara, H., et al. 2000, *A&A*, 361, 407
- Matsumoto, T., Hayakawa, S., Matsuo, H., Murakami, H., Sato, S., Lange, A. E., & Richards, P. L. 1988, *ApJ*, 329, 567
- Matsumoto, T., et al. 2005, *ApJ*, 626, 31
- Matute, I., La Franca, F., Pozzi, F., Gruppioni, C., Lari, C., & Zamorani, G. 2006, *A&A*, 451, 443
- Mazin, D., & Goebel, F. 2007, *ApJ*, 655, L13
- Mazin, D., & Raue, M. 2007, *A&A*, 471, 439
- Meszáros, P. 2006, *Reports on Progress in Physics*, 69, 2259
- Milliard, B., Donas, J., Laget, M., Armand, C., & Vuillemin, A. 1992, *A&A*, 257, 24
- Miniati, F., Ferrara, A., White, S. D. M., & Bianchi, S. 2004, *MNRAS*, 348, 964
- Montero-Dorta, A. D., & Prada, F. 2008, preprint (ArXiv:0806.4930 [astro-ph])
- Mukherjee, R., et al. 1997, *ApJ*, 490, 116
- Navarro, J. F., Frenk, C. S., & White, S. D. M. 1997, *ApJ*, 490, 493
- Nikishov, A. I. 1962, *Soviet Physics JETP*, 14, 393
- Norberg, P., et al. 2002, *MNRAS*, 332, 827

- Oh, S. P. 2001, *ApJ*, 553, 25
- Osterbrock, D. E. 1989, *Astrophysics of gaseous nebulae and active galactic nuclei* Mill Valley, CA, University Science Books, 1989, 422 p.
- Ouchi, M., et al. 2004, *ApJ*, 611, 660
- Paciesas, W. S., et al. 1999, *ApJS*, 122, 465
- Panaitescu, A. 2008, *MNRAS*, 385, 1628
- Papovich, C., et al. 2004, *ApJS*, 154, 70
- Partridge, R. B., & Peebles, P. J. E. 1967, *ApJ*, 148, 377
- Pavlidou, V., Siegal-Gaskins, J. M., Fields, B. D., Olinto, A. V., & Brown, C. 2008, *ApJ*, 677, 27
- Peebles, P. J. E. 1993, *Principles of physical cosmology*, Princeton Series in Physics, Princeton, NJ: Princeton University Press
- Pei, Y. C., Fall, S. M., & Hauser, M. G. 1999, *ApJ*, 522, 604
- Pérez-González, P. G., et al. 2005, *ApJ*, 630, 82
- Piran, T. 1999, *Phys. Rep.*, 314, 575
- Preece, R. D., Briggs, M. S., Mallozzi, R. S., Pendleton, G. N., Paciasas, W. S., & Band, D. L. 2000, *ApJS*, 126, 19
- Press, W. H., & Schechter, P. 1974, *ApJ*, 187, 425

- Primack, J. R., Bullock, J. S., & Somerville, R. S. 2005, in American Institute of Physics Conference Series, Vol. 745, High Energy Gamma-Ray Astronomy, ed. F. A. Aharonian, H. J. Völk, & D. Horns, 23–33
- Primack, J. R., Bullock, J. S., Somerville, R. S., & MacMinn, D. 1999, *Astroparticle Physics*, 11, 93
- Primack, J. R., Gilmore, R. C., & Somerville, R. S. 2008, in American Institute of Physics Conference Series, Vol. 1085, American Institute of Physics Conference Series, ed. F. A. Aharonian, W. Hofmann, & F. Rieger, 71–82
- Primack, J. R., Somerville, R. S., Bullock, J. S., & Devriendt, J. E. G. 2001, in American Institute of Physics Conference Series, Vol. 558, American Institute of Physics Conference Series, ed. F. A. Aharonian & H. J. Völk, 463
- Puget, J.-L., Abergel, A., Bernard, J.-P., Boulanger, F., Burton, W. B., Desert, F.-X., & Hartmann, D. 1996, *A&A*, 308, L5
- Puget, J. L., & Lagache, G. 2001, in IAU Symposium, Vol. 204, The Extragalactic Infrared Background and its Cosmological Implications, ed. M. Harwit, 233
- Punch, M., et al. 1992, *Nature*, 358, 477
- Quinn, J., et al. 1996a, *ApJ*, 456, L83
- Quinn, T., Katz, N., & Efstathiou, G. 1996b, *MNRAS*, 278, L49
- Rauch, M., et al. 1997, *ApJ*, 489, 7

- Razoumov, A. O., & Sommer-Larsen, J. 2006, *ApJ*, 651, L89
- . 2007, *ApJ*, 668, 674
- Razzaque, S., Dermer, C. D., & Finke, J. D. 2008, preprint (ArXiv:0807.4294 [astro-ph])
- Reddy, N. A., Steidel, C. C., Fadda, D., Yan, L., Pettini, M., Shapley, A. E., Erb, D. K., & Adelberger, K. L. 2006, *ApJ*, 644, 792
- Reddy, N. A., Steidel, C. C., Pettini, M., Adelberger, K. L., Shapley, A. E., Erb, D. K., & Dickinson, M. 2008, *ApJS*, 175, 48
- Richards, G. T., et al. 2006, *AJ*, 131, 2766
- Richards, G. T., Vanden Berk, D. E., Reichard, T. A., Hall, P. B., Schneider, D. P., SubbaRao, M., Thakar, A. R., & York, D. G. 2002, *AJ*, 124, 1
- Rieke, G. H., Alonso-Herrero, A., Weiner, B. J., Pérez-González, P. G., Blaylock, M., Donley, J. L., & Marcillac, D. 2009, *ApJ*, 692, 556
- Rowan-Robinson, M. 2001, *ApJ*, 549, 745
- Rowan-Robinson, M., Hughes, J., Veda, K., & Walker, D. W. 1990, *MNRAS*, 246, 273
- Sakamoto, T., et al. 2008, *ApJS*, 175, 179
- Salamon, M. H., & Stecker, F. W. 1998, *ApJ*, 493, 547
- Salpeter, E. E. 1955, *ApJ*, 121, 161
- Salvaterra, R., & Ferrara, A. 2003, *MNRAS*, 339, 973

- . 2006, MNRAS, 367, L11
- Salvaterra, R., Haardt, F., & Ferrara, A. 2005, MNRAS, 362, L50
- Sanders, D. B., Phinney, E. S., Neugebauer, G., Soifer, B. T., & Matthews, K. 1989,  
ApJ, 347, 29
- Sanders, D. B., et al. 2007, ApJS, 172, 86
- Sari, R., & Esin, A. A. 2001, ApJ, 548, 787
- Saz Parkinson, P. M., & Dingus, B. L. 2008, in International Cosmic Ray Conference,  
Vol. 3, International Cosmic Ray Conference, 1187–1190
- Schaye, J., Aguirre, A., Kim, T.-S., Theuns, T., Rauch, M., & Sargent, W. L. W. 2003,  
ApJ, 596, 768
- Schiminovich, D., et al. 2005, ApJ, 619, L47
- Schirber, M., & Bullock, J. S. 2003, ApJ, 584, 110
- Schirber, M., Miralda-Escudé, J., & McDonald, P. 2004, ApJ, 610, 105
- Sciama, D. W. 1998, A&A, 335, 12
- Scott, J., Bechtold, J., Dobrzycki, A., & Kulkarni, V. P. 2000, ApJS, 130, 67
- Shapley, A. E., Erb, D. K., Pettini, M., Steidel, C. C., & Adelberger, K. L. 2004, ApJ,  
612, 108

- Shapley, A. E., Steidel, C. C., Pettini, M., Adelberger, K. L., & Erb, D. K. 2006, *ApJ*, 651, 688
- Sheth, R. K., & Tormen, G. 1999, *MNRAS*, 308, 119
- Shull, J. M., Tumlinson, J., Giroux, M. L., Kriss, G. A., & Reimers, D. 2004, *ApJ*, 600, 570
- Shupe, D. L., et al. 2008, *AJ*, 135, 1050
- Siana, B., et al. 2007, *ApJ*, 668, 62
- Sijacki, D., Springel, V., di Matteo, T., & Hernquist, L. 2007, *MNRAS*, 380, 877
- Sikora, M., & Madejski, G. 2001, in *American Institute of Physics Conference Series*, Vol. 558, *American Institute of Physics Conference Series*, ed. F. A. Aharonian & H. J. Völk, 275
- Simard, L., et al. 2002, *ApJS*, 142, 1
- Smette, A., Heap, S. R., Williger, G. M., Tripp, T. M., Jenkins, E. B., & Songaila, A. 2002, *ApJ*, 564, 542
- Smith, J. D. T., et al. 2007, *ApJ*, 656, 770
- Soifer, B. T., & Neugebauer, G. 1991, *AJ*, 101, 354
- Somerville, R. S. 1997, PhD thesis, University of California, Santa Cruz
- Somerville, R. S., Bullock, J. S., & Livio, M. 2003, *ApJ*, 593, 616

- Somerville, R. S., Hopkins, P. F., Cox, T. J., Robertson, B. E., & Hernquist, L. 2008, MNRAS, 391, 481
- Somerville, R. S., & Kolatt, T. S. 1999, MNRAS, 305, 1
- Somerville, R. S., & Primack, J. R. 1999, MNRAS, 310, 1087
- Somerville, R. S., Primack, J. R., & Faber, S. M. 2000, preprint (astro-ph/0006364)
- . 2001, MNRAS, 320, 504
- Srbnovsky, J., & Wyithe, S. 2008, preprint (ArXiv:0807.4782 [astro-ph])
- Srbnovsky, J. A., & Wyithe, J. S. B. 2007, MNRAS, 374, 627
- Stecker, F. W., & de Jager, O. C. 1997, ApJ, 476, 712
- Stecker, F. W., Malkan, M. A., & Scully, S. T. 2006, ApJ, 648, 774
- . 2007, ApJ, 658, 1392
- Stecker, F. W., & Scully, S. T. 2009, ApJ, 691, L91
- Steidel, C. C., Adelberger, K. L., Giavalisco, M., Dickinson, M., & Pettini, M. 1999, ApJ, 519, 1
- Steidel, C. C., Pettini, M., & Adelberger, K. L. 2001, ApJ, 546, 665
- Stengler-Larrea, E. A., et al. 1995, ApJ, 444, 64
- Swanenburg, B. N., et al. 1978, Nature, 275, 298

- Symeonidis, M., Willner, S. P., Rigopoulou, D., Huang, J.-S., Fazio, G. G., & Jarvis, M. J. 2008, *MNRAS*, 385, 1015
- Tagliaferri, G., et al. 2008, *ApJ*, 679, 1029
- Tajima, H., Bregeon, J., Chiang, J., & Thayer, G. 2008, *GRB Coordinates Network*, 8246, 1
- Takeuchi, T. T., Ishii, T. T., Hirashita, H., Yoshikawa, K., Matsuhara, H., Kawara, K., & Okuda, H. 2001, *PASJ*, 53, 37
- Tavani, M., et al. 2008, *Nuclear Instruments and Methods in Physics Research A*, 588, 52
- Tavecchio, F., & Mazin, D. 2009, *MNRAS*, 392, L40
- Telfer, R. C., Zheng, W., Kriss, G. A., & Davidsen, A. F. 2002, *ApJ*, 565, 773
- Teshima, M., Prandini, E., Bock, R., & et al. 2008, in *International Cosmic Ray Conference*, Vol. 3, *International Cosmic Ray Conference*, 1045–1048
- Thompson, R. I., Eisenstein, D., Fan, X., Dickinson, M., Illingworth, G., & Kennicutt, Jr., R. C. 2006, *ApJ*, 647, 787
- Thompson, R. I., Eisenstein, D., Fan, X., Rieke, M., & Kennicutt, R. 2008, preprint (ArXiv:0801.3825 [astro-ph])
- Tisserand, P., et al. 2007, *A&A*, 469, 387
- Totani, T., Yoshii, Y., Iwamuro, F., Maihara, T., & Motohara, K. 2001, *ApJ*, 550, L137

- Treves, A., Falomo, R., & Uslenghi, M. 2007, *A&A*, 473, L17
- Tytler, D., O'Meara, J. M., Suzuki, N., Kirkman, D., Lubin, D., & Orin, A. 2004, *AJ*, 128, 1058
- van Dalen, A., & Schaefer, R. K. 1992, *ApJ*, 398, 33
- van Dokkum, P., Cooray, A., Labbé, I., Papovich, C., & Stern, D. 2007, in *American Institute of Physics Conference Series*, Vol. 943, *The Science Opportunities of the Warm Spitzer Mission Workshop*, ed. L. J. Storrie-Lombardi & N. A. Silbermann, 122–136
- Vanden Berk, D. E., et al. 2001, *AJ*, 122, 549
- Verma, A., Lehnert, M. D., Förster Schreiber, N. M., Bremer, M. N., & Douglas, L. 2007, *MNRAS*, 377, 1024
- Virgili, F. J., Liang, E.-W., & Zhang, B. 2009, *MNRAS*, 392, 91
- von der Linden, A., Best, P. N., Kauffmann, G., & White, S. D. M. 2007, *MNRAS*, 379, 867
- Wagner, R., Dorner, D., Hayashida, M., & et al. 2008, in *International Cosmic Ray Conference*, Vol. 3, *International Cosmic Ray Conference*, 889–892
- Wagner, R. M. 2008, *MNRAS*, 385, 119
- Weekes, T. C., & Turver, K. E. 1977, *Proc. 12th ESLAB Symp.*, 124, 279
- White, S. D. M., & Frenk, C. S. 1991, *ApJ*, 379, 52

- Wilkins, S. M., Trentham, N., & Hopkins, A. M. 2008, *MNRAS*, 385, 687
- Williams, D. A., et al. 2009, preprint (ArXiv:0902.3466 [astro-ph])
- Williams, D. A., & MILAGRO Collaboration. 2005, in American Institute of Physics Conference Series, Vol. 745, High Energy Gamma-Ray Astronomy, ed. F. A. Aharonian, H. J. Völk, & D. Horns, 499–504
- Williger, G. M., Baldwin, J. A., Carswell, R. F., Cooke, A. J., Hazard, C., Irwin, M. J., McMahon, R. G., & Storrie-Lombardi, L. J. 1994, *ApJ*, 428, 574
- Wolf, C., Meisenheimer, K., Rix, H.-W., Borch, A., Dye, S., & Kleinheinrich, M. 2003, *A&A*, 401, 73
- Wright, E. L. 1998, *ApJ*, 496, 1
- . 2001, *ApJ*, 553, 538
- . 2004, *New Astronomy Review*, 48, 465
- Wright, E. L., & Reese, E. D. 2000, *ApJ*, 545, 43
- Wyder, T. K., et al. 2005, *ApJ*, 619, L15
- Xu, C. K., et al. 2005, *ApJ*, 619, L11
- York, D. G., et al. 2000, *AJ*, 120, 1579
- Yoshida, N., Stoehr, F., Springel, V., & White, S. D. M. 2002, *MNRAS*, 335, 762
- Yoshii, Y., & Takahara, F. 1988, *ApJ*, 326, 1

Yüksel, H., Kistler, M. D., Beacom, J. F., & Hopkins, A. M. 2008, ApJ, 683, L5

Zhang, B., & Mészáros, P. 2001, ApJ, 559, 110

Zheng, W., et al. 2004, ApJ, 605, 631

Zou, Y.-C., Fan, Y.-Z., & Piran, T. 2008, preprint (ArXiv:0811.2997 [astro-ph])